Distribution Agreement

In presenting this thesis or dissertation as a partial fulfillment of the requirements for an advanced degree from Emory University, I hereby grant to Emory University and its agents the non-exclusive license to archive, make accessible, and display my thesis or dissertation in whole or in part in all forms of media, now or hereafter known, including display on the world wide web. I understand that I may select some access restrictions as part of the online submission of this thesis or dissertation. I retain all ownership rights to the copyright of the thesis or dissertation. I also retain the right to use in future works (such as articles or books) all or part of this thesis or dissertation.

Signature:

_____ _____

Henry J. Zecca Date

Design and Synthesis of a PD-L1 Radioligand for Diagnostic Imaging

and

Development and Optimization of a Potent Liver Receptor Homolog-1 Agonist

By

Henry J. Zecca

Doctor of Philosophy

Chemistry

Nathan Jui, Ph.D.
Advisor

Jennifer Heemstra, Ph.D.
Committee Member

Dennis Liotta, Ph.D.
Committee Member

Accepted:

Kimberly J. Arriola, Ph.D.
Dean of the James T. Laney School of
Graduate Studies

Date

Design and Synthesis of a PD-L1 Radioligand for Diagnostic Imaging
and
Development and Optimization of a Potent Liver Receptor Homolog-1 Agonist

By

Henry J. Zecca

B.A., Colorado College 2016

Advisor: Nathan T. Jui, Ph.D.

An abstract of
A dissertation submitted to the Faculty of the
James T. Laney School of Graduate Studies of Emory University
in partial fulfillment of the requirements for the degree of
Doctor of Philosophy
in Chemistry
2021

Abstract

Design and Synthesis of a PD-L1 Radioligand for Diagnostic Imaging
and
Development and Optimization of a Potent Liver Receptor Homolog-1 Agonist

By: Henry J. Zecca

Immune checkpoint inhibitors have revolutionized the way cancer is treated; instead of broadly cytotoxic therapies that "kill the patient, but kill the cancer faster", these therapeutics enable the immune system's ability to detect and clear tumors. The first therapies to be approved based on the genetic makeup of a tumor instead of the anatomical location and approved for over 15 indications, antibody drugs targeting programmed cell death protein 1 (PD-1) and its ligand (PD-L1) are the premier example of immune checkpoint inhibitors. However, these drugs will only work if the tumor is expressing the PD-L1 protein. Unfortunately, the current assays used to determine PD-L1 expression levels are poorly effective; biopsy samples fail to generate a complete picture of heterogeneous tumors, PD-L1 expression is tightly regulated by hormones that are only present *in vivo*, and the assays themselves are subjectively scored with variable definitions of PD-L1 positivity. This uncertainty related to a patient's potential response hampers the effective deployment of this revolutionary class of drugs.

Positron emission tomography (PET) has been used for decades as a powerful diagnostic technique for diagnosing and tracking tumors in patients. This technology, aided by a radiotracer such as ^{18}F-fluorodeoxyglucose, allows oncologists to visualize the tumors in their patients and with modern mutation- or protein-specific tracers, allows clinicians to formulate treatment plans.

Herein we describe the design, synthesis, and optimization of a PET tracer to visualize PD-L1 mutational status. Based on a PD-L1 binding small molecule, this radiotracer is easy to synthesize and selectively binds to PD-L1 with nanomolar potency.

Design and Synthesis of a PD-L1 Radioligand for Diagnostic Imaging

and

Development and Optimization of a Potent Liver Receptor Homolog-1 Agonist

By

Henry J. Zecca

B.A., Colorado College, 2016

Advisor: Nathan T. Jui, Ph.D.

A dissertation submitted to the Faculty of the
James T. Laney School of Graduate Studies of Emory University
in partial fulfillment of the requirements for the degree of
Doctor of Philosophy
in Chemistry
2021

Acknowledgements

Kristen: Thank you so much for being there for me throughout this entire experience, I certainly would not have finished without your support. From the good times to the bad I knew I always had someone I could come home to and talk about my day and would encourage me to just make it one more week when things were at their worst. I can't wait to spend our lives together.

Nate: I still remember the day you called to tell me that I had been accepted to Emory for grad school and was (and still am) impressed and happy that you were willing to talk through the LRH-1 project with some kid—even though you certainly had a full afternoon of acceptance calls to make after mine. From the very beginning through to the end you have been there to get excited about ideas with and encourage me (possibly too much) to explore them and try everything. I will forever cherish my time here, both the fun memories as well as the challenges; nothing worth doing ever came without working for it.

Jen: I want to thank you for being on my committee and for your infectious enthusiasm, I would leave our meetings even more excited about my own projects as a result of your feedback.

Dr. Liotta: I can't thank you enough for your invaluable feedback and wisdom during annual meetings. I am ceaselessly amazed by how quickly you can come up with insightful suggestions after just a few minutes of me describing a problem. I also want to thank you for your support of the EBCC and nontraditional career paths after grad school. For someone who pretty quickly realized that a lifetime at the bench was not what I wanted, knowing that I had a mentor who would support that decision gave me strength to persevere when I needed it the most.

Dave: "I couldn't have done it without you" gets thrown around a lot in these sorts of things but having someone who I could talk about chemistry *and* hobbies and not just chemistry kept

me sane. I'm happy to be able to call you a friend and I'm excited to see what kind of projects we talk each other into.

Kelly: It was invaluable to have someone to talk with who started this journey at the same time. We've been able to watch the group change over time, and it was great to know that there was always someone who would understand.

Professor Wuest: I cannot thank you enough for starting the EBCC here at Emory, it was an incredible experience, and I am excited to watch it continue to grow after participating in the first cohort. In my time with the group, I met so many wonderful people I hope to work with again, gained knowledge and skills from disciplines that I would otherwise have limited exposure to, and now know entirely too much about poultry production in America.

Dean Tedesco: I know you will never see this, but I have always been encouraged knowing that the person running Laney Graduate School was a vocal supporter of our graduates going on to do things that aren't academia. The "pathways beyond the professoriate" lunches were inspiring and reaffirmed that continuing on to get my PhD was the right decision.

Table of Contents

List of Figures

List of Schemes

List of Tables

Chapter 1 Thesis Introduction

1.1 Translational Chemistry

From its inception, the Jui Group has strived to discover and develop new chemical methods to generate molecules with biological relevance. The earliest work focused on synthesizing unnatural aryl amino acids through radical conjugate addition[1]. Further understanding of the nature of aryl radicals enabled hydroarylation of a diversity of olefinic substrates under extremely mild conditions[2]. This hydroarylation chemistry provides ready access to substrate classes such as phenethylamines, which have well established bioactivity. Simultaneously, the group was working on selective functionalization of one of the most traditionally inert moieties, the trifluoromethyl group (Figure 1.1).[3] This process occurs through addition of an electron to the electron poor arene followed by loss of fluoride through thermodynamically driven mesolytic cleavage.

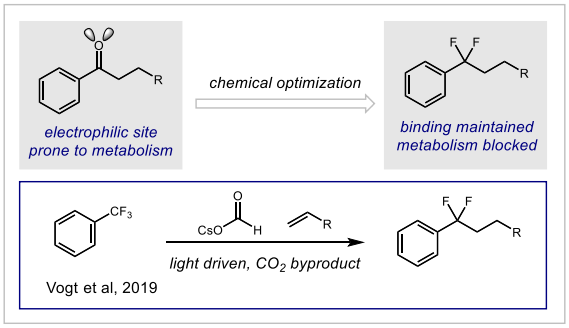

Figure 1.1 Defluorofunctionalization to access traditionally challenging pharmacophores

1

[2] Seath, C. P., Vogt, D. B., Xu, Z., Boyington, A. J., & Jui, N. T. (2018). Radical Hydroarylation of Functionalized Olefins and Mechanistic Investigation of Photocatalytic Pyridyl Radical Reactions. *Journal of the American Chemical Society*, *140*(45), 15525–15534. https://doi.org/10.1021/jacs.8b10238

[3] Vogt, D. B., Seath, C. P., Wang, H., & Jui, N. T. (2019). Selective C-F Functionalization of Unactivated Trifluoromethylarenes. *Journal of the American Chemical Society*, *141*(33), 13203–13211. https://doi.org/10.1021/jacs.9b06004

Defluorofunctionalization gives unprecedented access to functional groups such as $ArCF_2R$ and $ArCF_2H$ which have extraordinary biological properties but were previously extremely difficult and tedious to construct.[4] Recently, we have harnessed the same reactive intermediates to affect dearomitizative functionalization[5]; generating rigid, sp^3 rich frameworks for which there is high interest but poor access to currently (Figure 1.2).[6]

Figure 1.2 Spirocyclization produces rigid, sp^3 rich frameworks with concomitant generation of alkene synthetic handles.

In addition to advancing the understanding of aryl radicals, this body of work represents a series of new tools for medicinal chemists to improve compound quality. For instance, defluorofunctionalization offers blocking of metabolic sites while maintaining crucial binding interactions or a lipophilic hydrogen bond donor in the RCF_2H moiety. Dearomative cyclization explores new chemical space while increasing aqueous solubility and reducing metabolism when compared to an extended aryl system. The discovery of new chemical methods in this group has provided new access to biologically relevant molecular fragments and these pieces can improve physiochemical properties of drug molecules.

---

[4] Meanwell, N. A. (2018). Fluorine and Fluorinated Motifs in the Design and Application of Bioisosteres for Drug Design. In *Journal of Medicinal Chemistry* (Vol. 61, Issue 14, pp. 5822–5880). American Chemical Society. https://doi.org/10.1021/acs.jmedchem.7b01788

[5] Flynn, A. R., Mcdaniel, K. A., Hughes, M. E., Vogt, D. B., & Jui, N. T. (2020). Hydroarylation of Arenes via Reductive Radical-Polar Crossover. *Journal of the American Chemical Society*, *142*(20), 9163–9168. https://doi.org/10.1021/jacs.0c03926

[6] Lovering, F., Bikker, J., & Humblet, C. (2009). Escape from flatland: Increasing saturation as an approach to improving clinical success. *Journal of Medicinal Chemistry*, *52*(21), 6752–6756. https://doi.org/10.1021/jm901241e

1.2 Manipulation of chemical properties to better interrogate biological systems

A compound's chemical properties influence everything about its biological activity, from interactions with the protein of interest to the pharmacokinetic profile. Medicinal chemistry is working to optimize the properties that are lacking while avoiding erosion of a drug's beneficial elements. Without aqueous solubility, for instance, a compound is unlikely to be a successful or effective drug. Carrying out this optimization requires strong synthetic skills, altering the route or seeing new disconnections that may be different than the established path. This work also requires careful optimization of variables that are often inversely proportional to each other, finding a successful middle way when either extreme will produce a compound of little value. For these reasons, a group with demonstrated excellence in reaction optimization is a natural fit for compound optimization in medicinal chemistry.

1.3 Collaborative Multidisciplinary Science

We have successfully brought the skills of chemical optimization to projects across disciplines and schools at Emory University and beyond. Our group has worked alongside the Ortlund lab in Biochemistry and the Calvert lab at Emory Medicine to develop the most potent and efficacious agonists ever described for the orphan nuclear receptor liver receptor homolog-1 (LRH-1, NR5A2).[7] The molecules designed by our group and the optimization discussed herein are currently being expanded into external collaborations with pharmaceutical companies.

[7] Mays, S. G., Flynn, A. R., Cornelison, J. L., Okafor, C. D., Wang, H., Wang, G., Huang, X., Donaldson, H. N., Millings, E. J., Polavarapu, R., Moore, D. D., Calvert, J. W., Jui, N. T., & Ortlund, E. A. (2019). Development of the First Low Nanomolar Liver Receptor Homolog-1 Agonist through Structure-guided Design. *Journal of Medicinal Chemistry*, *62*(24), 11022–11034. https://doi.org/10.1021/acs.jmedchem.9b00753

Furthermore, we have applied our synthetic skills towards developing radioligands for diagnostic imaging of mutational status in tumors. Working with a team at Emory Department of Radiology and the Winship Cancer Institute, we have developed a molecule that lets oncologists visualize the tumors within a patient and see which if any will respond to immune checkpoint inhibitors, a revolutionary class of therapeutics. While the ultimate goals of the projects span a wide range of scientific space, the skills involved in developing a biologically active compound remain constant. Careful design, expert synthetic planning and execution, and critical review of the biologic data to inform optimization are a necessity to bring value to multidisciplinary teams.

Chapter 2

Visualizing Tumor Mutational Burden:

Development of Radioligands for PD-L1

Dr. Ronald Voll and Dr. Wone Woo Seo performed the radiochemistry, including adapting the fluorination conditions for use in the automated synthesizer. Weiping Yu performed the cell uptake and blocking studies. Lacey Perdue performed the surface plasmon resonance studies.

Abstract: Immuno-oncology therapeutics have revolutionized the way cancer is treated, improving survival while minimizing side effects. Anti-programmed cell death protein 1 (PD-1) and its ligand (PD-L1) antibodies are the premier example of immune-oncology therapeutics, with approvals in over 15 different indications. Yet it remains extremely difficult to determine which patients will respond to these therapies; the immunohistochemical assays currently utilized are error prone and subjectively scored. Positron emission tomography (PET) has been a mainstay of cancer diagnosis for several decades, utilizing ^{18}F-fluorodeoxyglucose to identify tumors based on high rates of glucose consumption. Recently, PET tracers have been developed that are specific to certain mutations or proteins, allowing oncologists to not only localize tumors, but also glean insights into treatment strategies for their patients. Here we disclose the design and development of a highly potent, soluble, and PD-L1 specific small molecule PET tracer to image PD-L1 expressing tumors.

2.1 Chemotherapeutic Agents in Oncology

Treating cancer with chemical agents was one of the biggest changes in medicine of the 20th century; the standard of care before 1940 was surgical resection, which was often aggressive enough to permanently disfigure patients.

2.1.1 Nitrogen Mustard

Repurposing the nitrogen mustard chemical weapons of the first World War to kill cancer cells allowed for the treatment of patients in a less aggressive fashion. The therapeutic effects of these compounds which had just been banned by the Geneva Convention was serendipitously discovered during autopsies of soldiers who had been exposed to mustard gas. The soldiers had substantial suppression of their lymph and bone marrow and the Navy physicians examining them hypothesized that these chemicals may be able to suppress the growth of malignancies of those same tissues. Working first with mice, they demonstrated that small, controlled dosing of mustard agents could selectively destroy lymphomas. In 1942, along with surgeon Gustaf Lindskog, they treated a lymphoma patient in New York. While the relief was temporary, for a time the man went into remission. Chemotherapy was born.

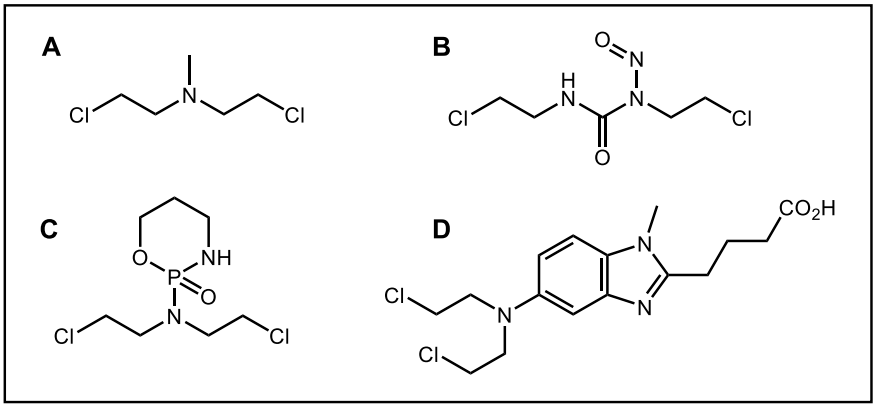

Figure 2.1 Nitrogen mustard chemotherapeutic drugs.
A) Mustine: original mustard chemotherapeutic, used infrequently today. B) carmustine (BiCNU): used in brain tumors as an implantable disc, slowly releasing the active pharmaceutical agent. C) Cyclophosphamide: prescribed today for lymphoma, leukemia and neuroblastoma. D) Bendamustine: prescribed for multiple myeloma and non-Hodgkin's lymphoma and is causes less hair loss.

2.1.2 Antifolates

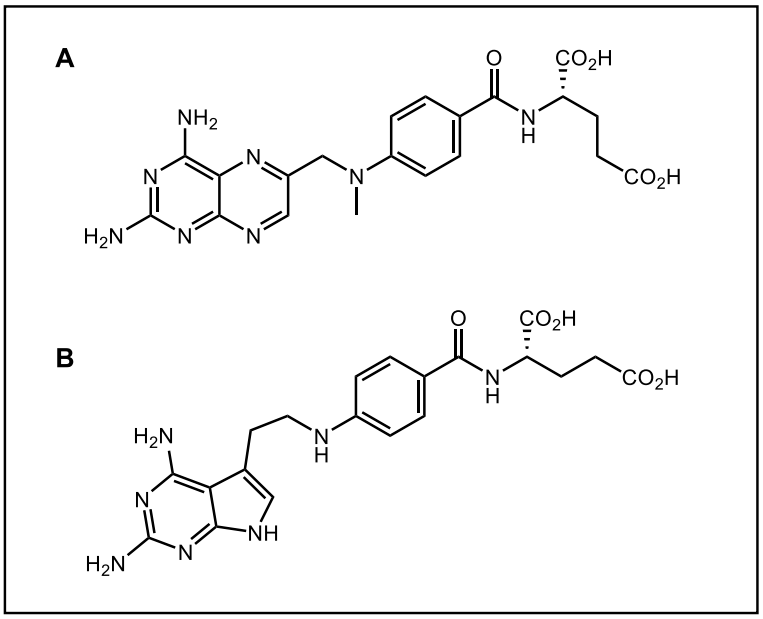

Figure 2.2. Antifolate Chemotherapeutics

A) Methotrexate: original antifolate drug used by Dr. Sidney Farber at Boston Children's Hospital. B) Pemetrexed: Developed at Princeton University, pemetrexed is an improved antifolate with some evidence of higher efficacy

Some years later, Dr. Sidney Farber was following up on a report that administering folate to leukemia patients seemed to make the cancer more aggressive. Dr. Farber went on to demonstrate that by administering antifolates, compounds with the ability to hamper folate metabolism and processing, the patients' disease would subside. The safest of these compounds, methotrexate is still prescribed to millions of patients every year. Antifolates prevent tumor cells from synthesizing nucleosides and thus prevent DNA replication. While all cells will have reduced replication rates, the cancer cells are impacted most severely as their replication rates are much higher than normal cells. It is notable that this discovery predates Roslin Franklin's Photo 51 and the subsequent publication by Watson and Crick by several years.

2.1.3 Natural products

During the early days of the field of molecular biology, the NIH appointed Dr. Gordon Zubrod to head the newly formed National Cancer Institute. Having previously discovered chloroquine to treat malaria for treating soldiers in the Pacific Theater of WWII, he was a natural fit for supercharging the institute's goal of developing further chemotherapeutic agents. During his tenure, the institute worked with a range of collaborators and developed therapies including taxanes (BMS), vinca alkaloids (Eli Lilly), camptothecins, and platinum based therapeutics (Michigan State University). These discoveries provided immense benefit to patients; however because all of them inhibit DNA synthesis in a broad sense, they also have concomitant side effects.

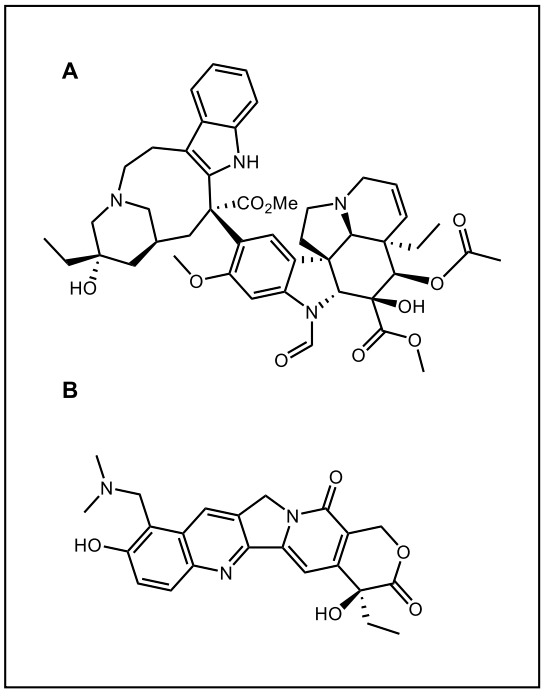

Figure 2.3 Natural product chemotherapeutics A) Vincristine, microtubule assembly inhibitor isolated from Madagascar periwinkle *Catharanthus roseus*. B) topotecan, water-soluble derivative of camptothecin a topoisomerase inhibitor isolated from *Cammptotheca acuminata*, a tree native to China

2.2 Targeted Therapies

The second half of the 20th century saw tremendous advancement in our understanding of the mechanisms involved in tumor development, culminating in the publication of the human genome. As these mechanisms were uncovered, therapeutic strategies were developed that could inhibit the growth of only the tumor cells, thereby limiting side effects.

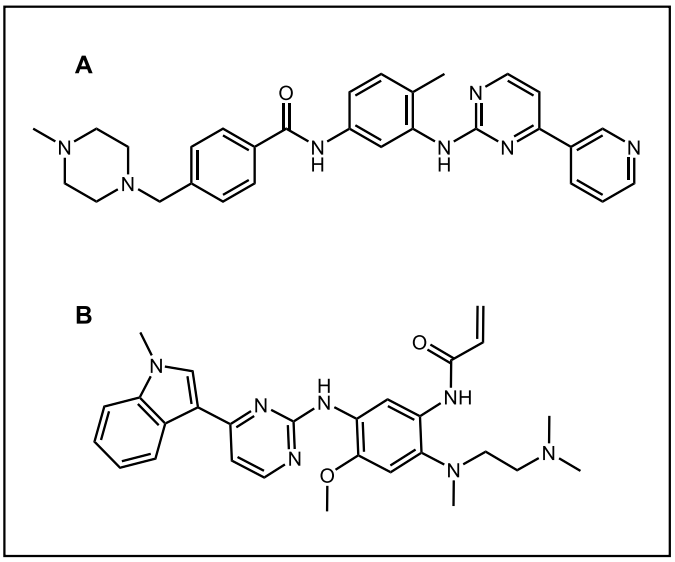

Figure 2.4 Targeted therapeutics
A) Imatinib (Gleevec) a BCR-Abl1 fusion protein inhibitor developed by Novartis. B) Osimertinib (Tagrisso) a T790M/L858R mutant selective EGFR inhibitor developed by Astra-Zeneca

One early "targeted therapeutic" was Gleevec (imatinib). Certain leukemias are highly correlated with a very specific fusion protein, BCR-ABL1. This fusion protein is only coded for after an aberrant chromosomal translocation (called the Philadelphia Chromosome). The resulting protein is a constitutively active tyrosine kinase, which causes uncontrolled cell cycle entry. Because this protein does not exist in healthy tissues it is a logical target for a wild type sparing therapeutic. Ultimately imatinib was optimized from a simple high throughput screen hit and is still prescribed today.

Targeted small molecule therapeutics continue to be developed today, with genotyping becoming cheaper and easier to perform thus allowing patients to receive therapies that are specific to their individual mutational burden.

2.3 The Immuno-Oncology Revolution

Sixty years before Sidney Farber was experimenting with antifolates in the basement of Boston Children's Hospital, Dr. William Coley was distraught over the death of one of his first patients. Despite providing her the standard of care for sarcoma (amputation of the affected limb), she later passed away due to metastases of the original tumor. This lead him to dig through the New York Hospital archives for cases of successful treatment of sarcoma. He stumbled upon

several cases where patients had become infected with *Streptococcus pyogenes* following their surgeries and peculiarly these patients were the ones who had fared better. He hypothesized that the infection itself is what was causing remission in these patients and sought to leverage the patient's immune system to fight tumors. When injected with live S. pyogenes, his patients did not fare well, with many passing away due to the infection. However, when a mixture of dead bacteria was used, coined "Coley's Toxin", the immune effects remained without the chance of infection. Dr. Coley never ran controlled studies on the therapeutic and it remains unclear whether there is a beneficial effect. Despite the lack of conclusive evidence that a mixture of dead bacteria confers a therapeutic benefit, the concept of treating cancer with a patient's own immune system was remarkable and would not be appreciated until well after his death in 1936. In 2005, almost one hundred years after his work, Pfizer licensed the technology with the hope of improving it and conclusively proving benefit.

2.3.1 Interleukin-2

In the 1970s, researchers had identified immune cells, including T cells, but it was profoundly difficult to study them. In contrast to other mammalian cell types, T cells would not continue to replicate in culture media. The solution to this problem was culturing the immune cells with a toxic lectin from red kidney beans, phytohemagglutinin (PHA). Once exposed to PHA, the T cells secreted a substance that could stimulate their growth, independent of the continued exposure to PHA. This signaling molecule was eventually isolated and was termed interleukin 2 (IL-2). Administration of IL-2 to tumor bearing mice caused their tumors to shrink, however the levels required for antitumor effects also displayed significant toxicity. Despite the side effect profile, the first studies in human cancer patients in 1985 provided conclusive evidence that cancer can be treated by recruitment of a patient's immune system.

2.4 Immune Checkpoint Inhibitors

2.4.1 CTLA-4

In 1987, a T cell receptor protein called cytotoxic T lymphocyte antigen 4 (CTLA-4) was first discovered. This protein binds the T cell receptor in a similar manner to CD-28, a stimulatory protein, however CTLA-4 is repressive. Early work in CTLA-4 knock out animals displayed an aggressive autoimmune phenotype, consistent with unencumbered activation of T cells. In the lab of Dr. James Allison, they envisaged that an anti-CTLA-4 antibody could be utilized in the treatment of cancer. In the late 1990s they performed a series of experiments using different tumor models (colon, prostate, breast, and skin) and showed high activity across all tumor types. These experiments proved the generality of anti-CTLA-4 mAb treatment. In 2004, working with the company Medarex, a humanizied form of the anti-CTLA-4 antibody was developed (ipilimumab). In 2016 Bristol-Meyers Squibb purchased Medarex and markets ipilimumab today as Yervoy.

2.4.2 PD-1/PD-L1

Meanwhile at the University of Kyoto, Tasuku Honjo's laboratory was working on proteins expressed during cell death. They isolated mRNA transcripts from cells that were undergoing apoptosis and named one of the proteins coded by the transcripts Programmed Cell Death 1 protein or PD-1. The function of this protein was a mystery for several years and knockout mice had a mild phenotype, only developing autoimmune disorders late in life. As the protein belonged to the CD28 family, along with CTLA-4, it was theorized that the protein was also a negative regulator of the immune system. Honjo then found the ligand for PD-1 (termed PD-L1, or programmed cell death ligand 1) and subsequent studies demonstrated that PD-L1 is expressed not only on immune cells, but many types of tumor cells. It became clear that tumors were expressing PD-L1 to avoid immune system surveillance. In the lab of Leiping Chen at Yale, antibodies to PD-1 and PD-L1

were developed and utilized in a series of preclinical experiments. They were able to prove that tumors were not subject to immune clearance when expressing PD-L1 but following administration of the anti-PD-L1 antibody the tumors would shrink. These experiments also showed that the autoimmune side effect profile was far milder than with the anti-CTLA-4 therapies. Honjo began a company, Ono Pharmaceuticals, which partnered with Bristol-Meyers Squibb to develop an anti-PD-1 therapy (nivolumab, Opdivo).

At the Dutch pharmaceutical company Organon, a second anti-PD-1 therapeutic was being developed. Following the purchase of Organon by Schering-Plough (and later Merck), this project was seen as a low priority and was being prepared for out licensing. Around this time the research team at Bristol-Meyers Squibb published an article describing the pronounced benefits of their anti-CTLA-4 and anti-PD-1 therapeutics, and Merck rushed to develop their nearly discarded anti-PD-1 project. Because the Bristol-Meyers Squibb program was substantially further along in development, the team at Merck elected to develop a companion diagnostic for PD-1. While this would limit the patient population for the therapy, it would allow them to run a smaller and faster clinical trial as the effect size would be larger. This gamble paid off and Merck's PD-1 inhibitor, pembrolizumab (Keytruda), received FDA approval several months before nivolumab was approved. In subsequent trials, Merck demonstrated efficacy and received approvals for many indications, including head and neck carcinoma, non-small cell lung cancer, melanoma, bladder cancer, and Hodgkin's lymphoma, among others. The side effect profile for pembrolizumab is quite mild, and the drug is extraordinarily effective; it has fundamentally changed how cancer is treated today.

2.4.3 Companion Diagnostics

Notably, pembrolizumab is the first therapeutic that is approved for treating tumors based on their genetic makeup, in contrast to the tissue of origin. The diagnostic test that was approved alongside the therapeutic (companion diagnostic) determines a patient's PD-1 expression level and if they qualify for pembrolizumab as a first line therapy.[8] Patients avoid rounds of therapy that may not provide benefit—the drug can only benefit patients if their tumors are using PD-1/PD-L1 to avoid immune surveillance. While the companion diagnostics work well for some patients, they unfortunately do not work for everyone.[9]

Companion diagnostics work based on a technique called immunohistochemistry—an assay based on antibody binding to a protein of interest[10]. First, a biopsy needle is used to remove a small piece of the tumor from a patient, then the tissue is fixed and sliced. Next, primary antibodies are placed on the tissue sample and bind to any PD-1 that is present. These primary antibodies are used as a handle for an enzyme tagged secondary antibody to bind to. Using the tagged enzyme, a color-generating reaction takes place and the amount of color produced is proportional to how much of

---

[8] Bellmunt J, De Wit R, Vaughn DJ, Fradet Y, Lee JL, Fong L, et al. Keynote-045: open-label, phase III study of pembrolizumab versus investigator's choice of paclitaxel, docetaxel, or vinflunine for previously treated advanced urothelial cancer. Society for Immunotherapy of Cancer (SITC) Annual Meeting. National Harbor, MD, 2016; Abstr 470.

[9] Kleinovink, J. W., Marijt, K. A., Schoonderwoerd, M. J. A., van Hall, T., Ossendorp, F., & Fransen, M. F. (2017). PD-L1 expression on malignant cells is no prerequisite for checkpoint therapy. *OncoImmunology*, *6*(4). https://doi.org/10.1080/2162402X.2017.1294299

[10] Teixidó, C., Vilariño, N., Reyes, R., & Reguart, N. (2018). PD-L1 expression testing in non-small cell lung cancer. In *Therapeutic Advances in Medical Oncology* (Vol. 10). SAGE Publications Inc. https://doi.org/10.1177/1758835918763493

the primary antibody bound to the protein of interest. The samples are then scored by a histologist[11].

While this "sandwich assay" technique can provide adequate specificity and sensitivity to some antigens, physicians have reported that PD-1/PD-L1 immunohistochemical assays are causing patients to go without a drug that may benefit them or being burdened financially with a drug that cannot help them.[12]

As the assay is based on a sample removed with a small biopsy needle, the results are limited by any sampling bias that may occur. As tumors are genetically heterogeneous, a small biopsy is unable to provide a complete picture of the expression levels. Furthermore, reduction in PD-1/PD-L1 expression has been shown to occur following removal of a sample from the tumor microenvironment. Due to the invasive nature of biopsy collection, samples generally cannot be collected serially; thus, these immunohistochemistry-based assays can provide only a snapshot of a patient's tumor. A technique that could quantify PD-1/PD-L1 expression levels throughout the body and in a noninvasive way would provide tremendous benefit to oncologists and their patients.

---

[11] Rimm, D. L., Han, G., Taube, J. M., Yi, E. S., Bridge, J. A., Flieder, D. B., Homer, R., West, W. W., Wu, H., Roden, A. C., Fujimoto, J., Yu, H., Anders, R., Kowalewski, A., Rivard, C., Rehman, J., Batenchuk, C., Burns, V., Hirsch, F. R., & Wistuba, I. I. (2017). A prospective, multi-institutional, pathologist-based assessment of 4 immunohistochemistry assays for PD-L1 expression in non–small cell lung cancer. *JAMA Oncology*, *3*(8), 1051–1058. https://doi.org/10.1001/jamaoncol.2017.0013

[12] Kulangara, K., Zhang, N., Corigliano, E., Guerrero, L., Waldroup, S., Jaiswal, D., Jansson, M., Shah, S., Hanks, D., Wang, J., Lunceford, J., Savage, M. J., Juco, J., & Emancipator, K. (n.d.). *Clinical Utility of the Combined Positive Score for Programmed Death Ligand-1 Expression and the Approval of Pembrolizumab for Treatment of Gastric Cancer*. https://doi.org/10.5858/arpa.2018-0043

2.5 Positron Emission Tomography

Positron emission tomography (PET) is a medical imaging technique that was developed in the 1950s and relies on detecting the energy released during a positron annihilation event.

Positron emission tomography utilizes specifically labeled pharmaceutical agents to probe biologic systems[13]. To image a protein of interest, a ligand for that protein is tagged with a radionuclide (forming a radioligand). The radioligand is then administered to the patient and binds to the protein. Meanwhile, the radionuclide is decaying through positron emission; a proton is becoming a neutron with a concomitant loss of its positive charge, the positron.

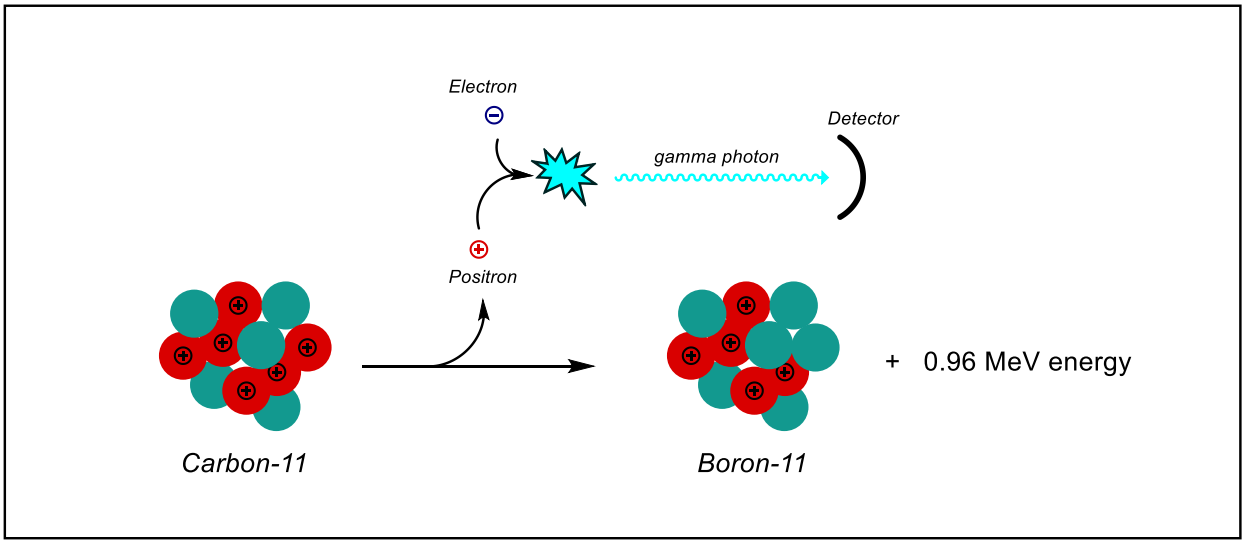

Figure 2.5 Positron emission and annihilation

These positrons that are emitted will annihilate with the first electron they collide with, releasing a high energy photon which can be detected (Figure 2.5). In a biological system, that annihilation event is nearly instantaneous and therefore the photon is emitted from precisely the

[13] Ghasemi, M., Nabipour, I., Omrani, A., Alipour, Z., & Assadi, M. (2016). Precision medicine and molecular imaging: new targeted approaches toward cancer therapeutic and diagnosis. In *Am J Nucl Med Mol Imaging* (Vol. 6, Issue 6). www.ajnmmi.us/ISSN:2160-8407/ajnmmi0039837

location where the radioligand is positioned[14]. The patient is imaged for several half-lives of radioactive decay and then a three-dimensional map of all the individual annihilation events is reconstructed. This allows radiologists to determine location and quantify the protein of interest within a patient.

Radionuclide	Half life (minutes)
^{11}C	20.36
^{13}N	9.97
^{15}O	2.03
^{18}F	109.9

Table 1 Half-lives of common radioisotopes

Because many of these isotopes have extremely short half-lives (on the order of minutes, Table 1) they generally are prepared soon before a patient is imaged. Common isotopes include ^{11}C, ^{13}N, ^{15}O, and ^{18}F[15]. Radiology labs that perform positron emission tomography imaging are usually located near the cyclotron that is required to produce the radioisotopes. To produce ^{18}F-, water enriched in ^{18}O is bombarded with high energy protons. From there, the ^{18}F is incorporated into the radioligand and transferred to the clinical labs for administration and imaging.

PET imaging utilizing fluorodeoxyglucose (FDG), a sugar molecule that has had ^{18}F incorporated, has been used extensively in imaging tumors, the brain, skeletal system, and the heart[16]. Cancer cells often utilize different metabolic pathways than normal cells and consume

[14] Basu S, Kwee TC, Surti S, Akin EA, Yoo D, Alavi A. Fundamentals of PET and PET/CT imaging. Ann N Y Acad Sci. 2011 Jun;1228:1-18. doi: 10.1111/j.1749-6632.2011.06077.x. PMID: 21718318.

[15] Choe YS, Lee KH. PET Radioligands for Imaging of Tau Pathology: Current Status. *Nucl Med Mol Imaging*. 2015;49(4):251-257. doi:10.1007/s13139-015-0374-9

[16] Yu S. Review of F-FDG Synthesis and Quality Control. *Biomed Imaging Interv J*. 2006;2(4):e57. doi:10.2349/biij.2.4.e57

abnormally high amounts of glucose (known as the Warburg Effect[17]). As a radiolabeled sugar

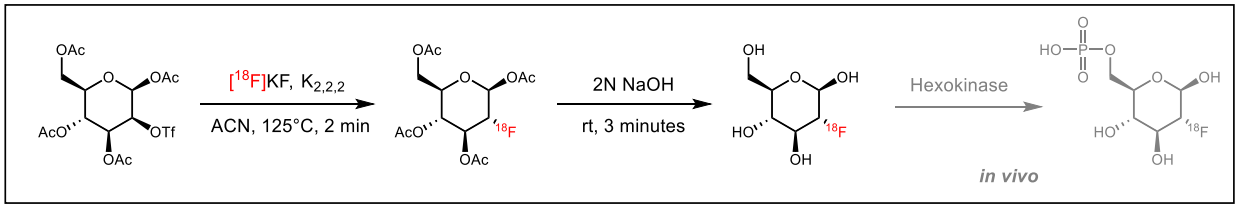

Scheme 1 Radiolabeling of fluorodeoxyglucose (FDG)

molecule, FDG is taken up by cancer cells at much higher levels than normal cells. Once inside the cells, FDG is phosphorylated by hexokinase as the cell attempts to feed it into the Krebs Cycle, however it is lacking a necessary oxygen and is not competent in glucose catabolism. Glucose phosphates are extremely polar and unable to exit the cell; thus, the radiolabel is trapped within the cancer cells (Scheme 1). FDG is prepared in two synthetic steps from acetyl protected mannose triflate. In the presence of a cryptand ligand, the fluoride is nucleophilic and will displace the alkyl triflate group. Subsequently the acetyl protecting groups are hydrolyzed and the compound administered to patients. Once a specialist technique, in 2019 more than two million PET scans were collected and around 90% of those scans utilized FDG as the radiotracer[18].

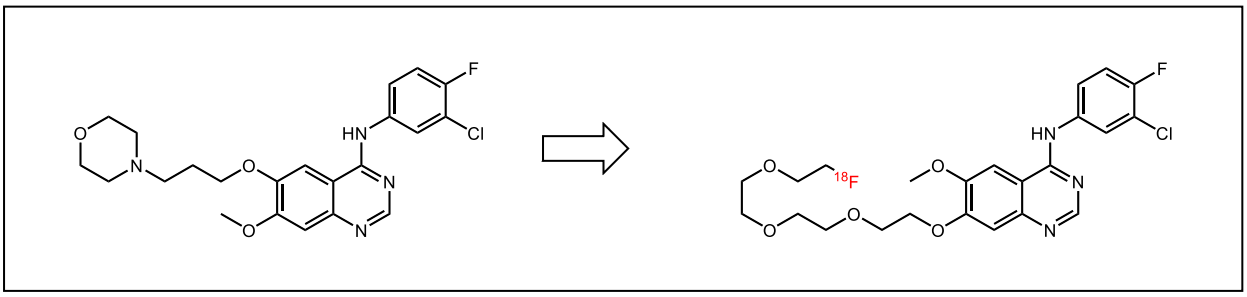

Figure 2.6 Radioligand development for EGFR mutant tumors

In recent years, several studies have been published describing the use of PET ligands to detect and quantify the presence of tumors overexpressing key cancer drivers. Overactive

[17] Warburg O PK, Negelein E. Uber den stoffwechsel der carcinomzelle. Biochem Zeitschrift. 1924;152:309–335.

[18] "PET/CT drives PET scan volume to new heights". Lorna Young, IMV Medical Information Market Research

Epidermal growth factor receptor (EGFR) is one of the most common mutations that drives lung cancer (the cancer type responsible for the most deaths per year). Many tyrosine kinase inhibitors (TKIs) have been developed to inhibit the activity of EGFR, however not all patients will respond to them. FDG-PET is already widely used for staging and diagnosing NSCLC, and researchers at Stanford University and Harbin Medical School have leveraged PET to determine whole-body EGFR expression levels in patients[19]. They first generated a radioligand that is a derivative of a known EGFR binding compound (Figure 2.6), incorporating radioactive fluoride through displacement of an alkyl sulfonate group. Then, using both FDG and then ^{18}F-MPG, they generated a mutation agnostic scan for tumors (FDG) and could overlay that image with the 18F-MPG image to determine which of those tumors would bind EGFR TKIs and thus respond to treatment. Using this technology in a clinical trial, they were able to show that a potential responder, identified with ^{18}F-MPG, was able to go into remission following a course of treatment with EGFR drug gefitinib. This study conclusively proves the power of using PET to determine specific mutations and evaluate potential therapies; the patients in that study and their oncologists were able to "see into the future" to determine their likely response to a drug without exposing them to any of the side effects or wasting time that could have been used to administer a treatment they would respond to.

A positron emission tomography ligand for imaging PD-1/PD-L1 would be of tremendous value. By detecting the expression level of the protein within the tumor microenvironment there is no change in expression levels, something that plagues companion diagnostics. The readout is the result of one binding event, rather than a series of multiple steps that need to work properly to

[19] Sun, X; Xiao, Z; Chen, G; Han, Z; Liu, Y; Zhang, C; Sun, Y; Song, Y; Wang, K; Fang, F; Wang, X; Lin, Y; Xu, L; Shao, L; Li, J; Cheng, Z; Gambhir, S; Shen, B. A PET imaging approach for determining EGFR mutation status for improved lung cancer patient management. *Sci. Transl. Med* 2018, (10), 431

provide a signal, which increases assay robustness. As an imaging technique, PET is noninvasive and can be performed multiple times to monitor a patient's regression or properly time PD-1/PD-L1 combination therapies, which has been shown to have an impact on patient outcomes.

Because of the ubiquity of FDG PET capabilities, researchers have attempted to leverage machine learning to correlate FDG PET artifacts with PD-L1 expression.[20] While these studies highlight the importance of PD-1/PD-L1 diagnostic imaging, the predictive capabilities of the models are insufficient for a clinical setting[21].

^{89}Zr labeled anti-PD-L1 antibodies have been developed to attempt to solve some of the problems associated with IHC assays (Figure 2.7), but they are far from an ideal solution.[22] ^{89}Zr

---

[20] A) Takada, K., Toyokawa, G., Tagawa, T., Kohashi, K., Akamine, T., Takamori, S., Hirai, F., Shoji, F., Okamoto, T., Oda, Y., & Maehara, Y. (2017). Association between PD-L1 Expression and Metabolic Activity on 18F-FDG PET/CT in Patients with Small-sized Lung Cancer. *Anticancer Research*, *37*(12), 7073–7082. https://doi.org/10.21873/anticanres.12180.

B) Chen, R. Y., Lin, Y. C., Shen, W. C., Hsieh, T. C., Yen, K. Y., Chen, S. W., & Kao, C. H. (2018). Associations of Tumor PD-1 Ligands, Immunohistochemical Studies, and Textural Features in 18F-FDG PET in Squamous Cell Carcinoma of the Head and Neck. *Scientific Reports*, *8*(1). https://doi.org/10.1038/s41598-017-18489-2.

C) Chen, R., Zhou, X., Liu, J., & Huang, G. (2019). Relationship between the expression of PD-1/PD-L1 and 18 F-FDG uptake in bladder cancer. *European Journal of Nuclear Medicine and Molecular Imaging*, *46*(4), 848–854. https://doi.org/10.1007/s00259-018-4208-8

[21] Togo, M., Yokobori, T., Shimizu, K., Handa, T., Kaira, K., Sano, T., Tsukagoshi, M., Higuchi, T., Yokoo, S., Shirabe, K., & Oyama, T. (2020). Diagnostic value of 18F-FDG-PET to predict the tumour immune status defined by tumoural PD-L1 and CD8+tumour-infiltrating lymphocytes in oral squamous cell carcinoma. *British Journal of Cancer*, *122*(11), 1686–1694. https://doi.org/10.1038/s41416-020-0820-z

[22] Donnelly, D. J., Adam Smith, R., Morin, P., Lipovsek, D., Gokemeijer, J., Cohen, D., Lafont, V., Tran, T., Cole, E. L., Wright, M., Kim, J., Pena, A., Kukral, D., Dischino, D. D., Chow, P., Gan, J., Adelakun, O., Wang, X. T., Cao, K., … Hayes, W. (2018). Synthesis and biologic evaluation of a novel 18 F-labeled adnectin as a PET radioligand for imaging PD-L1 expression. *Journal of Nuclear Medicine*, *59*(3), 529–535. https://doi.org/10.2967/jnumed.117.199596

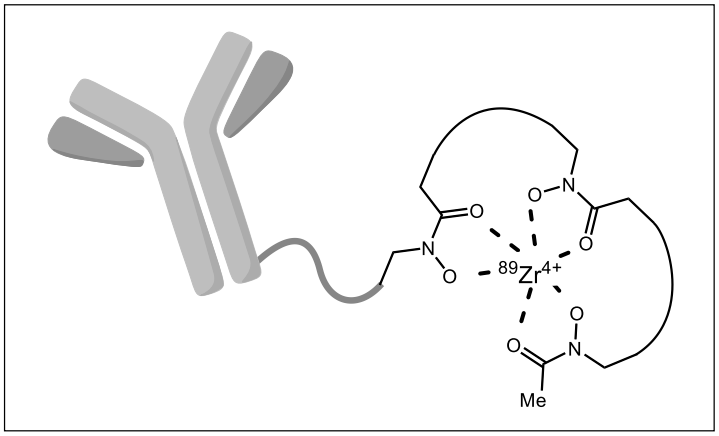

Figure 2.7 ^{89}Zr tagged nivolumab has been studied in humans for imaging PD-L1 with PET

decays primarily through electron capture (vs positron emission, 77% to 23% respectively) resulting in low signal, as well as emission of background-generating high energy gamma rays. Additionally, the positron range is larger than ^{18}F, limiting the spatial resolution as well as the contrast of the PET scan. Furthermore, the pharmacokinetic properties of antibodies require tracer administration on a separate day than imaging (ca. 5 days earlier), which creates high radiation exposure and an undue compliance burden on patients[23].

In comparison to ^{89}Zr, which requires a cyclotron facility to produce the radionuclide, gallium-68 can be readily generated in a benchtop apparatus. Despite the half-life of ^{68}Ga being too short for transport ($T_{1/2}$: 68 minutes), it is a daughter nuclide of a much longer-lived radioactive metal, ^{68}Ge ($T_{1/2}$ 271 days). To produce ^{68}Ga, a sample of ^{68}Ge is adsorbed onto an alumina cartridge and as it decays, the ^{68}Ga can be eluted off the column with dilute hydrochloric acid. This solution of $^{68}GaCl_3$ can then be complexed to a tracer that contains an aminopolycarboxylic acid ligand (APCL, e.g. DOTA or NOTA, Figure 2.8) and injected for imaging. A common way to attach the ligand

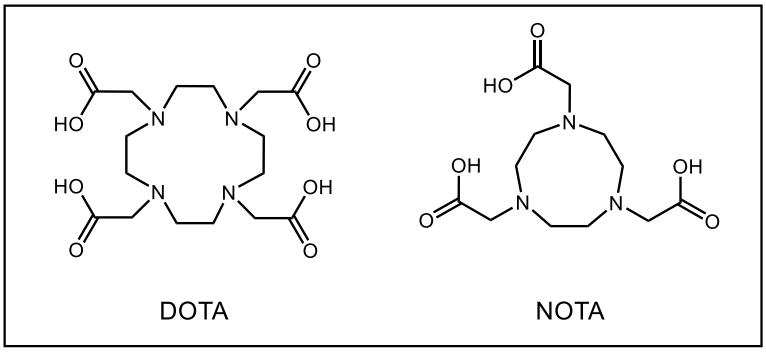

Figure 2.8 Aminopolycarboxylic acid ligands commonly used for ^{68}Ga and ^{64}Cu labeling of peptides, nanobodies, and antibodies

[23] Dunphy, M. P. S., & Pillarsetty, N. (2020). The unique pharmacometrics of small molecule therapeutic drug tracer imaging for clinical oncology. In *Cancers* (Vol. 12, Issue 9, pp. 1–16). MDPI AG. https://doi.org/10.3390/cancers12092712

to a protein binder, such as an antibody or nanobody, is through cysteine conjugation to a maleimide reactive handle. Several groups have used this approach to facilitate PD-L1 imaging via PET, utilizing PD-L1 binding nanobodies[24]. While the convenient generation of the ^{68}Ga radionuclide facilitates utilization of this strategy at a much wider range of clinics, the conjugate addition that tethers the ^{68}Ga-APCL complex to the nanobody is a reversible reaction and in the presence of nucleophiles such as water, the PD-L1 binding moiety and the radionuclide can dissociate[25]. The dissociation is doubly harmful to the image resolution; the cold PD-L1 nanobody acts as a "blocker" to the labeled antibody and the ^{68}Ga complex is free to circulate before being cleared by the kidneys.

[24] Liu, Q., Jiang, L., Li, K., Li, H., Lv, G., Lin, J., & Qiu, L. (2021). Immuno-PET imaging of 68Ga-labeled nanobody Nb109 for dynamic monitoring the PD-L1 expression in cancers. *Cancer Immunology, Immunotherapy*, *70*(6), 1721–1733. https://doi.org/10.1007/s00262-020-02818-y

[25] Chigoho, D. M., Lecocq, Q., Awad, R. M., Breckpot, K., Devoogdt, N., Keyaerts, M., Caveliers, V., Xavier, C., & Bridoux, J. (2021). Site-Specific Radiolabeling of a Human PD-L1 Nanobody via Maleimide–Cysteine Chemistry. *Pharmaceuticals*, *14*(6), 550. https://doi.org/10.3390/ph14060550

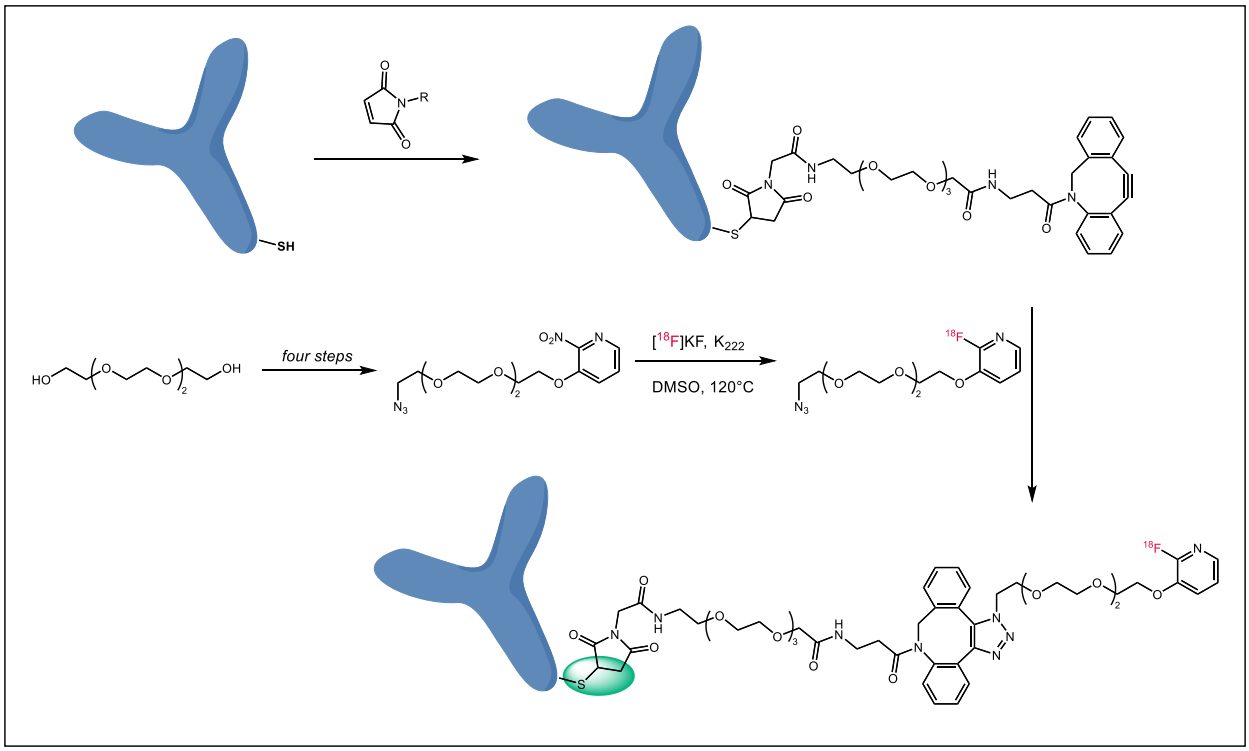

Figure 2.9 Adnectin based ^{18}F PD-L1 PET tracer. Thiol conjugate addition attached the ring-strained cyclooctyne handle which is "clicked" onto an 18F containing prosthetic group. The hydrolytically labile bond is highlighted in green.

^{18}F based tracers avoid the resolution problems inherent to metal radionuclide tracers, allow for lower radiation doses, and can be produced at the laboratories that currently produce FDG. These properties make them far more attractive for diagnostic development. One approach is to use a small antibody-like protein to bind PD-L1 and tether to it a small molecule containing ^{18}F, providing the resolution of ^{18}F tracers with the specificity of the antibody approach. Numerous iterations of this idea have been published, the most developed of which, 18F-BMS-986192[26], is

[26] Niemeijer, A. N., Leung, D., Huisman, M. C., Bahce, I., Hoekstra, O. S., van Dongen, G. A. M. S., Boellaard, R., Du, S., Hayes, W., Smith, R., Windhorst, A. D., Hendrikse, N. H., Poot, A., Vugts, D. J., Thunnissen, E., Morin, P., Lipovsek, D., Donnelly, D. J., Bonacorsi, S. J., … de Langen, A. J. (2018). Whole body PD-1 and PD-L1 positron emission tomography in patients with non-small-cell lung cancer. *Nature Communications*, *9*(1). https://doi.org/10.1038/s41467-018-07131-y

based on an Adnectin platform (Figure 2.9).[27] As the proteins that recognize and bind PD-L1 have an array of acidic functional groups on them which are not tolerated under the labeling conditions, these molecules must be synthesized modularly. The small molecule fragment is prepared in several steps, labeled with ^{18}F, then the solvent is removed and replaced with water to not denature the adnectin. That solution of ^{18}F labeled compound is then conjugated to the PD-L1 binding portion of the molecule before purification and then dosing. The synthesis of these compounds requires multiple steps with material that is rapidly decaying. A more ideal tracer would install fluorine in the last or penultimate step in order to prevent unnecessary decay.

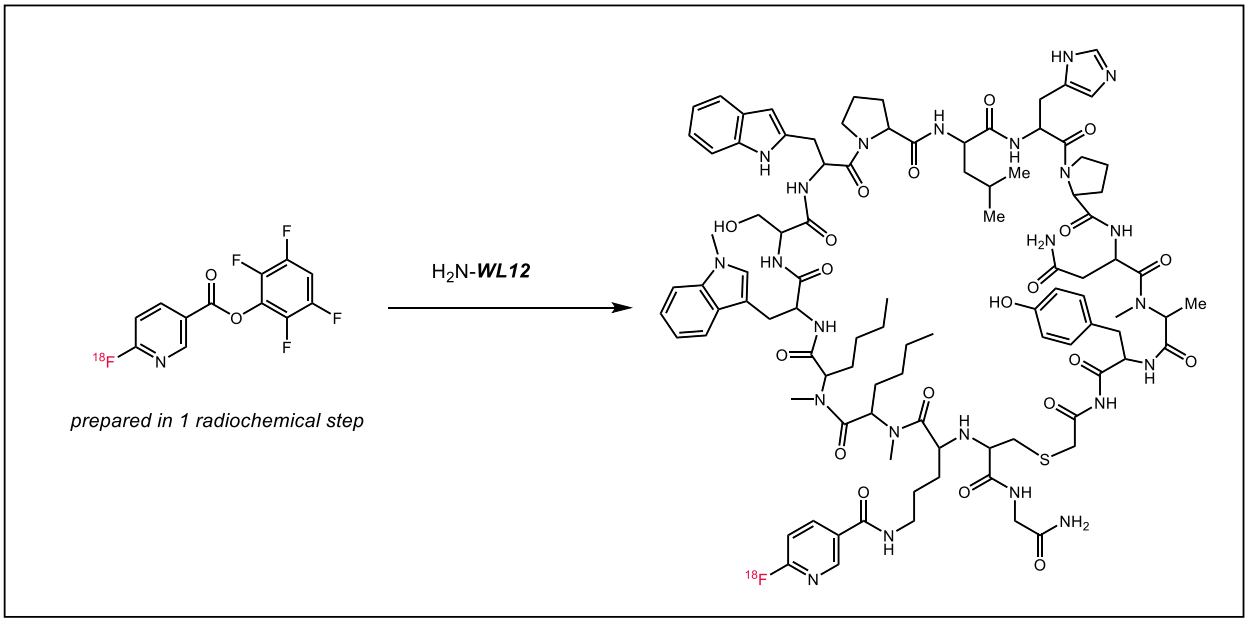

Figure 2.10 ^{18}F radiochemical labeling of PD-L1 binding peptide WL12 utilizing the FPy-TFP prosthetic group

Discovered in the Nimmagadda lab, a small peptide (WL12) has been used extensively for imaging PD-L1 and they have done so utilizing different radionuclides. WL12 possesses high

[27] Lipovsek D. Adnectins: engineered target-binding protein therapeutics. *Protein Eng Des Sel*. 2011;24(1-2):3-9. doi:10.1093/protein/gzq097

affinity for PD-L1 (22 nM) and is amenable to incorporation of ^{64}Cu[28], ^{68}Ga[29], as well as ^{18}F.[30] The results of these studies provide a controlled manner to compare the benefits of different radionuclides. When labeled with ^{64}Cu, the authors noted high hepatic uptake, likely due to copper transchelation, which potentially obfuscates hepatic metastases (occurring in 13% of patients with metastatic non-small cell lung cancer). A later report using ^{68}Ga-WL12 provided far superior contrast and facile synthesis (vide supra), however those benefits came at the expense of increased clearance. Most recently, peptide has been labeled with 18F, utilizing the [18F]FPy-TFP prosthetic group strategy developed by Olberg et al (Figure 2.10).[31] Despite this prosthetic being less hydrophobic than previous generations, ^{18}F-Fpy-WL12 was considerably more hydrophobic than ^{68}Ga-DOTA-WL12 and showed higher hepatic, renal and normal tissue uptake as a result. Furthermore, ^{18}F-Fpy-WL12 suffered from low specific activity, presumably a function of ^{19}F displacement arising from the fluorinated leaving group in the prosthetic radiosynthesis.

---

[28] Jiang, J., Li, D., Liu, T., Xia, L., Guo, X., Meng, X., Liu, F., Wang, F., Yang, Z., & Zhu, H. (2021). Noninvasive evaluation of PD-L1 expression using Copper 64 labeled peptide WL12 by micro-PET imaging in Chinese hamster ovary cell tumor model. *Bioorganic and Medicinal Chemistry Letters*, *40*. https://doi.org/10.1016/j.bmcl.2021.127901

[29] de Silva, R. A., Kumar, D., Lisok, A., Chatterjee, S., Wharram, B., Venkateswara Rao, K., Mease, R., Dannals, R. F., Pomper, M. G., & Nimmagadda, S. (2018). Peptide-Based 68 Ga-PET Radiotracer for Imaging PD-L1 Expression in Cancer. *Molecular Pharmaceutics*, *15*(9), 3946–3952. https://doi.org/10.1021/acs.molpharmaceut.8b00399

[30] Lesniak, W. G., Mease, R. C., Chatterjee, S., Kumar, D., Lisok, A., Wharram, B., Kalagadda, V. R., Emens, L. A., Pomper, M. G., & Nimmagadda, S. (2019). Development of [18F]FPy-WL12 as a PD-L1 Specific PET Imaging Peptide. *Molecular Imaging*, *18*. https://doi.org/10.1177/1536012119852189

[31] Olberg, D. E., Arukwe, J. M., Grace, D., Hjelstuen, O. K., Solbakken, M., Kindberg, G. M., & Cuthbertson, A. (2010). One step radiosynthesis of 6-[18F]fluoronicotinic acid 2,3,5,6-tetrafluorophenyl ester ([18F]F-Py-TFP): A new prosthetic group for efficient labeling of biomolecules with fluorine-18. *Journal of Medicinal Chemistry*, *53*(4), 1732–1740. https://doi.org/10.1021/jm9015813

A recent publication detailed the single step synthesis of an ^{18}F small molecule tracer for PD-L1, based on small molecule PD-L1 binding compounds disclosed by BMS (Figure 2.11).[32] These compounds provide the desired single step approach to labeling; however, the tumor-to-background signal was poor due to nonspecific binding of the extremely hydrophobic tracer. Further reducing the utility of the developed radioligand was poor tracer uptake in tumors relative to kidney, liver, heart, and bone (ca. 1% ID/g in tumor vs 18% in kidney).

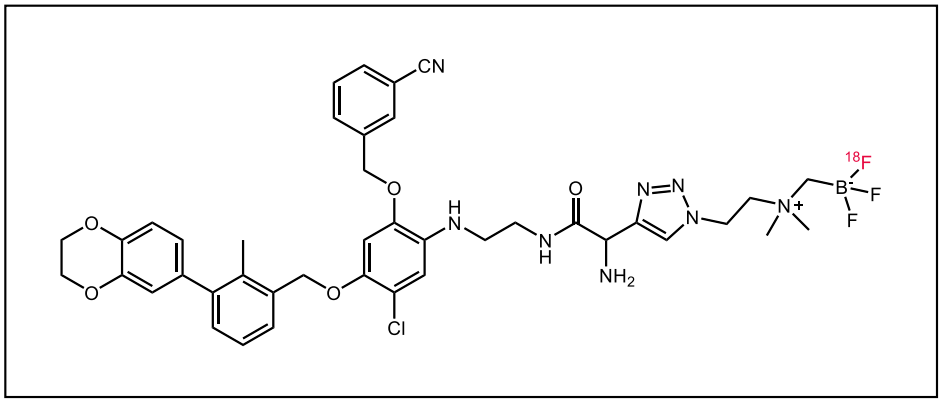

Figure 2.11 First disclosed ^{18}F Small molecule PD-L1 PET tracer

Despite progress towards a PD-L1 PET radiotracer, there continues to be unmet need for a radiotracer that can provide the high-resolution images needed for accurate diagnoses and patient monitoring[33]. An 18F radioligand derived from small molecule inhibitors is the ideal solution to that problem.

[32] Miao, Y., Lv, G., Chen, Y., Qiu, L., Xie, M., & Lin, J. (2020). One-step radiosynthesis and initial evaluation of a small molecule PET tracer for PD-L1 imaging. *Bioorganic and Medicinal Chemistry Letters*, *30*(24). https://doi.org/10.1016/j.bmcl.2020.127572

[33] Wierstra, P., Sandker, G., Aarntzen, E., Gotthardt, M., Adema, G., Bussink, J., Raavé, R., & Heskamp, S. (2019). Tracers for non-invasive radionuclide imaging of immune checkpoint expression in cancer. *EJNMMI Radiopharmacy and Chemistry*, *4*(1). https://doi.org/10.1186/s41181-019-0078-z

2.6 Small Moleucle Inhibitors of PD-L1

PD-L1 has been extensively targeted utilizing antibodies, however there are no approved PD-L1 small molecule drugs. Small molecules present significant benefits over antibody therapies, including oral dosing, shelf stability, and shorter in vivo half-lives. As a result, there are many reports of preclinical small molecule inhibitors of PD-L1.

2.6.1 Disclosed Inhibitors of PD-L1

Aurigene

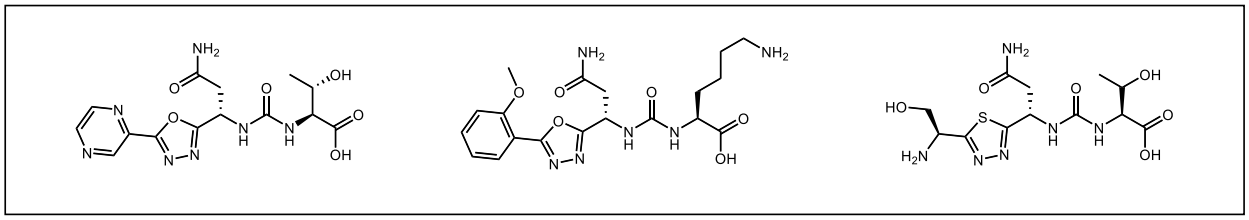

Figure 2.12 Compounds disclosed by Aurigene Discovery Technologies Limited

Based in Bangalore, India, researchers at Aurigene Discovery Technologies Limited have designed and tested a series of small peptide mimetics (Figure 2.12).[34] These compounds, which are built up around an oxadiazole or thiadiazole core, are highly effective in a splenocyte proliferation assay. These compounds are a distinct structural class from the remainder of the PD-1/PD-L1 targeting chemical matter, and studies have questioned their mechanism of action. They have been found to not bind PD-1/PD-L1 and their efficacy is due to other pharmacologic activity.

[34] Aurigene Discovery Technologies Limited. 1,3,4-oxadiazole and1,3,4-thiadiazole derivatives as immunomodulators.WO2015/033301 A1.2015. Aurigene Discovery Technologies Limited. 3-substituted 1,3,4-oxa-diazole and thiadiazole compounds as immunomodulators.WO2016/142894 A1.2016.Scheme 15.Cyclic peptides and examples patented by Aurigene Ltd.676S. SHAABANI ET AL.

BMS

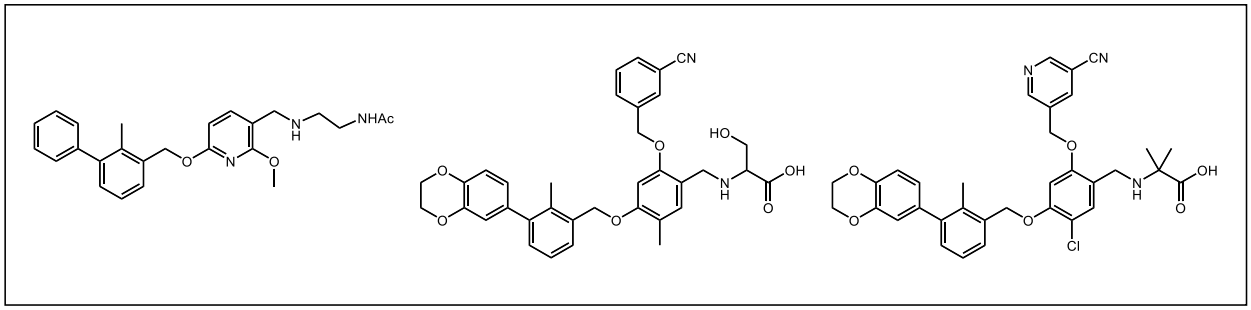

Figure 2.13 Compounds disclosed by Bristol-Meyers Squibb

Bristol-Meyers Squibb, the company first interested in producing an anti-PD-1/PD-L1 therapeutic, has published most prolifically in this space.[35] There are many patents assigned to the company detailing anti PD-1/PD-L1 small molecules. These compounds generally all have a similar structure, involving a central ring that has hydrophobic moieties attached on one side and hydrophilic moieties attached on the other (Figure 2.13). A subset of them has another electron poor aryl ring attached to the central arene, with a notable increase in the potency for those analogs (IC_{50} 10^{-9} M vs 10^{-7} – 10^{-8} M). Later disclosures cover compounds that are C2 symmetric, dimerized about the central arene unit.

Polaris Pharmaceuticals and Chemocentryx, Inc.

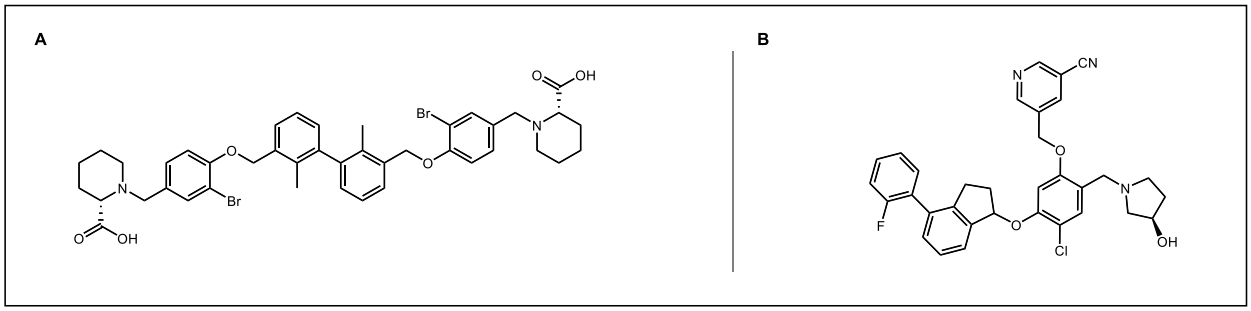

Figure 2.14 Compounds disclosed by Polaris Pharmaceuticals (A) and Chemocentryx, Incorporated (B)

[35] Bristol-Myers Squibb Company. Compounds useful as immunomo-dulators.WO2015/034820 A1.2015. Bristol-Myers Squibb Company. Compounds useful as immunomo-dulators.WO2015/160641 A2.

Patents issued to these two companies[36] are largely derivative of the chemical matter developed by Bristol-Meyers Squibb, either functionalized dimers or modifications of the hydrophobic arene unit (Figure 2.14).

Incyte

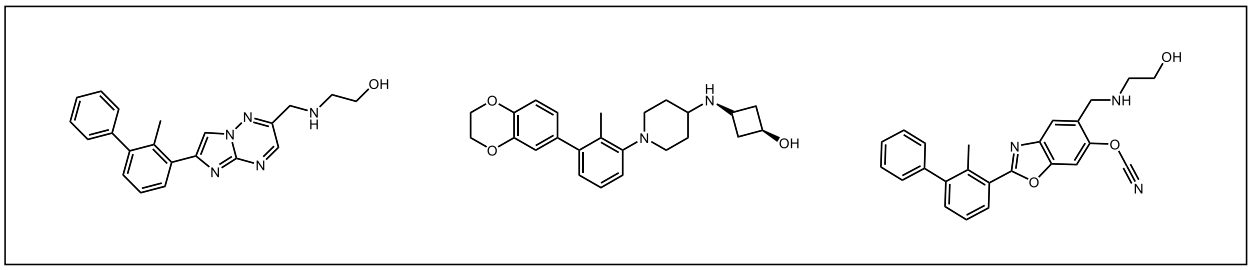

Figure 2.15 Compounds disclosed by Incyte Corporation

While the compounds claimed by Incyte have features consistent with the Bristol-Meyers Squibb compounds (hydrophobic region – aryl linker – hydrophilic region) they are chemically distinct, incorporating heterocycles which lower the overall hydrophobicity of the analogs (Figure 2.15).[37] These structural improvements culminated in the first oral PD-L1 drug to enter clinical trials (INCB086550, structure not disclosed).

Macrocyclic Inhibitors

There have been several reports of macrocyclic PD-1/PD-L1 inhibitors, built with a peptide backbone. The macrocyclics have IC_{50} values comparable to the other small molecule inhibitors.

[36] Polaris Pharmaceuticals, Inc. Immune checkpoint inhibitors, com-positions and methods there for.WO2018/045142 A1.2018. Chemocentryx, Inc. Immunomodulator compounds.WO2018/005374 A1.2018. Incyte Corporation. Heterocyclic compounds as immunomodula-tors.US2017/0107216 A1.2017. Incyte Corporation. Heterocyclic compounds as immunomodula-tors.WO2017/070089A1.2017.

[37] Incyte Corporation. Heterocyclic compounds as immunomodula-tors.WO2017/205464 A1.2017

2.7 Structural Biology of PD-1/PD-L1 Antagonism

The first reported cocrystal of a PD-L1 antagonist bound to the protein utilized a compound developed by Bristol-Meyers Squibb[38,39]. Upon small molecule binding, the protein has been demonstrated to dimerize; a phenomenon observed in both X-ray crystallographic data as well as in-vitro in the cell membrane. A later report shows that this dimerization triggers internalization and degradation of the PD-L1, likely the complete mechanism of action of these compounds, which contradicts previous reports hypothesizing that the dimerization event prevented PD-1/PD-L1 binding[40]. The solved crystal structures of Bristol-Meyers Squibb's compounds highlight key features involved in the binding of small molecules to PD-L1.

[38] Guzik, K., Zak, K. M., Grudnik, P., Magiera, K., Musielak, B., Törner, R., Skalniak, L., Dömling, A., Dubin, G., & Holak, T. A. (2017). Small-Molecule Inhibitors of the Programmed Cell Death-1/Programmed Death-Ligand 1 (PD-1/PD-L1) Interaction via Transiently Induced Protein States and Dimerization of PD-L1. *Journal of Medicinal Chemistry*, *60*(13), 5857–5867. https://doi.org/10.1021/acs.jmedchem.7b00293

[39] Konstantinidou M, Zarganes-Tzitzikas T, Magiera-Mularz K, et al.Immune checkpoint PD-1/PD-L1: is there life beyond antibodies?Angew Chemie - Int Ed.2018;57:4840–4848.

[40] Park, J. J., Thi, E. P., Carpio, V. H., Bi, Y., Cole, A. G., Dorsey, B. D., Fan, K., Harasym, T., Iott, C. L., Kadhim, S., Kim, J. H., Lee, A. C. H., Nguyen, D., Paratala, B. S., Qiu, R., White, A., Lakshminarasimhan, D., Leo, C., Suto, R. K., … Moore, C. B. (2021). Checkpoint inhibition through small molecule-induced internalization of programmed death-ligand 1. *Nature Communications*, *12*(1). https://doi.org/10.1038/s41467-021-21410-1

Solvent Exposed Region

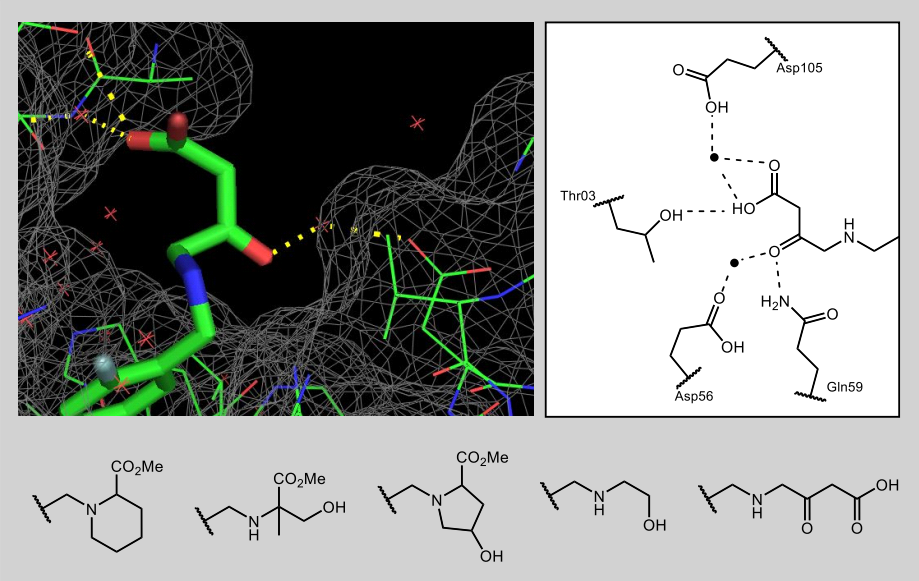

Figure 2.16 Key binding elements in the solvent exposed region of PD-L1 dimer

The proximal end of published small molecule inhibitors frequently contain highly hydrophobic moieties, including amino alcohols and amino acids (Figure 2.16). This portion of the molecule, when bound, is solvent exposed and provides a crucial handle for modulating physiochemical properties. Interactions of the solvent exposed region with the PD-L1 protein are mediated through bound water molecules (to $_{A}$Asp122, $_{A}$Thr20, $_{A}$Tyr123, and $_{B}$Gln66), though direct interaction with Lys124 plays a part.

Aryl Linker Region

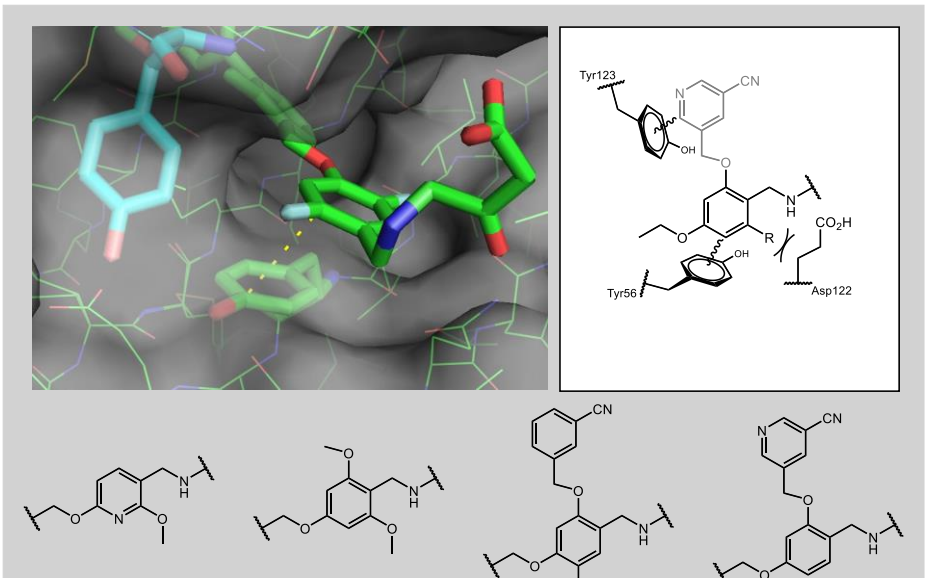

Figure 2.17 Key binding elements in the aryl linker region of PD-L1 dimer

The aryl linker portion of PD-L1 inhibitors connect the solvent exposed region to the biaryl headgroup. While the primary function of this region is positioning the

binding portions of the molecule in space, there are several interactions that it makes that are of note (Figure 2.17). Early compounds disclosed include small greasy functionalities on this ring, including chlorine and methoxy groups. These groups form hydrophobic contacts with the side chain of $_{A}$Asp122, but more importantly, the ring itself forms a pi stacking interaction with Tyr56 of the B subunit in the dimer, helping to encourage dimerization. Further SAR disclosed in later patents include 5-cyanopyridn-3-yl methoxy groups to strengthen the interaction with $_{B}$Tyr56.

Biaryl Headgroup

The most crucial binding element of the pharmacophore is the 2-susbtituted-1,1'-biphenyl moiety (Figure 2.18). This highly hydrophobic portion of the molecule has been demonstrated to be the minimum active fragment in PD-L1 inhibition and anchors the remainder of the molecule into the binding pocket. The major interactions driving this binding activity are T-stacking with ATyr56, and pi-alkyl interactions to Met115 and Ala121. Importantly, the 2-substitution on the biphenyl cants the distal ring at 45 degree angle, which pushes the substituting group in closer contact with Met115 and improves the contact.

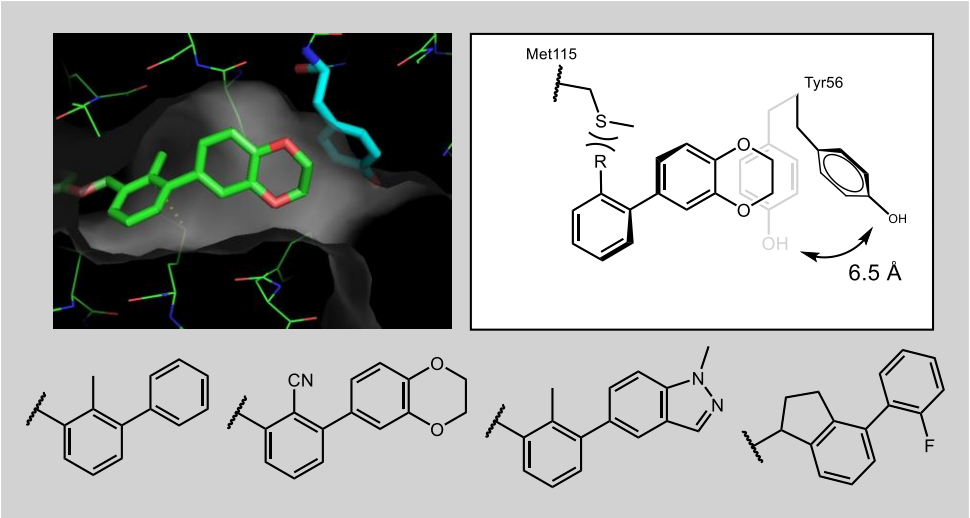

Figure 2.18 Key binding elements in the biaryl tunnel region of PD-L1 dimer

Moving from a biphenyl compound to the benzodioxane derivatives causes more profound structural changes to the PD-L1 dimer. The steric repulsion of the larger functionality causes

aTyr56 to swing back (6.5 angstrom movement) and creates a hydrophobic tunnel that encapsulates the bound ligand. The benxodioxane ethers form hydrogen bonds to AAla121. This restructuring can be seen in the higher binding affinities of benzodioxane-containing compounds.

2.8 Design of PD-L1 Radiotracers

2.8.1 Properties of a PET tracer

The properties most important in designing a radioligand are similar yet distinct to those important to drug design. Since the radiotracer is often dosed far below therapeutic levels, properties like toxicity are less critical. However, to maximize the signal to noise, dissociation constants (Kd) must be low nanomolar concentration. The compounds must not be overly hydrophilic (preventing compartmentalization in the kidney and bladder) or hydrophobic (nonspecific binding to plasma proteins). Depending on the rate of metabolism of the compounds, preventing radiolabeled metabolites may be important. Ideally, incorporation of the radionuclide will not decrease the binding affinity and be relatively isosteric to the parent inhibitor; therefore, it is common to see methoxy groups used as ^{11}C incorporation sites or ^{18}F replacing an alcohol (Figure 2.19).

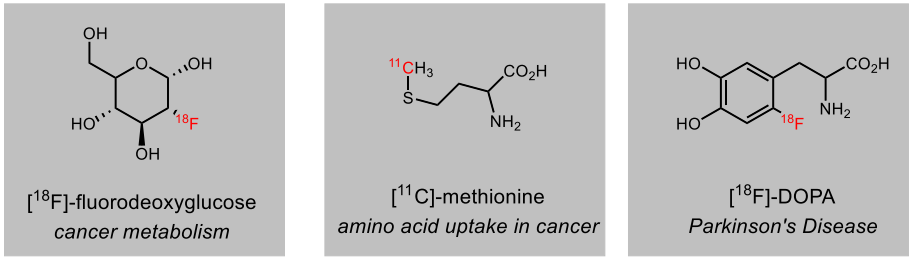

Figure 2.19 Commonly used PET tracers showing site of radionuclide incorporation

Finally, the compound's synthesis must be amenable to incorporation of the radionuclide in the last synthetic step; half lives are on the order of minutes and the compound must be synthesized, purified, and characterized within 1-2 half-lives (~3.5 hours for ^{18}F). Furthermore, fluoride is a poor nucleophile and an excellent base; elimination of the intended leaving group is a common

problem. These constraints require strategic synthetic planning, the ligand's structure must be fully elaborated before the introduction of a potent electrophile.

2.8.2 First generation design of PD-L1 PET tracer

After examining the plethora of compounds disclosed in patents issued to Bristol-Meyers Squibb, one compound appeared particularly attractive as the parent compound contained a fluorine atom. Retrosynthetically, the fluorine could be incorporated by S_NAr of a nitro leaving group with the ortho cyano function activating it for displacement. Utilizing a nitro leaving group (compared to a more traditional fluorine leaving group) prevents a competing reverse reaction of $[^{19}F]F^-$ displacing ^{18}F.

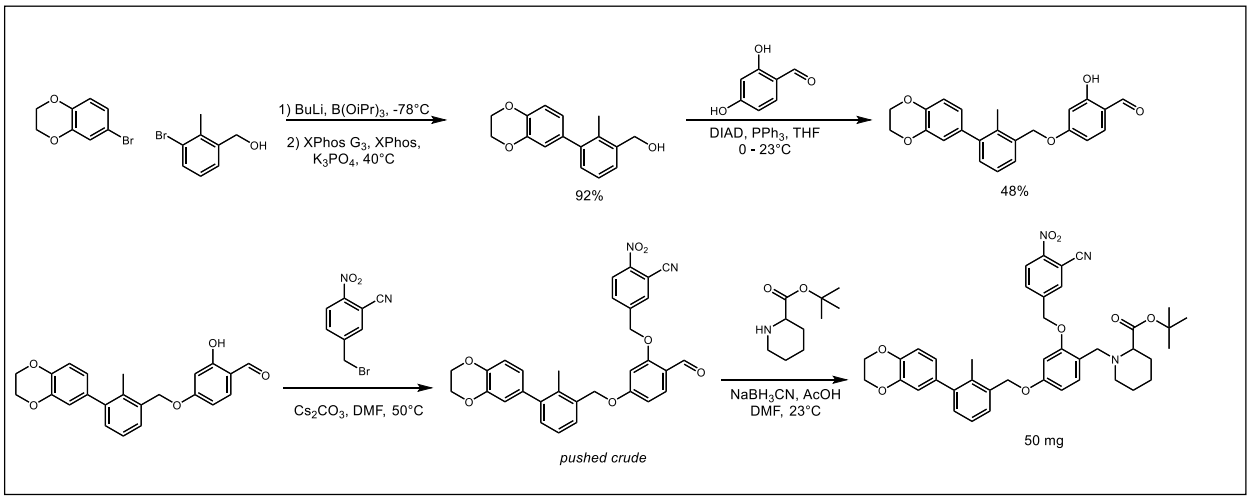

Scheme 2. Synthesis of precursor for first generation PD-L1 PET tracer

Shown in Scheme 2, synthesis of this compound began with bromination of benzodioxane, followed by Suzuki coupling to construct the biaryl core. Next, Mitsunobu alkylation of the linking arene furnished the nascent backbone. Alkylation of the pi-stacking arene containing the electrophilic warhead followed by reductive amination of the solubilizing group completed the synthesis.

The yields of the Mitsunobu alkylation were modest and highly variable utilizing the rection conditions from the literature. However, after screening a series of conditions with little improvement, it was found that purification of the electron rich benzaldehyde fragment just prior to use provided an improvement in yield and purification.

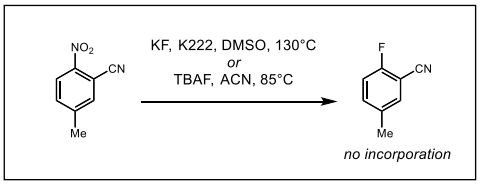

Scheme 3 Fluorination using model system

Initial attempts to fluorinate the derivative were largely unsuccessful, likely owing to its high reactivity and propensity to degrade. Indeed, even the benzyl bromide fragment was unprecedented in the literature and would degrade rapidly upon standing. Utilizing a simplified electrophile as a model system, extremely low levels of fluorination were observed (Scheme 3).

2.8.3 Second generation design of PD-L1 PET tracer

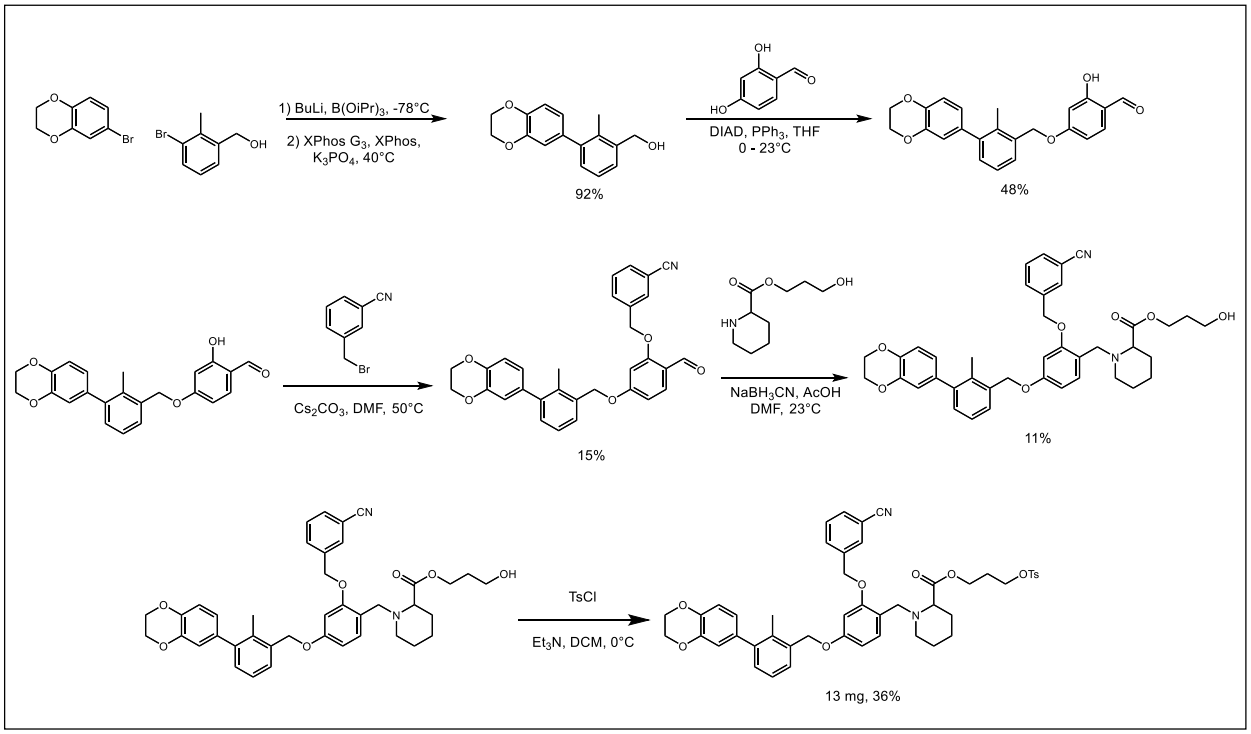

Scheme 4. Synthesis of precursor for second generation PD-L1 PET tracer

Incorporation of fluorine by displacement of alkyl sulfonates is extremely well precendented and we sought to improve the reliability of our fluorine incorporation by utilizing

this strategy. Following a similar synthesis (Scheme 4), the aryl linker core was alkylated with 3-cyanobenzyl bromide and then reductive amination with pipecolic acid completed the synthesis of a known low nanomolar PD-L1 small molecule. Esterification with propane diol and tosylation furnished the fully elaborated radiotracer precursor. Fluorination of this compound proceeded smoothly with TBAF as well as KF/$K_{2,2,2}$. The fluorination was successfully transferred to the radiochemistry facility and cell uptake of the compound was attempted. However, this compound is extremely hydrophobic and was insoluble in the aqueous buffer used to prepare the cells.

2.8.4 Third generation of PD-L1 PET tracer

Further examination of the patent literature yielded a more promising compound series. Published by Incyte, these compounds were >100,000x more soluble in water; not only would this allow for analysis, but we hypothesized we would observe significantly better signal to noise. As the biaryl region was highly conserved across all the disclosed compounds, we sought to incorporate fluorine in a location that would minimally effect binding. In contrast, the solvent exposed region contained a range of functionality with no loss in binding. This was a logical place to introduce the radionuclide. Analogous to an alkyl sulfonate, we designed a labeling precursor containing a cyclic sulfamidate. This functionality is known to be highly electrophilic and is easily

constructed from 2-aminoethanol derivatives.

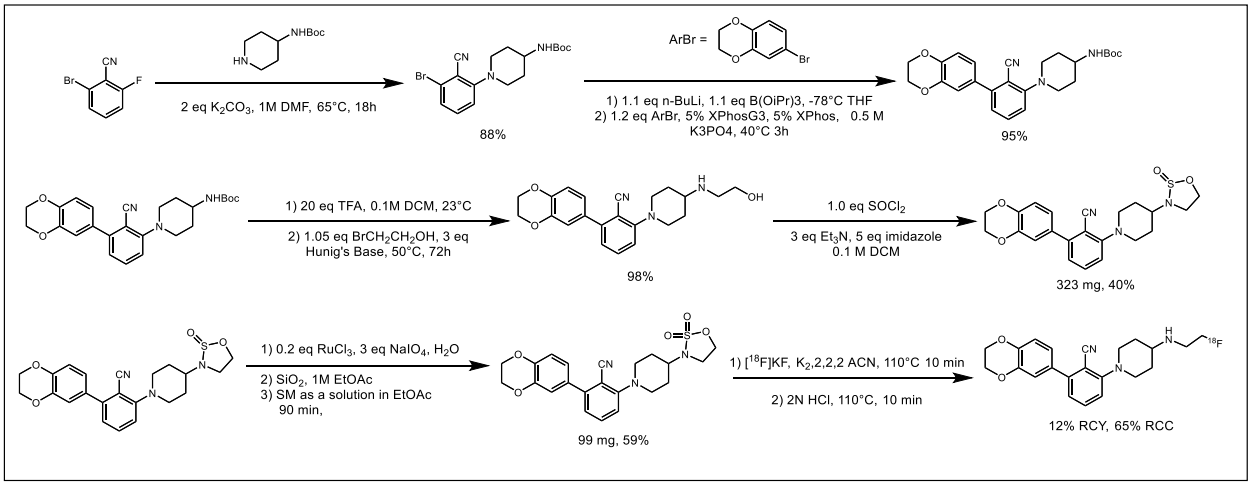

Scheme 5. Synthesis of precursor and successful radiolabeling of third generation PD-L1 PET tracer

The synthesis of the sulfamidate precursor began with one-pot borylation/Suzuki coupling of benzodioxane bromide with 2-bromo-6-fluoro-benzonitrile (Scheme 5). Next, SNAr displacement of fluoride with 4-tertbutoxyamino-piperidine provided the fully elaborated backbone. Facile amine deprotection followed by alkylation furnished the 2-aminoethanol derivative. Cyclization of this compound with thionyl chloride followed by oxidation of the sulfur center yielded the sulfamidate electrophile. Encouragingly, the final compound is so electrophilic that it significantly degrades during aqueous workup and silica purification. With the desired precursor in hand, we tested the fluorination. At 85C in acetonitrile with 10 equivalents of KF, no fluorination was observed over 60 mintues; however, after addition of cryptand ligand $K_{2,2,2}$ the reaction proceeded quantitatively within 5 minutes. Fluorination of this compound with [^{18}F]KF performed similarly well, with a radiochemical conversion of 64% and radiochemical yield of 12%.

2.9 *In vitro* characterization of a small molecule PD-L1 PET tracer

Following the successful development of radiofluorination conditions for this radiotracer, we sought to determine if any of the modifications to the compound's structure precluded high affinity binding. Utilizing surface plasmon resonance, we determined that the fluorinated compound has a binding affinity comparable to other PD-L1 inhibitors (50 nM, Figure 2.20). This is encouraging as removal of a hydrogen bonding moiety such as an alcohol in the solvent exposed portion of the molecule is likely to disrupt the hydrogen bonding network at the mouth of the pocket. This level of affinity was encouraging for futher development of the compound. Next, we examined the radiouptake in cells dosed with the ^{18}F ligand (Figure 2.21). This allows for relatively easy determination of the specificity of binding from the compound, as a model of signal to noise that would be observed in an *in vivo* system. A dose of the ^{18}F tracer was synthesized, and then added to tumor cells. The cells were then

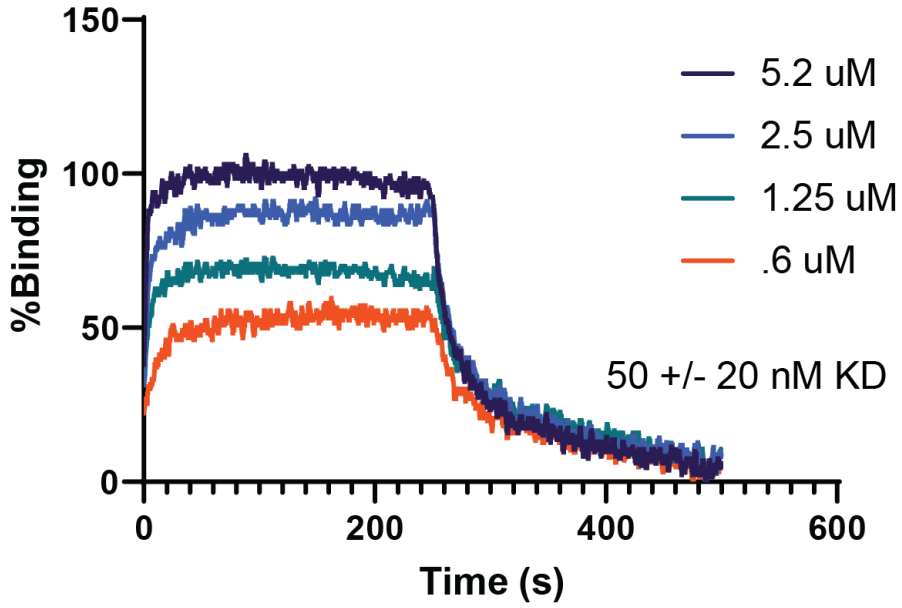

Figure 2.20 Surface plasmon resonance measurement of the radiotracer binding affinity for PD-L1

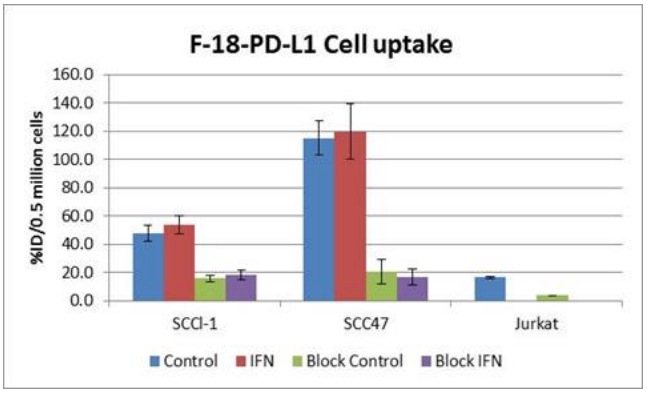

Figure 2.21 Cell uptake study demonstrating specific and competitive binding of the radioligand to PD-L1

washed, and radioactivity measured. The measured radioactivity in the PD-L1 positive cell lines (SCCl-1 and SCC47), was much higher than in PD-L1 negative cell line (Jurkat T cells), indicating the radiotracer binds specifically to PD-L1. Next, the cells were pretreated with the ^{19}F version of the radiotracer and then dosed with ^{18}F compound, and the observed radioactivity was significantly diminished, further corroborating that the compound binds specifically and competitively with the cold compound. Interferon gamma, a chemokine that is responsible for maintaining high levels of PD-L1 expression in tumor cells, appeared to have little effect. In particular, the blocking study with the ^{19}F compound as well as interferon gamma, we still observed similar levels of blocking, indicating saturation of the receptors.

2.10 *In vivo* characterization of a small molecule PD-L1 PET tracer

Encouraged by the *in vitro* studies, we next sought to determine if the tracer would be effective in determination of PD-L1 expressing tumors in rodents. To do this, we first cultured SCC47 and MCF-7 cells and implanted them into the flanks of mice. The tumors were then allowed to grow over three weeks until they were 180-360 mm^3, at which point the mice were dosed with the radioligand and imaged by microPET/CT. The results of these studies are currently being collected and analyzed.

2.11 Conclusion

PD-(L)1 therapeutics have revolutionized the way that cancer is treated. No longer are treatments doled out based on the location of the tumor, but by its genetic makeup. These therapeutics can provide significant improvement in progression free survival while also mitigating side effects. However, there remains uncertainty about which patients may respond well to the therapies, as it

is currently very difficult to accurately determine PD-L1 expression. Immunohistochemical assays are moderately effective, but when there are lives on the line, moderately effective is not enough. Positron emission tomography has been used for decades as a diagnostic tool in the field of oncology, and recently mutation and disease specific tracers have been developed to diagnose tumor mutational burden on a more granular level. Here we disclose the development of a ^{18}F small molecule PET tracer that is soluble, highly potent, and specific to PD-L1. This molecule represents an improvement on antibody, nanobody, small peptide, and existing small molecule PET tracers for PD-L1.

2.12 Supporting Information

2.12.1 General Information

All reactions were carried out in oven-dried glassware, equipped with a stir bar and under a nitrogen atmosphere with dry solvents under anhydrous conditions, unless otherwise noted. Solvents used in anhydrous reactions were purified by passing over activated alumina and storing under argon. Yields refer to chromatographically and spectroscopically (1H NMR) homogenous materials, unless otherwise stated. Reagents were purchased at the highest commercial quality and used without further purification, unless otherwise stated. n-Butyllithium (n-BuLi) was used as a 1.6 M or a 2.5 M solution in hexanes (Aldrich), was stored at 4°C and titrated prior to use. Organic solutions were concentrated under reduced pressure on a rotary evaporator using a water bath. Chromatographic purification of products was accomplished using forced-flow chromatography on 230-400 mesh silica gel. Preparative thin-layer chromatography (PTLC) separations were carried out on 1000μm SiliCycle silica gel F-254 plates. Thin-layer chromatography (TLC) was performed on 250μm SiliCycle silica gel F-254 plates. Visualization

of the developed chromatogram was performed by fluorescence quenching or by staining using KMnO4, p-anisaldehyde, or ninhydrin stains.

1H and 13C NMR spectra were obtained from the Emory University NMR facility and recorded on a Bruker Avance III HD 600 equipped with cryo-probe (600 MHz), INOVA 600 (600 MHz), INOVA 500 (500 MHz), INOVA 400 (400 MHz), VNMR 400 (400 MHz), or Mercury 300 (300 MHz), and are internally referenced to residual protio solvent signals. Data for 1H NMR are reported as follows: chemical shift (ppm), multiplicity (s = singlet, d = doublet, t = triplet, q = quartet, m = multiplet, dd = doublet of doublets, dt = doublet of triplets, ddd= doublet of doublet of doublets, dtd= doublet of triplet of doublets, b = broad, etc.), coupling constant (Hz), integration, and assignment, when applicable. Data for decoupled 13C NMR are reported in terms of chemical shift and multiplicity when applicable. Gas Chromatography Mass Spectrometry (GC-MS) was performed on an Agilent 5977A mass spectrometer with an Agilent 7890A gas chromatography inlet. Liquid Chromatography Mass Spectrometry (LC-MS) was performed on an Agilent 6120 mass spectrometer with an Agilent 1220 Infinity liquid chromatography inlet. Preparative High-Pressure Liquid chromatography (Prep-HPLC) was performed on an Agilent 1200 Infinity Series chromatograph using an Agilent Prep-C18 30 x 250 mm 10 μm column, or an Agilent Prep-C18 21.2 x 100 mm, 5 μm column.

2.12.2 Evaluation of Purity

Purity of all tested compounds was determined by HPLC analysis, using the methods given below (as indicated for each compound).

Method A: A linear gradient using water and 0.1 % formic acid (FA) (Solvent A) and MeCN and 0.1% FA (Solvent B); t = 0 min, 30% B, t = 4 min, 99% B (held for 1 min), then 50% B for 1 min, was employed on an Agilent Poroshell 120 EC-C18 2.7 micron, 3.0 mm x 50 mm column

(flow rate 1 mL/min) or an Agilent Zorbax SB-C18 1.8 micron, 2.1 mm x 50 mm column (flow rate 0.8 mL/min). The UV detection was set to 254 nm. The LC column was maintained at ambient temperature.

Method B: A linear gradient using water and 0.1 % formic acid (FA) (Solvent A) and MeCN and 0.1% FA (Solvent B); t = 0 min, 70% B, t = 4 min, 99% B (held for 1 min), then 50% B for 1 min, was employed on an Agilent Poroshell 120 EC-C18 2.7 micron, 3.0 mm x 50 mm column (flow rate 1 mL/min) or an Agilent Zorbax SB-C18 1.8 micron, 2.1 mm x 50 mm column (flow rate 0.8 mL/min). The UV detection was set to 254 nm. The LC column was maintained at ambient temperature.

Method C: A linear gradient using water and 0.1 % formic acid (FA) (Solvent A) and MeCN and 0.1% FA (Solvent B); t = 0 min, 5% B, t = 6 min, 95% B (held for 2 min), then 5% B for 1 min, was employed on an Agilent Poroshell 120 EC-C18 2.7 micron, 3.0 mm x 50 mm column (flow rate 1 mL/min) or an Agilent Zorbax SB-C18 1.8 micron, 2.1 mm x 50 mm column (flow rate 0.8 mL/min). The UV detection was set to 254 nm. The LC column was maintained at ambient temperature.

2.12.3 Chemical Synthesis

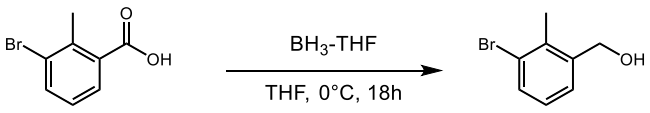

(3-bromo-2-methylphenyl)methanol 3-bromo-2-methylbenzoic acid (10g) was dissolved in 100 mL THF. Cooled to 0 Celsius and then 17.5 mL borane was added dropwise. Stirred overnight as it warmed to room temperature. Quenched cautiously with 0.5 N HCl and then extracted with diethyl ether. Concentrated to a crude solid that was passed through a silica plug with 40% ethyl

acetate in hexanes. Concentrated to white plates. 9.3 g, 99%. ^{1}H NMR (600 MHz, Chloroform-*d*) δ 7.49 (d, *J* = 8.0 Hz, 1H), 7.30 (d, *J* = 7.5 Hz, 1H), 7.04 (t, *J* = 7.8 Hz, 1H), 4.69 (s, 2H), 2.40 (s, 3H).

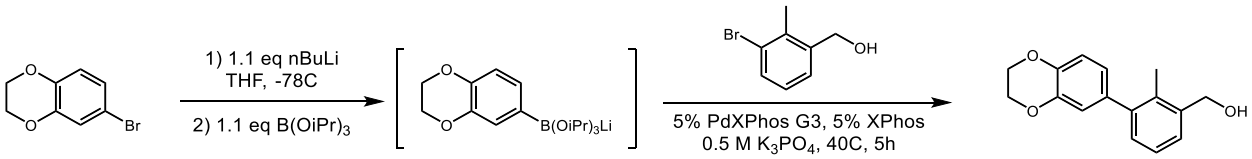

(3-(2,3-dihydrobenzo[b][1,4]dioxin-6-yl)-2-methylphenyl)methanol An oven dried round bottom flask was charged with 3.98 g benzodioxane bromide and 25 mL THF. The flask was sealed and cooled to -78 Celsius. Next, 8.25 mL (1.1 eq) butyllithium (2.5 M in hexanes) was added dropwise, followed immediately by 4.75 mL of triisopropyl borate. The reaction was stirred at the same temperature for 60 minutes, then 50 mL of 0.5 M potassium phosphate was added. The reaction was then uncapped, and 2.5 g of (3-bromo-2-methylphenyl)methanol was added along with 75 mg of PdXPhos G3 and 42 mg of Xphos. The flask was resealed and then evacuated and refilled with nitrogen. The reaction was placed in a preheated oil bath at 40 degrees Celsius and stirred for 5 hours. The reaction was then cooled to room temperature and saturate ammonium chloride solution was added. The reaction was extracted with ethyl acetate (3x 50 mL) and then concentrated. The crude residue was purified by silica chromatography (gradient 20-40% ethyl acetate in hexanes). 3.7 g, 83%. ^{1}H NMR (600 MHz, Chloroform-d) δ 7.36 (t, J = 7.6 Hz, 1H), 7.21 (t, J = 7.5 Hz, 1H), 7.18 – 7.14 (m, 1H), 6.90 (dd, J = 8.3, 1.9 Hz, 1H), 6.82 (dd, J = 9.2, 2.1 Hz, 1H), 6.76 (td, J = 8.7, 2.1 Hz, 1H), 4.88 (d, J = 179.2 Hz, 2H), 4.28 (s, 4H), 2.23 (d, J = 18.8 Hz, 3H).

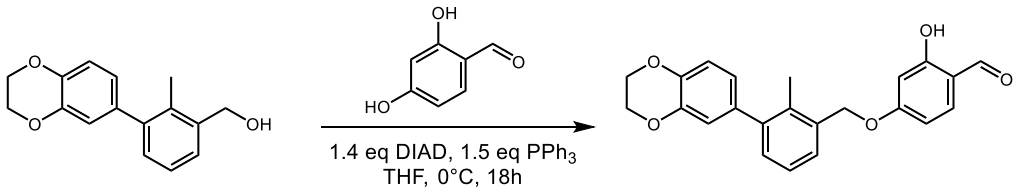

4-((3-(2,3-dihydrobenzo[b][1,4]dioxin-6-yl)-2-methylbenzyl)oxy)-2-hydroxybenzaldehyde

2.195 g 2,4-dihydroxybenzaldehyde, 4.162 g triphenylphosphine and 3.7 g (3-(2,3-dihydrobenzo[b][1,4]dioxin-6-yl)-2-methylphenyl)methanol was added to 61 mL THF. The solution was stirred until dissolved and then cooled to zero Celsius. Next, a solution of 3.01 mL Diisopropyl azodicarboxylate was added as a solution in 61 mL THF dropwise over 4h via syringe pump. The reaction was stirred overnight and allowed to warm to room temperature. Concentrated to a crude solid and then purified by silica chromatography (10-30% ethyl acetate in hexanes). 816 mg, 32%. ^{1}H NMR (600 MHz, Chloroform-*d*) δ 11.49 (s, 1H), 9.72 (s, 1H), 7.45 (d, *J* = 8.6 Hz, 1H), 7.36 (dd, *J* = 5.6, 3.5 Hz, 1H), 7.24 – 7.22 (m, 2H), 6.90 (d, *J* = 8.2 Hz, 1H), 6.81 (d, *J* = 2.1 Hz, 1H), 6.76 (dd, *J* = 8.3, 2.1 Hz, 1H), 6.63 (dd, *J* = 8.6, 2.4 Hz, 1H), 6.55 (d, *J* = 2.3 Hz, 1H), 5.12 (s, 2H), 4.30 (s, 4H), 2.24 (s, 4H).

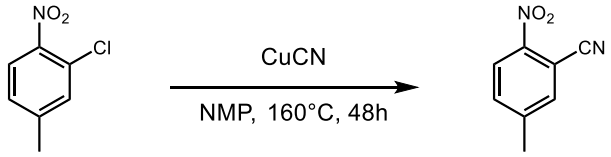

5-methyl-2-nitrobenzonitrile 3-chloro-4-nitro-toluene (5 g) and copper cyanide (7.2 g) were dissolved in NMP (25 mL) and then heated to 160C for 48. The reaction was cooled, then poured into cold chloroform. The solids were filtered off and the filtrate treated with activated charcoal, then filtered to remove the charcoal. The filtrate was washed with water, then dried with sodium sulfate and concentrated to a black tar. The residue was triturated with water (intense stirring) and then extracted into chloroform and dried with sodium sulfate and concentrated. The crude product was purified by silica chromatography (20% ethyl acetate in hexanes) to provide a yellow solid.

1.773 g, 50% ^{1}H NMR (600 MHz, Chloroform-*d*) δ 8.24 (d, *J* = 8.5 Hz, 1H), 7.70 (d, *J* = 1.9 Hz, 1H), 7.59 (ddt, *J* = 8.5, 1.5, 0.7 Hz, 1H), 2.53 (d, *J* = 0.7 Hz, 3H).

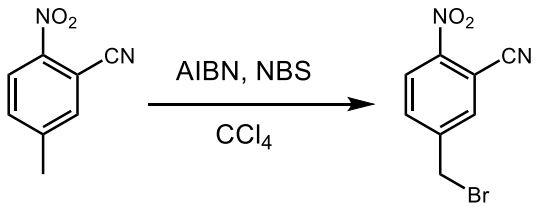

5-(bromomethyl)-2-nitrobenzonitrile A suspension of 5-methyl-2-nitrobenzonitrile (712 mg), freshly recrystallized N-Bromosuccinimide (866 mg, 1.1 eq) and freshly recrystallized azobisisobutyronitrile (72.6 mg, 0.1 eq) was heated to reflux for 48 hours. After cooling to room temperature, the suspension was filtered, and the filtrate evaporated to dryness. The resulting crude material was purified by silica chromatography to provide the title compound as a yellow oil. Extremely unstable upon standing, keep refrigerated. 142 mg, 11%. ^{1}H NMR (600 MHz, Chloroform-d) δ 8.32 (dd, J = 8.6, 1.5 Hz, 1H), 7.93 (d, J = 1.9 Hz, 1H), 7.82 (dd, J = 8.6, 2.0 Hz, 1H), 4.52 (d, J = 1.4 Hz, 2H).

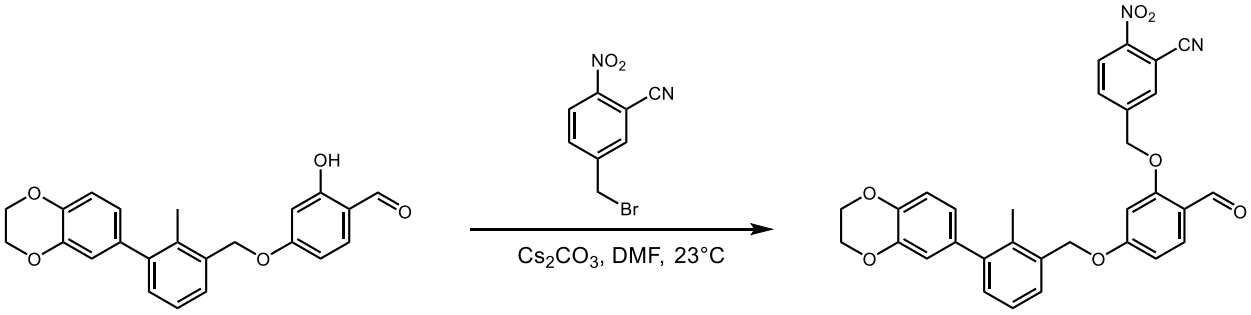

5-((5-((3-(2,3-dihydrobenzo[b][1,4]dioxin-6-yl)-2-methylbenzyl)oxy)-2-formylphenoxy)methyl)-2-nitrobenzonitrile was dissolved in 10 mL DMF. To this was added 250 mg of tert-butyl piperidine-2-carboxylate 282 mg (0.75 mmol) of 4-((3-(2,3-dihydrobenzo[b][1,4]dioxin-6-yl)-2-methylbenzyl)oxy)-2-hydroxybenzaldehyde, 390 mg (1.2

mmol, 1.6 equivalents) of cesium carbonate, and 4-nitro-3-cyanobenzyl bromide (241 mg, 1.0 mmol, 1.33 equivalents) were dissolved in 8 mL of DMF and the reaction stirred for 45 minutes at room temperature. Reaction was then quenched with 1M LiCl and extracted with ethyl acetate (3x 25 mL). The organic layers were combined, dried over sodium sulfate and concentrated to a crude residue that was passed through a silica plug and used without further purification.

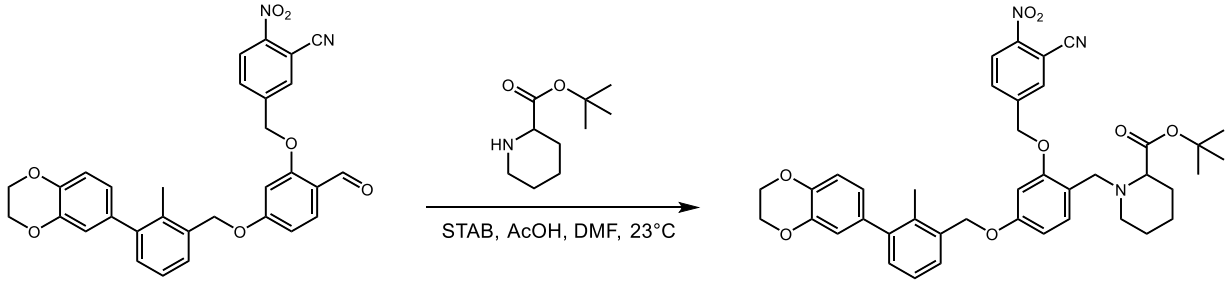

tert-butyl 1-(2-((3-cyano-4-nitrobenzyl)oxy)-4-((3-(2,3-dihydrobenzo[b][1,4]dioxin-6-yl)-2-methylbenzyl)oxy)benzyl)piperidine-2-carboxylate 100 mg of 5-((5-((3-(2,3-dihydrobenzo[b][1,4]dioxin-6-yl)-2-methylbenzyl)oxy)-2-formylphenoxy)methyl)-2-nitrobenzonitrile was dissolved in 10 mL DMF. To this was added 250 mg of tert-butyl piperidine-2-carboxylate. The mixture was stirred for 20 minutes then 50 microliters of acetic acid was added followed by 15 mg of sodium cyanoborohydride. Reaction was stirred overnight, one drop of water was added to quench residual borohydride and then the reaction was filtered. The reaction mixture was purified by preparative HPLC 10-99 % ACN in water, 0.1% formic acid modifier. 15 mg (11.4%). ^{1}H NMR (600 MHz, Chloroform-*d*) δ 7.73 (dd, *J* = 6.0, 2.2 Hz, 1H), 7.68 (ddd, *J* = 7.8, 5.0, 2.2 Hz, 1H), 7.35 (t, *J* = 6.8 Hz, 2H), 7.23 – 7.19 (m, 3H), 6.89 (d, *J* = 8.3 Hz, 1H), 6.81 (d, *J* = 2.1 Hz, 1H), 6.76 (dd, *J* = 8.2, 2.2 Hz, 1H), 6.62 (dd, *J* = 8.3, 2.3 Hz, 1H), 6.50 (d, *J* = 2.3 Hz, 1H), 5.02 (d, *J* = 7.5 Hz, 4H), 4.29 (s, 4H), 3.63 (dd, *J* = 136.1, 13.6 Hz, 2H), 3.47 (s, 2H), 3.08 (t, *J* = 5.8 Hz, 1H), 2.95 (ddd, *J* = 11.0, 6.9, 3.6 Hz, 1H), 2.24 (s, 3H), 2.18 (ddd, *J* = 11.4, 7.8, 3.8

Hz, 1H), 1.79 (q, *J* = 6.0 Hz, 2H), 1.70 – 1.48 (m, 1H), 1.45 (s, 9H), 1.37 (dt, *J* = 15.5, 7.9 Hz, 1H).

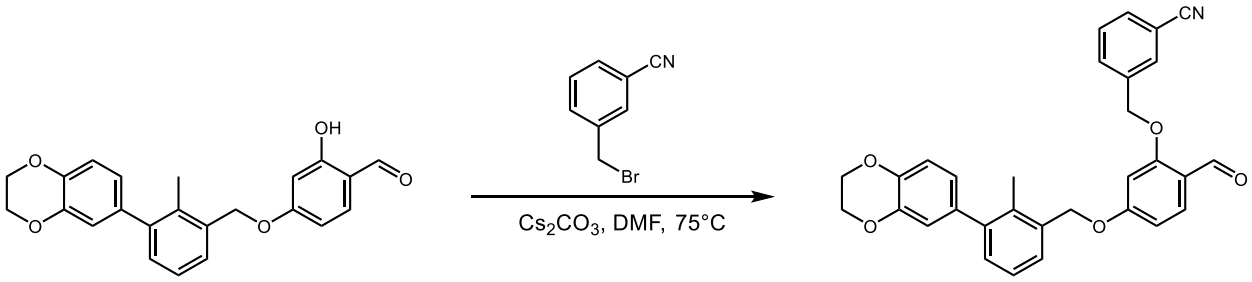

3-((5-((3-(2,3-dihydrobenzo[b][1,4]dioxin-6-yl)-2-methylbenzyl)oxy)-2-formylphenoxy)methyl)benzonitrile 264 mg of 4-((3-(2,3-dihydrobenzo[b][1,4]dioxin-6-yl)-2-methylbenzyl)oxy)-2-hydroxybenzaldehyde (0.7 mmol) was charged to a round bottom flask followed by 342 mg of cesium carbonate (1.5 equivalents) and 158 mg (0.805 mmol) 3-cyanobenzyl bromide. 10 mL of DMF was added and the reaction stirred for 3 hours at 75°C. The reaction was then cooled, and neutralized with 0.1M HCl. Extracted with ethyl acetate (3x 25 mL) then the organic layers dried over sodium sulfate and concentrated to a crude residue that was purified by silica chromatography (10-65% ethyl acetate in hexanes). 150 mg, 44%. ^{1}H NMR (600 MHz, Chloroform-d) δ 10.36 (s, 1H), 7.88 (d, J = 8.7 Hz, 1H), 7.72 (s, 1H), 7.69 (d, J = 8.0 Hz, 1H), 7.64 (d, J = 7.6 Hz, 1H), 7.52 (t, J = 7.8 Hz, 1H), 7.35 (t, J = 4.5 Hz, 1H), 6.90 (d, J = 8.2 Hz, 1H), 6.81 (d, J = 2.0 Hz, 1H), 6.76 (dd, J = 8.2, 2.1 Hz, 1H), 6.72 (d, J = 7.9 Hz, 1H), 6.56 (d, J = 2.1 Hz, 1H), 5.16 (s, 2H), 5.12 (s, 2H), 4.30 (s, 4H), 2.25 (s, 3H).

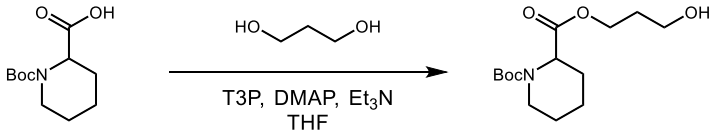

1-(tert-butyl) 2-(3-hydroxypropyl) piperidine-1,2-dicarboxylate 10 mmol 1-(tert-butoxycarbonyl)piperidine-2-carboxylic acid (2.29 g), 15 mmol 1,3 propane diol (114 mg, 1.5 eq), 1 mmol 4-dimethylaminopyridine (0.1 eq, 12 mg) and 20 mmol triethylamine (2 g, 1.3 mL, 2 eq) were dissolved in 100 mL THF and cooled to 0°C. To this was added 12 mmol of tripropylphosphonic anhydride (T3P, 60% solution in ethyl acetate, 5.94 mL) and stirred for 60 minutes. The reaction was warmed to room temperature and poured into 1M NaOH, extracted with ethyl acetate (3x 50 mL) and concentrated to a colorless oil. The crude oil was purified by silica chromatography (40% ethyl acetate in hexanes) to provide 2.33 g (81%) of the title compound. Mixture of rotamers. ^{1}H NMR (600 MHz, Chloroform-*d*) δ 4.24 (dt, *J* = 22.2, 6.5 Hz, 2H), 4.04 – 3.79 (m, 1H), 3.64 (t, *J* = 6.0 Hz, 2H), 2.99 – 2.73 (m, 1H), 2.17 (q, *J* = 18.2, 14.5 Hz, 2H), 1.83 (p, *J* = 5.9 Hz, 2H), 1.69 – 1.52 (m, 3H), 1.40 (d, *J* = 18.8 Hz, 8H), 1.18 (ddd, *J* = 14.3, 10.7, 3.6 Hz, 1H).

3-hydroxypropyl piperidine-2-carboxylate 2.32 g of 1-(tert-butyl) 2-(3-hydroxypropyl) piperidine-1,2-dicarboxylate (8.1 mmol) was dissolved in 81 mL of dichloromethane and cooled to 0°C. Next, 20 equivalents of trifluoroacetic acid (dissolved in 80 mL dichloromethane) was added dropwise over 20 minutes. The reaction was stirred at 0°C for 30 minutes then warmed to

room temperature and stirred for 90 minutes then quenched with saturated sodium bicarbonate solution. The organic layer was separated and then dried over sodium sulfate and concentrated to a colorless oil. 1.5g, 99%. ^{1}H NMR (600 MHz, Chloroform-*d*) δ 4.27 (t, *J* = 6.1 Hz, 2H), 3.65 (s, 1H), 3.40 (dd, *J* = 10.2, 3.2 Hz, 1H), 3.11 (dt, *J* = 13.0, 3.6 Hz, 1H), 2.70 – 2.64 (m, 1H), 1.97 (dp, *J* = 10.5, 2.9 Hz, 1H), 1.86 (p, *J* = 6.0 Hz, 2H), 1.77 (dt, *J* = 7.9, 5.4 Hz, 1H), 1.57 (dtd, *J* = 23.7, 10.5, 9.1, 6.0 Hz, 2H), 1.50 – 1.38 (m, 2H).

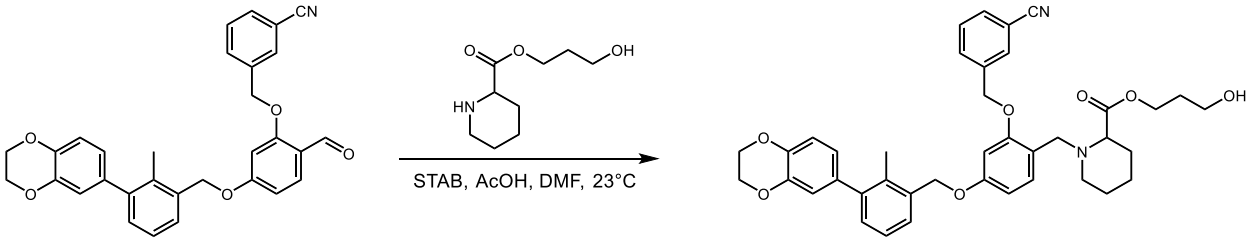

3-hydroxypropyl 1-(2-((3-cyanobenzyl)oxy)-4-((3-(2,3-dihydrobenzo[b][1,4]dioxin-6-yl)-2-methylbenzyl)oxy)benzyl)piperidine-2-carboxylate 100 mg of 3-((5-((3-(2,3-dihydrobenzo[b][1,4]dioxin-6-yl)-2-methylbenzyl)oxy)-2-formylphenoxy)methyl)benzonitrile (0.2 mmol) and 150 mg 3-hydroxypropyl piperidine-2-carboxylate (0.8 mmol, 4 eq) was dissolved in 6 mL DMF and stirred for 2h at room temperature. Next, 16 microliters of acetic acid (1 eq) was added along with 52.7 mg of sodium cyanoborohydride (0.6 mmol, 3 eq). Reaction stirred for 4 days at room temperature. 1M lithium chloride was added to quench the reaction and then it was extracted with ethyl acetate (3x 10 mL). The organics were dried over sodium sulfate and concentrated to a crude residue. Purified 30-80% ethyl acetate in hexanes. 74 mg, 55% ^{1}H NMR (600 MHz, Chloroform-*d*) δ 7.77 (d, *J* = 6.1 Hz, 1H), 7.66 (d, *J* = 7.7 Hz, 1H), 7.61 (d, *J* = 7.5 Hz, 1H), 7.50 (t, *J* = 7.7 Hz, 1H), 7.37 (dt, *J* = 8.8, 4.4 Hz, 1H), 7.31 (d, *J* = 8.3 Hz, 1H), 7.25 – 7.19 (m, 2H), 6.91 (d, *J* = 8.2 Hz, 1H), 6.84 – 6.80 (m, 1H), 6.77 (td, *J* = 7.1, 6.0, 1.9 Hz, 1H), 6.64 (dd, *J* = 8.3, 2.4 Hz, 1H), 6.54 (t, *J* = 3.5 Hz, 1H), 5.09 (d, *J* = 2.3 Hz, 2H), 5.04 (d, *J* = 6.0 Hz, 2H),

4.30 (d, *J* = 5.5 Hz, 4H), 4.27 (td, *J* = 6.3, 1.8 Hz, 1H), 3.78 (d, *J* = 13.8 Hz, 1H), 3.68 (t, *J* = 6.0 Hz, 1H), 3.61 (d, *J* = 13.1 Hz, 1H), 3.26 (s, 1H), 3.03 (s, 1H), 2.25 (d, *J* = 5.9 Hz, 3H), 1.92 – 1.77 (m, 3H), 1.67 – 1.52 (m, 3H), 1.40 (d, *J* = 7.3 Hz, 1H), 1.32 – 1.18 (m, 2H).

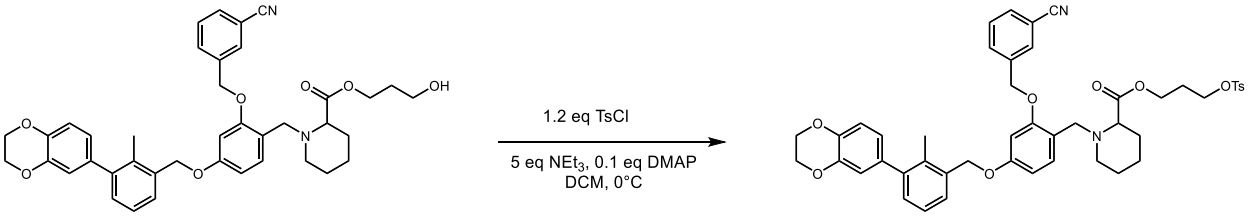

3-(tosyloxy)propyl 1-(2-((3-cyanobenzyl)oxy)-4-((3-(2,3-dihydrobenzo[b][1,4]dioxin-6-yl)-2-methylbenzyl)oxy)benzyl)piperidine-2-carboxylate 30 mg 3-hydroxypropyl 1-(2-((3-cyanobenzyl)oxy)-4-((3-(2,3-dihydrobenzo[b][1,4]dioxin-6-yl)-2-methylbenzyl)oxy)benzyl)piperidine-2-carboxylate stirred in 1 mL dichloromethane and cooled to 0°C. Next, 6 microliters of triethylamine (3 equivalents) and 8.55 mg tosyl chloride (1.5 equivalents). The reaction was stirred overnight. In the morning, water was added and the mixture extracted with dichloromethane (3x 5 mL) and the organic fractions combined, dried over sodium sulfate and concentrated to a crude oil. The oil was purified by silica chromatography (40% ethyl acetate in hexanes). 13 mg, 35% ^{1}H NMR (600 MHz, Chloroform-*d*) δ 7.79 – 7.71 (m, 2H), 7.65 (d, *J* = 7.8 Hz, 1H), 7.59 (d, *J* = 7.7 Hz, 1H), 7.50 – 7.43 (m, 1H), 7.36 (dd, *J* = 6.4, 2.6 Hz, 1H), 7.28 (dd, *J* = 16.6, 8.1 Hz, 2H), 7.23 – 7.19 (m, 2H), 6.89 (d, *J* = 8.2 Hz, 1H), 6.81 (d, *J* = 2.1 Hz, 1H), 6.76 (dd, *J* = 8.2, 2.1 Hz, 1H), 6.62 (dd, *J* = 8.3, 2.3 Hz, 1H), 6.51 (d, *J* = 2.4 Hz, 1H), 5.05 (s, 2H), 5.03 (s, 2H), 4.29 (s, 4H), 4.09 (dt, *J* = 21.1, 6.5 Hz, 4H), 3.72 – 3.50 (m, 2H), 3.16 (t, *J* = 5.9 Hz, 1H), 2.99 – 2.90 (m, 1H), 2.40 (s, 3H), 2.24 (s, 3H), 1.96 (p, *J* = 6.2 Hz, 2H), 1.73 (d, *J* = 10.7 Hz, 3H), 1.53 (h, *J* = 11.1, 8.4 Hz, 3H).

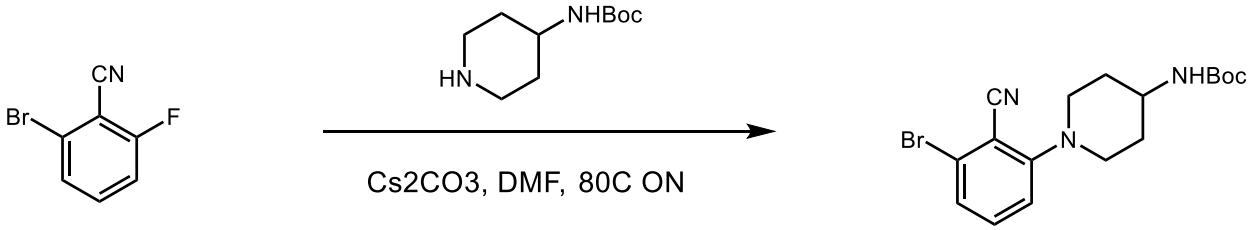

tert-butyl (1-(3-bromo-2-cyanophenyl)piperidin-4-yl)carbamate 2-fluoro-6-benzonitrile (3 mmol, 600 mg) was stirred in 5 mL DMF with boc-4-aminopiperidine (3.5 mmol, 700 mg, 1.17 equivalents) and cesium carbonate (6 mmol, 1.95 g, 2 equivalents). The reaction was heated to 80 degrees overnight and then cooled in the morning. Ethyl acetate (20 mL) was added and the solution extracted with lithium chloride (1M), saturated brine, and saturated ammonium chloride (20 mL each). The organic layer was dried with sodium sulfate and concentrated. Used without further purification. 1.085 g, 95% ^{1}H NMR (600 MHz, Chloroform-*d*) δ 7.31 (dd, *J* = 15.7, 7.6 Hz, 1H), 7.24 (d, *J* = 7.9 Hz, 1H), 6.97 (d, *J* = 8.3 Hz, 1H), 3.59 – 3.48 (m, 2H), 2.94 (td, *J* = 11.9, 2.5 Hz, 2H), 2.16 – 2.07 (m, 2H), 1.69 (qd, *J* = 11.3, 3.8 Hz, 2H), 1.48 (s, 9H). ^{13}C NMR (151 MHz, Chloroform-*d*) δ 158.30, 155.21, 133.89, 126.82, 125.65, 117.59, 116.71, 109.65, 79.51, 51.19, 47.44, 32.68, 28.42.

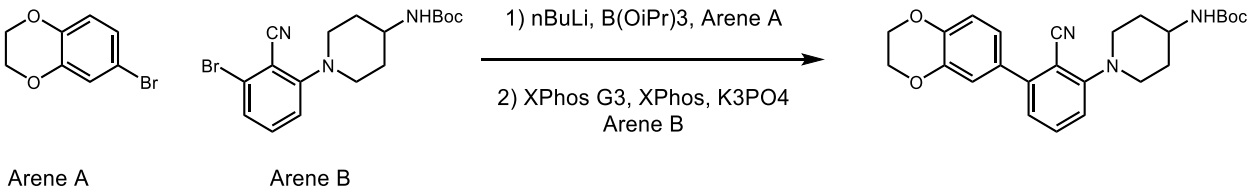

tert-butyl (1-(2-cyano-3-(2,3-dihydrobenzo[b][1,4]dioxin-6-yl)phenyl)piperidin-4-yl)carbamate In a 100 mL round bottom flask, 958 mg benzodioxane bromide (1.5 eq, 4.5 mmol)

was dissolved in 30 mL dry THF. The solution was cooled to -78 degrees and then 5.1 mmol n-butyl lithium was added (2.04 mL, 2.5M in hexanes) followed by 5.1 mmol triisopropyl borate (1.176 mL). The reaction was stirred for 60 minutes at -78 degrees, then uncapped and 20 mL of degassed potassium phosphate (0.5M) was added followed by 3.0 mmol of Arene B, 25 mg of PdXPhos G3, and 16 mg XPhos. The reaction was recapped, the headspace evacuated and refilled with argon and the reaction placed in a preheated 40 degree oil bath. Stirred for 3h and then quenched with saturated ammonium chloride and extracted with ethyl acetate. Concentrated to a crude solid that was purified by silica chromatography (40% EtOAc:Hexanes). 1.050 g, 85%

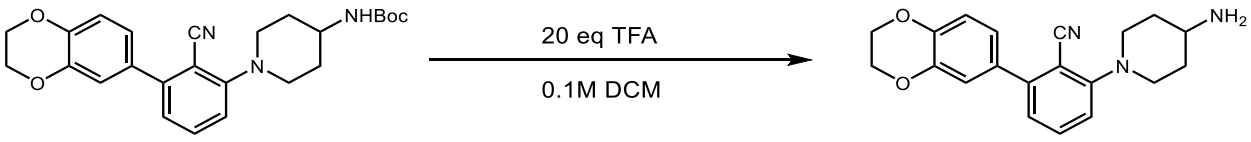

2-(4-aminopiperidin-1-yl)-6-(2,3-dihydrobenzo[b][1,4]dioxin-6-yl)benzonitrile Starting material was dissolved in DCM (10 mL) and 20 eqivalents of trifluoroacetic acid were added at room temperature. Stirred for 18h, then concentrated to provide the title compound. Used without further purification. ^{1}H NMR (600 MHz, Chloroform-*d*) δ 7.46 (t, *J* = 8.0 Hz, 1H), 7.08 – 6.93 (m, 5H), 4.37 – 4.27 (m, 4H), 3.60 (d, *J* = 12.0 Hz, 2H), 2.94 (q, *J* = 12.9, 11.6 Hz, 3H), 2.06 (d, *J* = 12.9 Hz, 2H), 1.74 (q, *J* = 11.6 Hz, 2H). ^{13}C NMR (151 MHz, Chloroform-*d*) δ 206.92, 157.53, 147.09, 144.09, 143.45, 133.02, 132.12, 122.90, 122.16, 117.90 (d, *J* = 4.8 Hz), 117.34 (d, *J* = 10.9 Hz), 105.73, 64.41 (d, *J* = 16.5 Hz), 51.29, 48.50, 35.06, 30.94. ^{13}C NMR (151 MHz, Chloroform-*d*) δ 158.30, 155.21, 133.89, 126.82, 125.65, 117.59, 116.71, 109.65, 51.19, 32.68, 28.42.

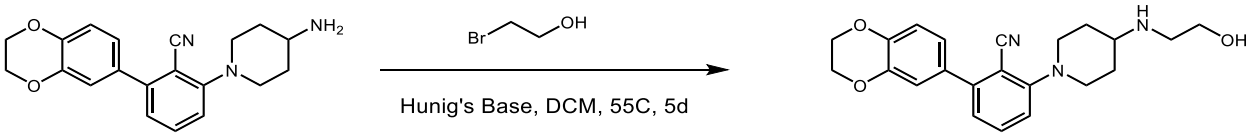

2-(2,3-dihydrobenzo[b][1,4]dioxin-6-yl)-6-(4-((2-hydroxyethyl)amino)piperidin-1-yl)benzonitrile In a pressure vessel, 653 mg of 2-(4-aminopiperidin-1-yl)-6-(2,3-dihydrobenzo[b][1,4]dioxin-6-yl)benzonitrile was dissolved in 7 mL of dichloromethane and then 326 microliters of diisopropylethyl amine and 130.6 microliters of 2-bromoethanol was added. The vessel was sealed with a Viton O-ring and stirred at 55 degrees for 5 days. The mixture was concentrated to a dark brown solid and then purified by silica chromatography (20% Methanol:DCM with 0.5% NH4OH). 739 mg, 98%

2-(2,3-dihydrobenzo[b][1,4]dioxin-6-yl)-6-(4-(2-oxido-1,2,3-oxathiazolidin-3-yl)piperidin-1-yl)benzonitrile 267 mg of 2-(2,3-dihydrobenzo[b][1,4]dioxin-6-yl)-6-(4-((2-hydroxyethyl)amino)piperidin-1-yl)benzonitrile was dissolved in 10 mL dichloromethane, then 272.4 microliters of triethylamine (197 mg, 3 eq) was added followed by 260 mg imidazole (5 eq). The solution was cooled to zero degrees.

Next, a solution of 78 mg thionyl chloride (47 microliters, 1.1 eq) in 5 mL dichloromethane was added dropwise over 20 minutes. The reaction was stirred until TLC indicated complete conversion. Water (10 mL) was added and the reaction extracted with dichloromethane (2x 10 mL) then 10% methanol in dichloromethane (20 mL). Organics were combined, dried, and concentrated to an orange solid. Purified by silica chromatography (0-10% methanol in dichloromethane). 204

mg, 68% ^{1}H NMR (500 MHz, Chloroform-*d*) δ 7.46 (t, *J* = 7.9 Hz, 1H), 7.07 – 6.88 (m, 5H), 4.82 (td, *J* = 7.6, 3.7 Hz, 1H), 4.36 (q, *J* = 8.0 Hz, 1H), 4.30 (s, 4H), 3.72 – 3.55 (m, 2H), 3.54 – 3.39 (m, 2H), 3.31 (tt, *J* = 10.6, 4.2 Hz, 1H), 2.95 (tt, *J* = 12.2, 3.3 Hz, 2H), 2.32 – 1.96 (m, 4H). ^{13}C NMR (151 MHz, Chloroform-*d*) δ 157.13, 156.79, 147.16, 144.15, 143.48, 133.08, 131.99, 123.32, 122.14, 117.88, 117.43, 117.27, 105.96, 71.28, 64.46, 64.36, 52.99, 51.25, 50.96, 43.76, 31.73, 31.62, 30.93.

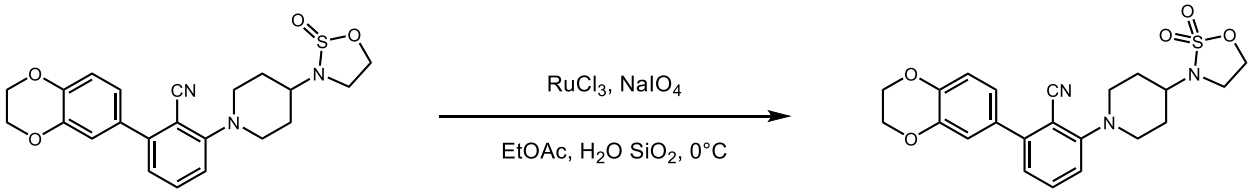

2-(2,3-dihydrobenzo[b][1,4]dioxin-6-yl)-6-(4-(2,2-dioxido-1,2,3-oxathiazolidin-3-yl)piperidin-1-yl)benzonitrile 1.35 mg ruthenium trichloride was dissolved in 165 microliters water, and then sodium periodate was added until the color changed from black to orange. Then, 0.39 g silica gel was added followed by the remaining sodium periodate (total addition 150 mg, 3 eq). 1.31 mL ethyl acetate was added and the reaction cooled to zero degrees. In a separate vial, 100 mg 2-(2,3-dihydrobenzo[b][1,4]dioxin-6-yl)-6-(4-(2-oxido-1,2,3-oxathiazolidin-3-yl)piperidin-1-yl)benzonitrile dissolved in 1.31 mL ethyl acetate, then added dropwise to the ruthenium solution. Stirred for 90 minutes and then the entire reaction was passed through celite, the celite pad washed with acetonitrile, and then the filtrate concentrated. Purified by silica chromatography (60% ethyl acetate in hexanes). 21 mg, 20% ^{1}H NMR (600 MHz, Chloroform-*d*) δ 7.47 (t, *J* = 7.9 Hz, 1H), 7.07 – 6.92 (m, 5H), 4.57 (t, *J* = 6.5 Hz, 2H), 4.35 – 4.26 (m, 4H), 3.63 (q, *J* = 5.6, 5.0 Hz, 4H), 3.52 (tt, *J* = 10.9, 3.9 Hz, 1H), 3.01 – 2.90 (m, 2H), 2.17 (dq, *J* = 7.7, 3.5 Hz, 2H), 1.31 (m, 2H). ^{13}C NMR (151 MHz, Chloroform-*d*) δ 157.13, 147.30, 144.32, 143.63,

133.29, 132.06, 123.67, 122.26, 118.01, 117.58, 117.51, 106.17, 66.82, 64.60, 64.50, 60.54, 54.19, 51.38, 43.95, 30.36.

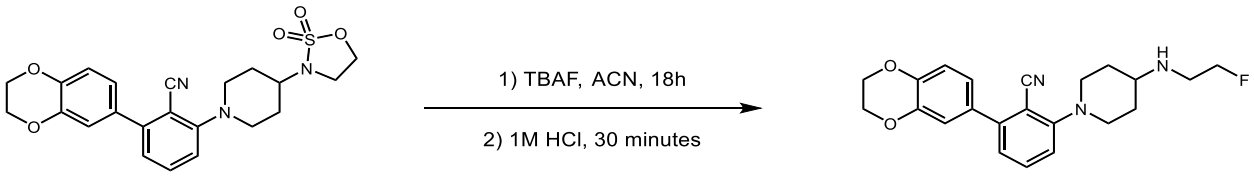

2-(2,3-dihydrobenzo[b][1,4]dioxin-6-yl)-6-(4-((2-fluoroethyl)amino)piperidin-1-yl)benzonitrile. 13 mg 2-(2,3-dihydrobenzo[b][1,4]dioxin-6-yl)-6-(4-(2,2-dioxido-1,2,3-oxathiazolidin-3-yl)piperidin-1-yl)benzonitrile was dissolved in 2 mL dry acetonitrile. To this was added 300 microliters tetrabutyl ammonium fluoride (1.0M in THF). This was stirred overnight at room temperature. Then, 5 mL of 1M hydrochloric acid was added and the reaction stirred for 30 minutes then the reaction was concentrated by half. Dichloromethane (5 mL) and water (2 mL) was added and the aqueous layer extracted with dichloromethane (2x 10 mL). Organics combined, dried, and concentrated. Concentrated to a crude solid which was purified by silica chromatography (0-10% methanol in dichloromethane). 4 mg, 36%

2.12.4 Radiochemical Synthesis of ^{18}F Labeled Tracer

The [^{18}F]fluoride was produced at Emory University with a 11 MeV Siemens RDS 112 negative-ion cyclotron (Knoxville, TN, USA) by the $^{18}O(p,n)^{18}F$ reaction using [^{18}O]H_2O (95%). The automated radiosyntheses were performed in a chemical process control unit (CPCU) obtained from CTI, Inc. (Knoxville, TN, USA). Silica and alumina SepPaks and HLB Oasis cartridges were purchased from Waters, Inc. (Milford, MA, USA). The columns used for ion retardation (IR) chromatography and the IR resin AG 11 A8 (biotechnology grade) were purchased from Bio-Rad

Laboratories (Hercules, CA, USA). Trap/release cartridges model DW-TRC were purchased from D&W, Inc. (Oakdale, TN, USA). The reaction vessel used in the CPCU were borosilicate glass purchased from Pacific Flame Glass Works (Emeryville, CA, USA), and the vials used for reagents were borosilicate glass Microvial v-vials of appropriate volume fitted for aluminum seals purchased from Kimble/Kontes (Vineland, NJ, USA). Radiometric thin layer chromatography was performed with 0.25 mm silica adsorbed to aluminum plates obtained from Whatman, Inc. (Clifton, NJ, USA) and analyzed using a Bioscan System 200 (Washington, DC, USA).

2.12.5 Binding Affinity by Surface Plasmon Resonance

HJZ-5-164 and PD-L1 binding kinetics were measured via biolayer interferometry using an Octet RED384 system (ForteBio). Nickel nitrilotriacetic acid sensors (Ni-NTA, ForteBio) were equilibrated in kinetics buffer (PBS, 0.02% Tween20, 0.1% BSA, 0.05% sodium azide) and coated with polyhistidine-tagged PD-L1(SinoBiological) for 60 seconds (25 ug/mL). Association kinetics were measured over 250-500 seconds at 5.2 2.5 1.25 and 0.6 uM HJZ-5-164 followed by dissociation in kinetics buffer over 250-500 seconds. Measurements were repeated in three independent experiments and fit using Data Analysis 11.1 (ForteBio) using a 1:1 kinetic model.

Chapter 3:

Development of a Highly Potent and Efficacious Liver Receptor Homolog-1 Agonist

Jeffery Cornelison and Autumn Flynn developed the synthetic routes to compounds described herein. Jeffery Cornelison synthesized and characterized some of the compounds used in biological assays. Michael Cato, Anamika Patel, Denise Okafor, and Emma D'Agostino performed biochemical assays and ran the molecular dynamics simulations.

Abstract: Liver receptor homolog 1 (LRH-1) is a nuclear receptor that regulates gene expression in pathways related to bile acid synthesis, reverse cholesterol transport and lipid homeostasis. These pathways are attractive targets for therapeutic intervention in intestinal inflammation and cardiovascular diseases. While the native ligands for these receptors are phospholipids, these molecules make poor therapeutics due to poor pharmacokinetics and potency. Here we compare the activity of two LRH-1 agonists developed in our group in addition to a hybrid ligand combining individual elements of each prior ligand. These elements interact with two different sets of polar residues, one at the mouth of the binding pocket and the other deep within. We show that interaction with both sets of polar residues results in superior binding to LRH-1 and downstream gene expression consistent with the native ligand. Interestingly, binding different polar residues leads to differential coactivator recruitment and gene expression, demonstrating the possibility of selective modulation of certain downstream genes.

3.1 Liver Receptor Homolog 1 (LRH-1)

3.1.1 Orphan Nuclear Receptors

Liver Receptor Homolog 1 (NR5A2, LRH-1) is an orphan nuclear receptor crucial to development and lipid homeostasis[41,42]. There is formally no endogenous ligand (orphan receptor), however LRH-1 regulates a wide range of genes (nuclear receptor) in the liver, ovaries, breast, and colon, among other organs. In fetal tissues, it is responsible for maintenance of pluripotency and regulates the differentiation of the intestine, liver, and pancreas[43].

In adults, LRH-1 regulates bile acid synthesis, lipogenesis, and reverse cholesterol transport. Additionally, LRH-1 regulates steroidogenesis in ovary, breast preadipocytes, intestinal, and pancreatic tissues, which is responsible for its role in cancer pathology[44,45]. LRH-1, as a druggable nuclear receptor, represents an attractive "control switch" to modulate a wide range of diseases that impact human health today.

---

[41] Lu TT, Makishima M, Repa JJ, Schoonjans K, Kerr TA, Auwerx J, Mangelsdorf DJ. Molecular basis for feedback regulation of bile acid synthesis by nuclear receptors. Mol Cell 2000; 6(3):507-15; PMID:11030331; http://dx.doi.org/10.1016/S1097-2765(00)00050-2

[42] Nitta M, Ku S, Brown C, Okamoto AY, Shan B. CPF: an orphan nuclear receptor that regulates liver-specific expression of the human cholesterol 7alpha-hydroxylase gene. Proc Natl Acad Sci U S A 1999; 96(12):6660-5; PMID:10359768; http://dx.doi.org/10.1073/pnas.96.12.6660

[43] Fayard E, Auwerx J, Schoonjans K. LRH-1: An orphan nuclear receptor involved in development, metabolism and steroidogenesis. Trends Cell Biol 2004; 14(5):250-60; PMID:15130581; http://dx.doi.org/10.1016/j.tcb.2004.03.008

[44] Liu DL, Liu WZ, Li QL, Wang HM, Qian D, Treuter E, Zhu C. Expression and functional analysis of liver receptor homologue 1 as a potential steroidogenic factor in rat ovary. Biol Reprod 2003; 69(2):508-17; PMID:12672674; http://dx.doi.org/10.1095/biolreprod.102.011767

[45] Benod C, Vinogradova MV. Jouravel N, Kim GE, Fletterick RJ, Sablin EP. Nuclear receptor liver receptor homologue 1 (LRH-1) regulates pancreatic cancer cell growth and proliferation. Proc Natl Acad Sci 2011; 108(41):16927-31; PMID:21949357; http://dx.doi.org/10.1073/pnas.1112047108

3.1.2 Activation of LRH-1

A nuclear receptor, as a transcription factor, directly binds DNA and activates genes for expression. The hydrophobic ligands of nuclear receptors (e.g. steroid hormones) are privileged in their ability to move readily throughout the body and pass through membranes and are thus responsible for organism level intercellular communication and signaling[46]. Depicted in Figure 3.1, LRH-1's activation begins with a phospholipid binding in the ligand binding domain (LBD). Next, the activation function helix (AF-H) rotates and packs against the LBD, forming the activation function surface (AFS) and recruits coactivator proteins[47]. Contrary to canonical nuclear receptor activity, LRH-1 does not transmit the ligand binding event through the helices of the protein; the ligand binding is transmitted through the residues at the distal end of the pocket (i.e. G421, Y516, and K520), the hydrophobic contacts deep in the pocket, and crucially, through the

[46] Sever, R., & Glass, C. K. (2013). Signaling by nuclear receptors. *Cold Spring Harbor Perspectives in Biology*, *5*(3). https://doi.org/10.1101/cshperspect.a016709

[47] Musille, P. M., Kohn, J. A., & Ortlund, E. A. (2013). Phospholipid-Driven gene regulation. In *FEBS Letters* (Vol. 587, Issue 8, pp. 1238–1246). https://doi.org/10.1016/j.febslet.2013.01.004

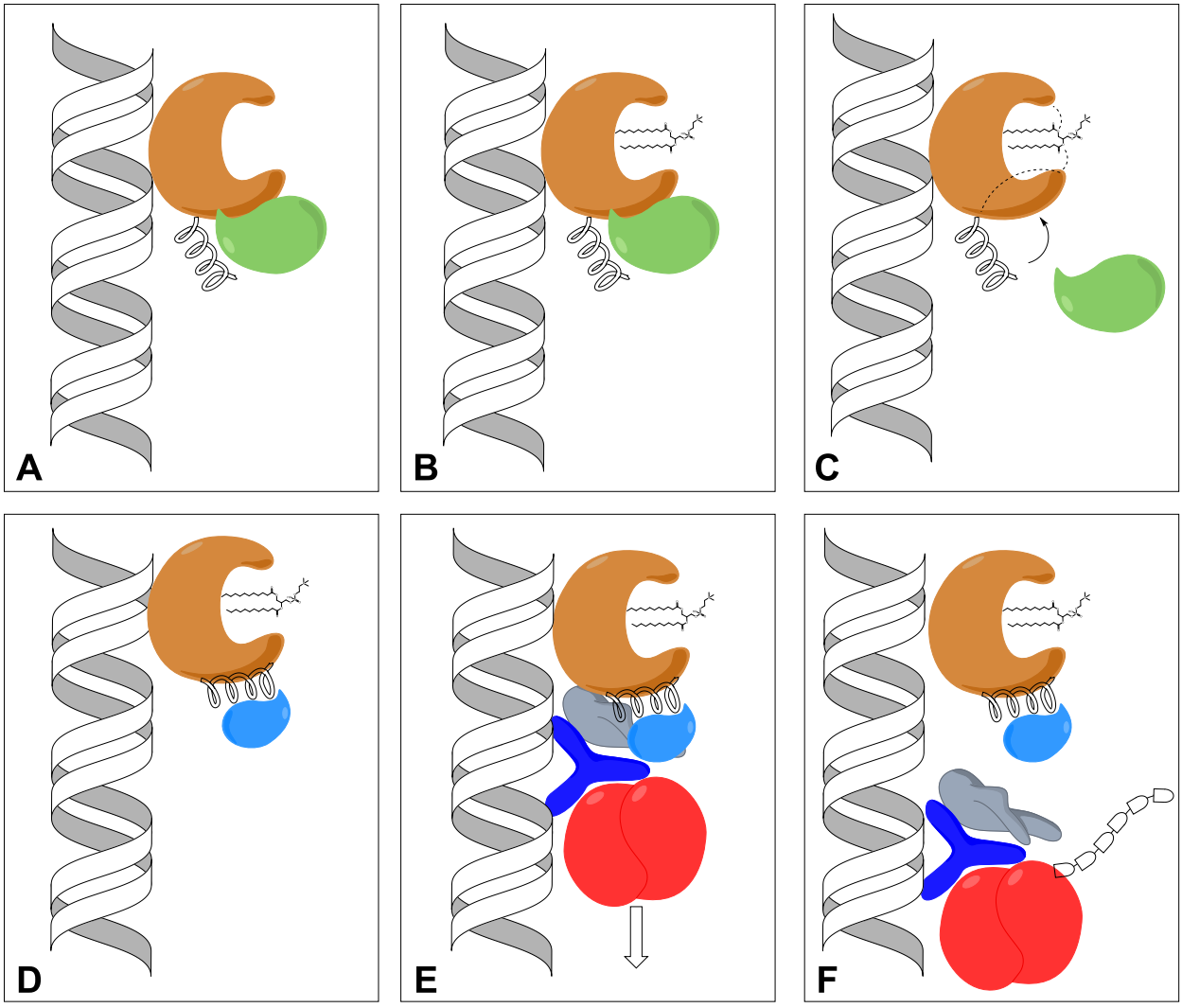

Figure 3.1 LRH-1 ligand binding initiates transcription of target genes.

Panel A) LRH-1 (orange) in the resting state with corepressors (green). **Panel B)** DLPC binds in the LBD. **Panel C)** Ligand binding initiates communication from helices 2, 3, 6 and 7 through the ligand at the mouth of the pocket and through the deep pocket to the AF-H. **Panel D)** AF-H rotates tight against the LBD which forms the AFS, and recruits coactivators (blue). **Panel E)** coactivator recruitment in turn localizes transcriptional machinery, including RNA polymerase II (red). **Panel F)** transcriptional machinery begins to read off the gene, causing target gene expression

ligand itself. Once the AFS is in an active form, various coactivators can bind and assemble the larger transcriptional machinery, expressing the target genes. Interestingly, the identity of the ligand defines the suite of coactivators that are recruited to the AFS. This may explain the differential roles and genes expressed based on the tissue that LRH-1 is in. However, that same coactivator specificity can be leveraged to achieve the desired tissue specific pharmacological effects while avoiding disturbance of normal physiological function in other tissues.

3.1.3 Natural Agonists of LRH-1

Despite being formally classified as an orphan nuclear receptor, the native ligands are reasonably well understood[48]. When purified from bacterial expression systems, the protein's ligand binding pocket contains medium chain phospholipids. As genes responsible for lipogenesis are major targets for LRH-1 regulation, binding of phospholipids generates a regulatory feedback-loop regime analogous to ones seen in many metabolic pathways. Further research to probe the exact identity of the ligands typically bound to LRH-1 has shown a distinct influence of chain length in binding affinity[49].

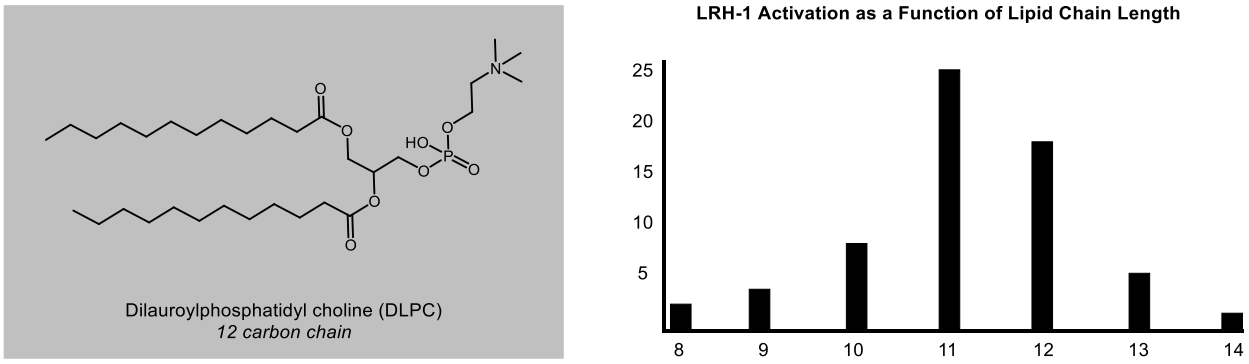

Figure 3.2 LRH-1 agonistic activity is tightly correlated to size of phospholipid chain length

Dilauroyl phosphatidyl choline (DLPC, PC 12:0/12:0) and diundecanoyl phosphatidyl choline (DUPC; PC 11:0/11:0) both possess modest LRH-1 binding activity (Figure 3.2). When the chain of DLPC extended, even by a single methylene, the binding affinity is significantly compromised. DUPC and DLPC have been studied for treatment of metabolic diseases in

[48] Krylova IN, Sablin EP, Moore J, Xu RX, Waitt GM, MacKay JA, Juzumiene D, Bynum JM, Madauss K, Montana V, et al.. Structural analyses reveal phosphatidyl inositols as ligands for the NR5 orphan receptors SF-1 and LRH-1. Cell 2005; 120(3):343-55; PMID:15707893; http://dx.doi.org/10.1016/j.cell.2005.01.024

[49] Ortlund EA, Lee Y, Solomon IH, Hager JM, Safi R, Choi Y, Guan Z, Tripathy A, Raetz CR, McDonnell DP, et al.. Modulation of human nuclear receptor LRH-1 activity by phospholipids and SHP. Nat Struct Mol Biol 2005; 12(4):357-63; PMID:15723037; http://dx.doi.org/10.1038/nsmb910

preclinical as well as clinical studies, but because of their pharmacokinetic properties, propensity for biotransformation, and known polypharmacology, they are poorly suited for therapeutic use.

3.1.4 Synthetic Agonists of LRH-1

In 2006, the first synthetic agonist of LRH-1 was disclosed by a group at GlaxoSmithKline and University of Southampton[50]. This molecule, named GSK8470 (Figure 3.3), was a breakthrough given no endogenous ligand is known. However, the compound is acid sensitive, decomposing even on silica gel, which hampers its utility in biological assays or systems. Further refinement of the cis-bicyclo[3,3,0]oct-2-ene scaffold to remove the bridgehead aniline moiety afforded RJW-100, an acid insensitive analog (stable to camphor sulfonic acid in $CDCl_3$ for 24h)[51]. This compound was an attractive starting point for our lab to initiate structure-activity relationship (SAR) studies.

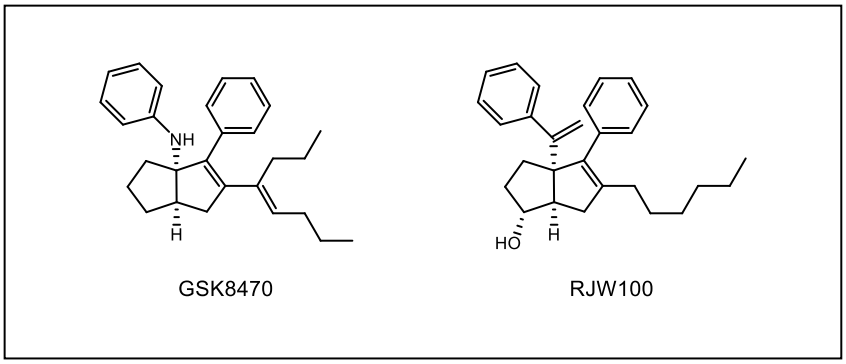

Figure 3.3 Early LRH-1 synthetic agonists

[50] Whitby, R. J., Dixon, S., Maloney, P. R., Delerive, P., Goodwin, B. J., Parks, D. J., & Willson, T. M. (2006). Identification of small molecule agonists of the orphan nuclear receptors liver receptor homolog-1 and steroidogenic factor-1. *Journal of Medicinal Chemistry*, *49*(23), 6652–6655. https://doi.org/10.1021/jm060990k

[51] Whitby, R. J., Stec, J., Blind, R. D., Dixon, S., Leesnitzer, L. M., Orband-Miller, L. A., Williams, S. P., Willson, T. M., Xu, R., Zuercher, W. J., Cai, F., & Ingraham, H. A. (2011). Small molecule agonists of the orphan nuclear receptors steroidogenic factor-1 (SF-1, NR5A1) and liver receptor homologue-1 (LRH-1, NR5A2). *Journal of Medicinal Chemistry*, *54*(7), 2266–2281. https://doi.org/10.1021/jm1014296

Seeking to improve the activity of RJW-100, we hypothesized that incorporating elements of the phospholipids known to agonize LRH-1 natively might improve the binding affinity. To that end, a compound was designed that contained the greasy bicyclo[3,3,0]oct-2-ene core that was known to have LRH-1 potency, and add the phosphatidylcholine portion that is present on phospholipids[52]. This compound proved more potent than previous derivatives but presented significant synthetic hurdles (Figure 3.4). To facilitate further derivatization, the polar tail was pared down from phosphatidylcholine to a simple carboxylic acid. This compound retained the activity of the phospholipid mimic without the pharmacological liabilities. Subsequent studies to determine the ideal chain length were undertaken and it was found that 10 carbons provided maximum activation as it presents the carboxylate in close proximity to key residues at the mouth

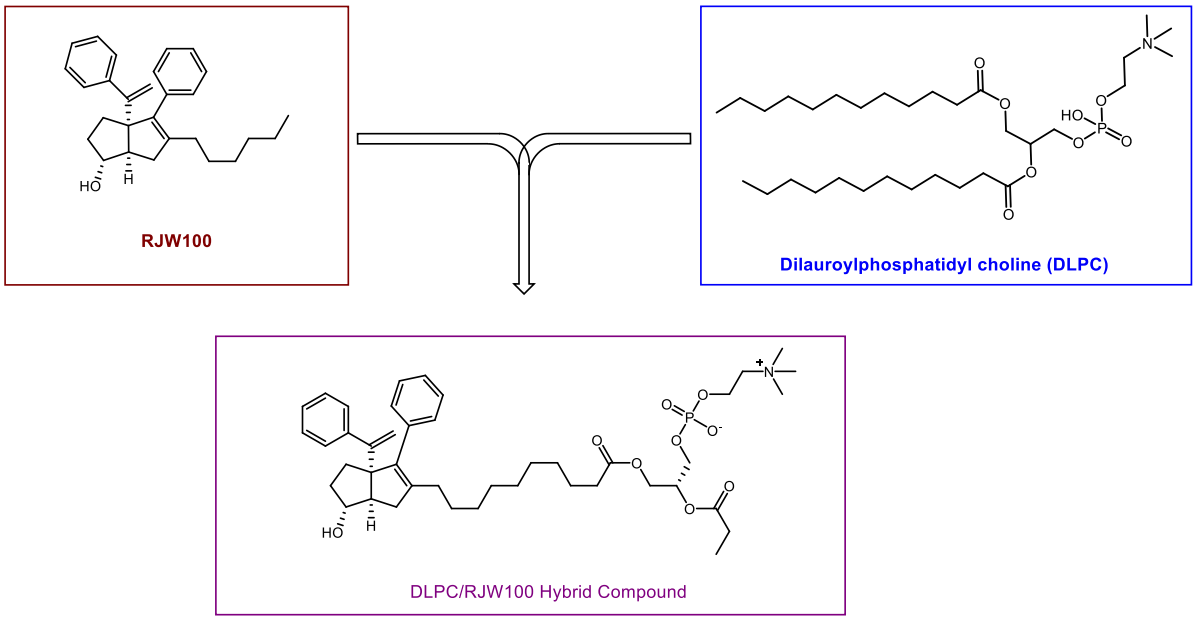

Figure 3.4 Hybridizing elements from phospholipids and published agonists yields "phospholipid mimic"

[52] Flynn, A. R., Mays, S. G., Ortlund, E. A., & Jui, N. T. (2018). Development of Hybrid Phospholipid Mimics as Effective Agonists for Liver Receptor Homologue-1. *ACS Medicinal Chemistry Letters*, *9*(10), 1051–1056. https://doi.org/10.1021/acsmedchemlett.8b00361

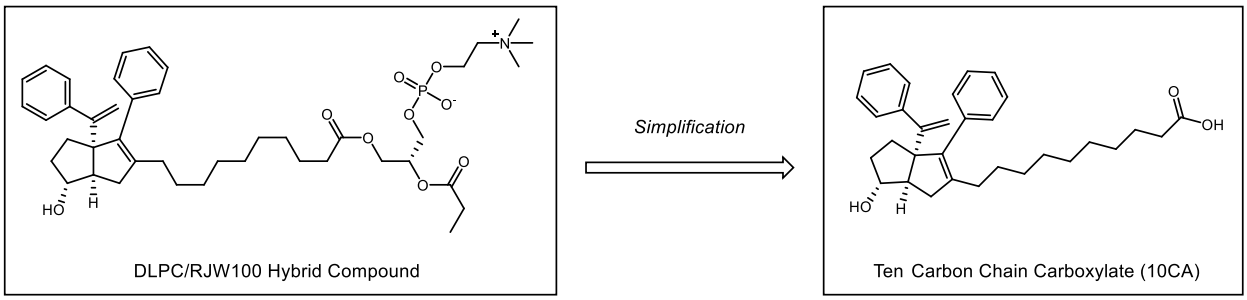

Figure 3.5 Simplification of phospholipid mimic into ten carbon carboxylate (10CA)

of the binding pocket (Figure 3.5). Concurrently, the polar headgroup and pendant arenes were being optimized using information gleaned from structural biology efforts[53].

Based on the structural information it appeared that improving the pi stacking interaction between the pendant styrenyl arene and a nearby histidine would be fruitful, but no modification at this site proved advantageous. The key element of RJW-100 binding is the network of bound water molecules deep in the pocket of the protein. This network is what interacts with the alcohol moiety of the bicyclo[3,3,0]oct-2-ene. Theorizing that a larger polar function might be able to displace one of the bound waters, a series of analogs probed that question. It was found that the *endo*-sulfamide (6N) formed far stronger interactions at this important site and was the highest potency LRH-1 agonist discovered at the time.

3.2 LRH-1 in Human Disease

The human liver is the largest organ in the body and plays a crucial role in managing the body's supply of nutrients. It produces and secretes liver specific biomolecules such as bile acids

[53] Mays, S. G., Flynn, A. R., Cornelison, J. L., Okafor, C. D., Wang, H., Wang, G., Huang, X., Donaldson, H. N., Millings, E. J., Polavarapu, R., Moore, D. D., Calvert, J. W., Jui, N. T., & Ortlund, E. A. (2019). Development of the First Low Nanomolar Liver Receptor Homolog-1 Agonist through Structure-guided Design. *Journal of Medicinal Chemistry*, *62*(24), 11022–11034. https://doi.org/10.1021/acs.jmedchem.9b00753

and ketone bodies, as well as storing minerals and vitamins[54]. It synthesizes carbohydrates, proteins, and lipids as well as important blood factors. Its role in these processes is a function of being directly downstream from the digestive tract in the vasculature—all food, vitamins, minerals and drugs taken in by the body are processed by the liver prior to going anywhere else. This location facilitates its role managing the nutrients and energy doled out to the rest of the body[55].

3.2.1 Cardiovascular disease

LRH-1 is highly expressed in hepatocytes where it is responsible for several of the many pathways regulated by the liver. One pathway governed by LRH-1 is reverse cholesterol transport[56]. This process is how excess cholesterol is removed from the bloodstream and tissues, preventing atherosclerosis. Additionally, LRH-1 regulates many of the bile acid synthesis pathways, which indirectly controls the amount and types of lipids that are brought into the blood stream from the digestive tract[57]. This in concert with its regulatory role in glucose and lipid metabolism highlight

---

[54] Hofmann, A. F. (n.d.). *The Continuing Importance of Bile Acids in Liver and Intestinal Disease*. https://jamanetwork.com/

[55] Alamri, Z. Z. (2018). The role of liver in metabolism: an updated review with physiological emphasis. *International Journal of Basic & Clinical Pharmacology*, *7*(11), 2271. https://doi.org/10.18203/2319-2003.ijbcp20184211

[56] Schoonjans, K., Annicotte, J.-S., Huby, T., Botrugno, O. A., Fayard, E., Ueda, Y., Chapman, J., & Auwerx, J. (2002). Liver receptor homolog 1 controls the expression of the scavenger receptor class B type I. In *EMBO reports* (Vol. 3, Issue 12).

[57] Lee YK, Schmidt DR, Cummins CL, Choi M, Peng L, Zhang Y, Goodwin B, Hammer RE, Mangelsdorf DJ, Kliewer SA. Liver receptor homolog-1 regulates bile acid homeostasis but is not essential for feedback regulation of bile acid synthesis. Mol Endocrinol. 2008 Jun;22(6):1345-56. doi: 10.1210/me.2007-0565.

the significance of LRH-1 in cardiovascular and metabolic diseases, the leading cause of death worldwide.

3.2.2 Non-alcoholic fatty liver disease

Non-alcoholic fatty liver disease (NAFLD) is the most common form of liver disease and is linked to type II diabetes, obesity, and insulin resistance[58]. NAFDL is characterized by lipid droplets deposited in hepatocytes, known as steatosis. In some patients this progresses to steatohepatitis which ultimately leads to fibrosis, cirrhosis and carcinoma. Despite the increasing incidence of NAFLD as a result of sedentary lifestyles and changes in diet, there are no targeted therapies available for NAFLD[59]. Steatosis is a direct result of imbalanced lipid transport and metabolism and is thus strongly associated with the functions LRH-1 regulates. Thus the synthetic agonists developed are highly attractive in reducing the disease burden of NAFLD.

3.3 Introduction

Multiple studies have shown that LRH-1 can bind a variety of phospholipids (PLs)[60] and is activated by dietary PL 1,2-dilauroyl-sn-glycero-3-phosphocholine (DLPC) *in vitro* and in

---

[58] Younossi, Z., Anstee, Q. M., Marietti, M., Hardy, T., Henry, L., Eslam, M., George, J., & Bugianesi, E. (2018). Global burden of NAFLD and NASH: Trends, predictions, risk factors and prevention. In *Nature Reviews Gastroenterology and Hepatology* (Vol. 15, Issue 1, pp. 11–20). Nature Publishing Group. https://doi.org/10.1038/nrgastro.2017.109

[59] Neuschwander-Tetri, B. A. (2020). Therapeutic Landscape for NAFLD in 2020. *Gastroenterology*, *158*(7), 1984-1998.e3. https://doi.org/10.1053/j.gastro.2020.01.051

[60] Ortlund EA, Lee Y, Solomon IH, Hager JM, Safi R, Choi Y, Guan Z, Tripathy A, Raetz CR, McDonnell DP, Moore DD, Redinbo MR. Modulation of human nuclear receptor LRH-1 activity by phospholipids and SHP. Nat Struct Mol Biol. 2005;12(4):357-63. Epub 2005/02/22. doi: 10.1038/nsmb910. PubMed PMID: 15723037.

mice[61,62]. However, because of the insolubility and poor potency of DLPC, synthetic agonists are needed to effectively activate the receptor for clinical and laboratory purposes. The leading member of the first class of synthetic LRH-1 agonists based on the hexahydropentalene scaffold ("RJW100," Figure 3.6) adopts an orientation distinct from that of PLs (Figure 3.6).[60,61,63] While PL head groups bind hydrophilic residues at the mouth of the ligand binding pocket (LBP), the RJW100 hydroxyl group contacts polar residues deep within the pocket through a conserved network of water molecules

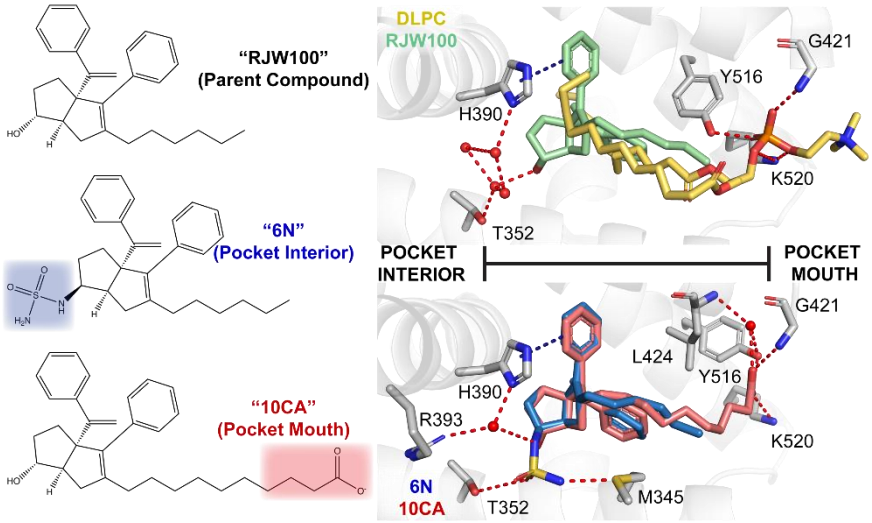

Figure 3.6 LRH-1 agonist structures and binding orientations.

Left: Chemical structures of leading LRH-1 synthetic agonists. Right: Binding pose of activating phospholipid DLPC (yellow, PDB 4DOS), RJW100 (green, PDB 5L11), 6N (blue, PDB 6OQY), and 10CA (red, unpublished). Residue sidechains are shown as sticks (O=red, N=blue, S=yellow), water molecules are shown as spheres, and bonds are represented as dotted lines (red=hydrogen, blue= π–π stacking).

---

[61] Musille PM, Pathak M, Lauer JL, Hudson WH, Griffin PR, Ortlund EA. Antidiabetic phospholipid-nuclear receptor complex reveals the mechanism for phospholipid-driven gene regulation. Nat Struct Mol Biol. 2012;19(5):532-S2. Epub 2012/04/17. doi: 10.1038/nsmb.2279. PubMed PMID: 22504882; PMCID: PMC3960984.

[62] Lee JM, Lee YK, Mamrosh JL, Busby SA, Griffin PR, Pathak MC, Ortlund EA, Moore DD. A nuclear-receptor-dependent phosphatidylcholine pathway with antidiabetic effects. Nature. 2011;474(7352):506-10. Epub 2011/05/27. doi: 10.1038/nature10111. PubMed PMID: 21614002; PMCID: PMC3150801.

[63] Mays SG, Okafor CD, Whitby RJ, Goswami D, Stec J, Flynn AR, Dugan MC, Jui NT, Griffin PR, Ortlund EA. Crystal Structures of the Nuclear Receptor, Liver Receptor Homolog 1, Bound to Synthetic Agonists. J Biol Chem. 2016;291(49):25281-91. Epub 2016/10/04. doi: 10.1074/jbc.M116.753541. PubMed PMID: 27694446; PMCID: PMC5207232.

(Figure 3.6). We used structure-guided approaches to target nearby hydrophilic residues in the LBP to improve compound solubility, potency, and efficacy. By making direct contact with deep-pocket polar residues, we developed a compound ("6N," Figure 3.6) that activates the receptor with nanomolar potency[64]. Furthermore, we have recently used a strategy that targets residues contacted by activating PLs to engage the endogenous route of LRH-1 activation.[52,53] This resulted in a small molecule ("10CA," Figure 3.6) that was able to alleviate DSS-induced intestinal epithelial damage, improve disease activity, and accelerate weight gain in a model for intestinal inflammation. Our work in agonist development has therefore culminated in two compounds that make unique contacts with distinct sets of hydrophilic residues in the LBP. Both compounds achieve activation through distinct mechanisms, with 6N exhibiting stronger potency and 10CA elevating efficacy. We reasoned that we could combine features of both agonists to capture the benefits of engagement with both LBP sites.

Here, we show that an agonist contacting both hydrophilic sites (termed "6N-10CA") exhibits elevated affinity, potency, and receptor communication with the AFS. Notably, while 6N-10CA activates LRH-1 to an equivalent level as 10CA in reporter assays, it elicits LRH-1 target gene expression to a greater degree than either 6N or 10CA in HepG2 cells. Additionally, 6N-10CA promotes an expression profile that resembles DLPC-mediated effects on metabolic genes, which are downregulated by 6N. Mechanistic studies reveal that small molecules exert differential effects on LRH-1 activity depending upon which coregulator is dominant in the cell, suggesting that the two sets of hydrophilic residues contacted by lead agonists promote differential coregulator

[64] Mays SG, Flynn AR, Cornelison JL, Okafor CD, Wang H, Wang G, Huang X, Donaldson HN, Millings EJ, Polavarapu R, Moore DD, Calvert JW, Jui NT, Ortlund EA. Development of the First Low Nanomolar Liver Receptor Homolog-1 Agonist through Structure-guided Design. J Med Chem. 2019;62(24):11022-34. Epub 2019/08/17. doi: 10.1021/acs.jmedchem.9b00753. PubMed PMID: 31419141.

preference. Our work thus provides critical information regarding the distinct features of leading agonists and characterizes a highly active compound that bridges agonistic modifications.

3.4 Results

Our previous studies on compounds **6N** and **10CA** leveraged the modular construction of these molecules for rapid access to derivatives used for structure-activity relationship studies[52,53]. Fortuitously, the sulfamide moiety responsible for the high potency of **6N** is incorporated into the hexahydropentalene core on a different fragment than the ten-carbon carboxylic acid "tail" that confers high agonistic efficacy to **10CA**. Thus, synthesis of a hybridized version containing both the sulfamide as well as the ten-carbon carboxylic acid tail was straightforward.

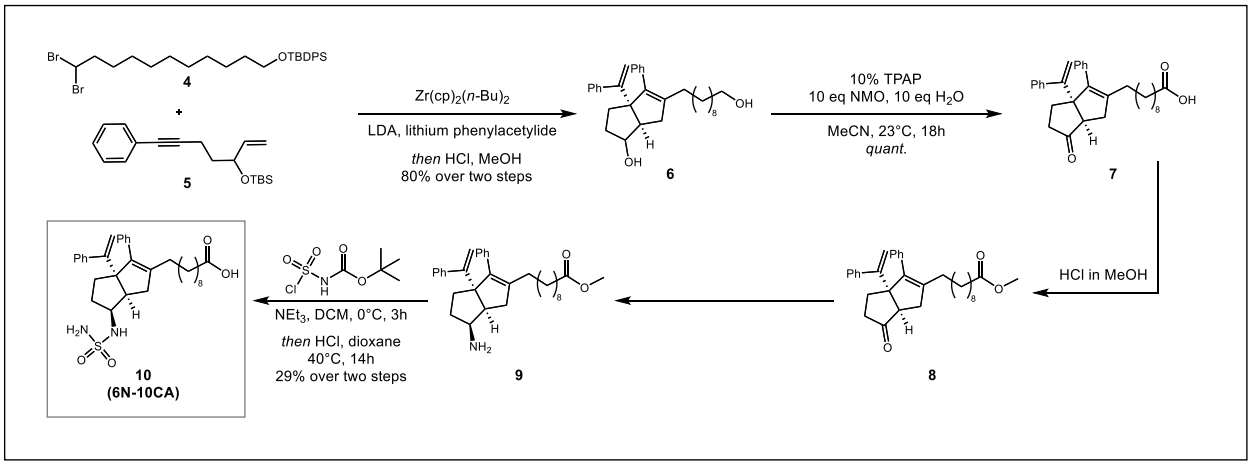

Scheme 6. Synthesis of 6N-10CA hybrid compound

Synthesis of **6N-10CA** began with generation of diol **6** from enyne **5** and protected 11,11-dibromoundecan-1-ol **4**, as reported by our group previously (Scheme 6). Next, Ley-Griffith oxidation of the diol furnished the ketoacid **7**, which was then esterified under Fisher conditions. Reductive amination of the ketone function with methanolic ammonia utilizing anhydrous

titanium^{IV} isopropoxide produced primary amine **9** in excellent yield (81%). After amine installation, sulfamidation with freshly prepared *tert*-butyl chlorosulfonyl carbamate followed by acidic global deprotection furnished **6N-10CA** in 29% over two steps.

Targeting polar residues deep within, and at the mouth of the pocket has proven to be an effective strategy for improving compound binding and potency.[52,53,65] To compare binding affinity and potency of small molecules that contact one or both polar sites, we performed an FP competition assay developed in our lab,[65] as well as a luciferase reporter assay used to assess small-molecule mediated activation of LRH-1 in previous studies.[52] Trends for 6N and 10CA mirrored reported data,[52,53,66] with 6N exhibiting greater affinity (K_i) and potency (EC_{50}) than 10CA, and 10CA exhibiting greater efficacy (fold-activation) than 6N. Interestingly, 6N-10CA displayed picomolar affinity, approximately 10-fold higher than that of 6N (Figure 3.7 A, D), representing the first picomolar affinity LRH-1 ligand to date. Luciferase reporter assays demonstrated the same trend, with 6N-10CA exhibiting the highest potency. Interestingly, 6N-10CA exhibited a similar fold activation as that of 10CA (Figure 3.7 B, D), suggesting that the tail modification preserves an elevated efficacy granted by contacting polar residues at the pocket mouth.

Previous studies have shown that LRH-1 small molecule agonists stabilize the LBD, however, potency does not always correlate with the degree of stabilization.11 We therefore compared

---

[65] D'Agostino EH, Flynn AR, Cornelison JL, Mays SG, Patel A, Jui NT, Ortlund EA. Development of a Versatile and Sensitive Direct Ligand Binding Assay for Human NR5A Nuclear Receptors. ACS Med Chem Lett. 2020;11(3):365-70. Epub 2020/03/19. doi: 10.1021/acsmedchemlett.9b00442. PubMed PMID: 32184971; PMCID: PMC7074214

[66] Cornelison JL, Cato ML, Johnson AM, D'Agostino EH, Melchers D, Patel AB, Mays SG, Houtman R, Ortlund EA, Jui NT. Development of a new class of liver receptor homolog-1 (LRH-1) agonists by photoredox conjugate addition. Bioorg Med Chem Lett. 2020;30(16):127293. Epub 2020/07/08. doi: 10.1016/j.bmcl.2020.127293. PubMed PMID: 32631515; PMCID: PMC7701997.

compound-mediated thermal stability of the LRH-1 LBD between agonists. Each compound increased the stability of the receptor relative to DLPC, with 6N-10CA displaying the greatest degree of stabilization, improving thermal stability by approximately 12.2°C, followed by 6N (+9.4°C) and 10CA (+6.2°C) (Fig. 2C, D). Overall, this suggests that contacting hydrophilic residues within and at the mouth of the pocket enhances affinity, potency, and stability of the receptor in an additive manner, while preserving efficacy permitted by LBP mouth contacts.

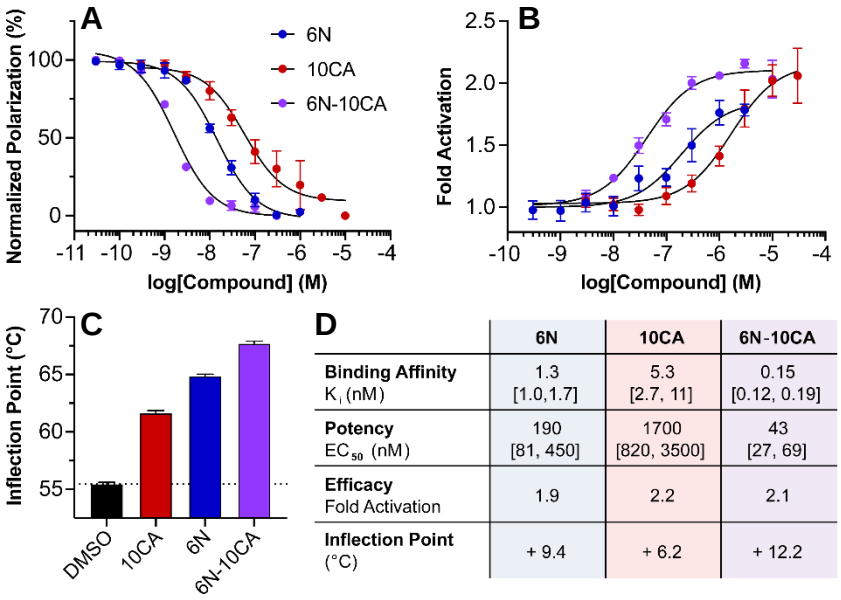

	6N	10CA	6N-10CA
Binding Affinity K_i (nM)	1.3 [1.0,1.7]	5.3 [2.7, 11]	0.15 [0.12, 0.19]
Potency EC_{50} (nM)	190 [81, 450]	1700 [820, 3500]	43 [27, 69]
Efficacy Fold Activation	1.9	2.2	2.1
Inflection Point (°C)	+ 9.4	+ 6.2	+ 12.2

Figure 3.7 Comparison of agonist binding, potency, efficacy, and thermal stability.

A. FP competition assay shows 6N-10CA exhibits highest binding affinity. **B.** 6N-10CA exhibits the highest potency in luciferase reporter assay and a similar efficacy as 10CA. **C.** 6N-10CA stabilizes the LRH-1 LBD to the highest degree in thermal shift assays. The inflection point corresponds to the temperature at which the protein unfolds. Data shown as mean ± SEM from two independent experiments (FP), four biological replicates (luciferase), or three independent experiments (thermal shift). **D.** Summary of data. 95% confidence intervals shown in brackets.

To investigate how small molecules compare in driving LRH-1 target gene expression, we performed RT-qPCR analysis of LRH-1 target genes CYP7A1 and SHP in HepG2 cells, a liver-derived cell line commonly used to assess LRH-1 activity. Interestingly, 10CA did not alter expression of either target gene, while 6N increased expression of CYP7A1. Importantly, 6N-10CA was the only small molecule to drive SHP expression and induced expression of CYP7A1 to an equivalent degree as 6N (Fig. 3A). This suggests that 6N-10CA may be the most effective

small molecule in driving LRH-1 target gene expression, and that some LRH-1 target genes may be selectively responsive to certain classes of LRH-1 agonists. These data also suggest that while leading agonists each stabilize LRH-1 and drive reporter activity, effects on gene expression may differ substantially in a cellular context.

Differences in agonist-driven SHP expression led us to hypothesize that inclusion of the carboxylate tail on 6N-10CA can have a radically different effect on downstream gene expression.

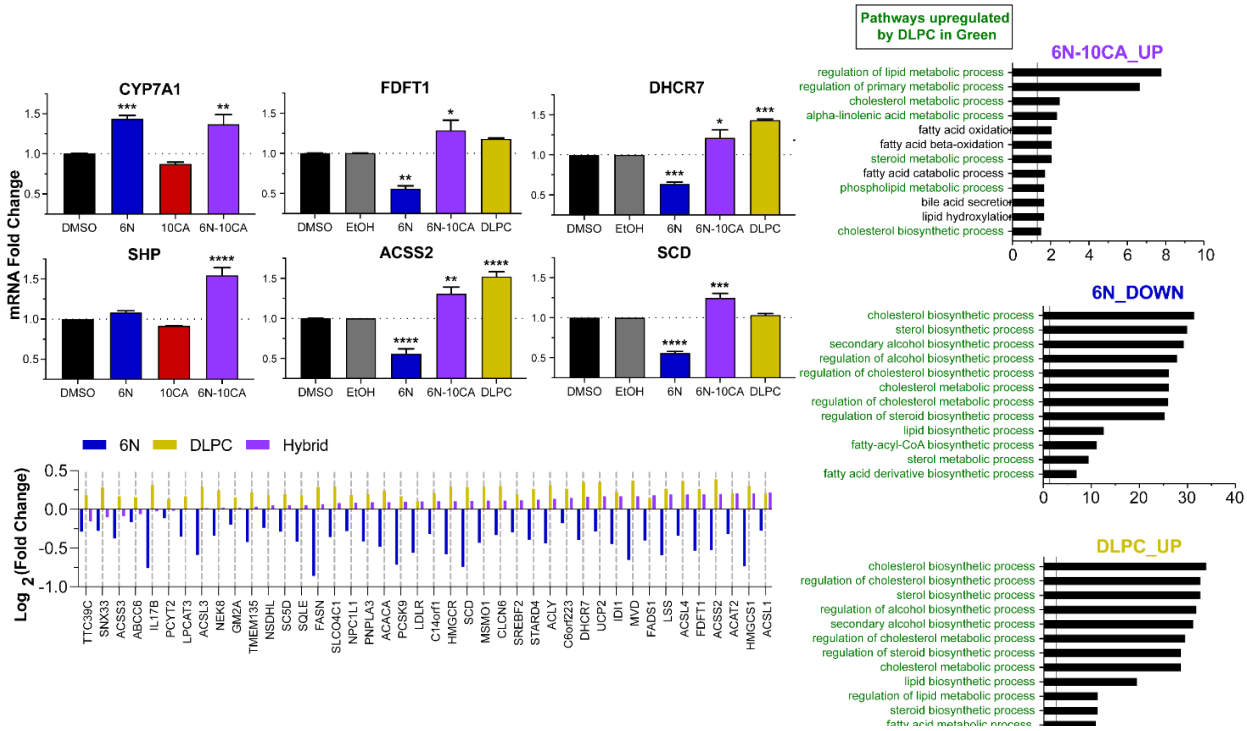

Figure 3.8 LRH-1 agonists promote different transcriptional profiles in HepG2 cells.

A. RT-qPCR analysis of HepG2 cells treated with agonists for 24 hrs. Data shown as mean ± SEM from three biological replicates. One-way ANOVA and Bonferroni Multiple Comparisons Test, *p < 0.05, **p < 0.01, ***p < 0.001, ****p < 0.0001 **B.** GO pathway analysis of cells treated with 6N-10CA, 6N, and DLPC. Genes used in analysis were those significantly (p < 0.05) up- (6N-10CA, DLPC) or downregulated (6N) by compounds. Adjusted p-value cutoff of 0.05 indicated by gray line. **C.** mRNA levels of genes significantly (p < 0.05) upregulated by DLPC and downregulated by 6N are shown.

To explore these differences, we performed RNA-seq analysis on HepG2 cells treated with 6N-10CA, 6N, and activating PL DLPC (Figure 3.8). Notably, DLPC- and 6N-treated cells exhibit divergent effects on metabolic pathways, with genes responsible for cholesterol and lipid

homeostasis upregulated by DLPC and downregulated by 6N (Figure. 3.8 B). Closer inspection revealed 42 genes upregulated by DLPC and downregulated by 6N. Importantly, these DLPC gene expression patterns were mirrored in 6N-10CA-treated cells (Fig. 3 B, C). To further assess whether 6N-10CA recapitulated expression profiles of 6N or DLPC, we used RT-qPCR analysis to individually examine overlapping genes in DLPC-upregulated and 6N-downregulated expression signatures. Examination of four key metabolic genes up- and down-regulated by DLPC and 6N, respectively, show that 6N-10CA consistently drives an increase in mRNA levels of metabolic genes that are downregulated by 6N (Fig. 3.8A). This suggests that the favorable contact of the LBP mouth by the carboxylate drives a substantial difference in downstream gene expression output and that 6N-10CA promotes an expression profile resembling that of activating PL DLPC.

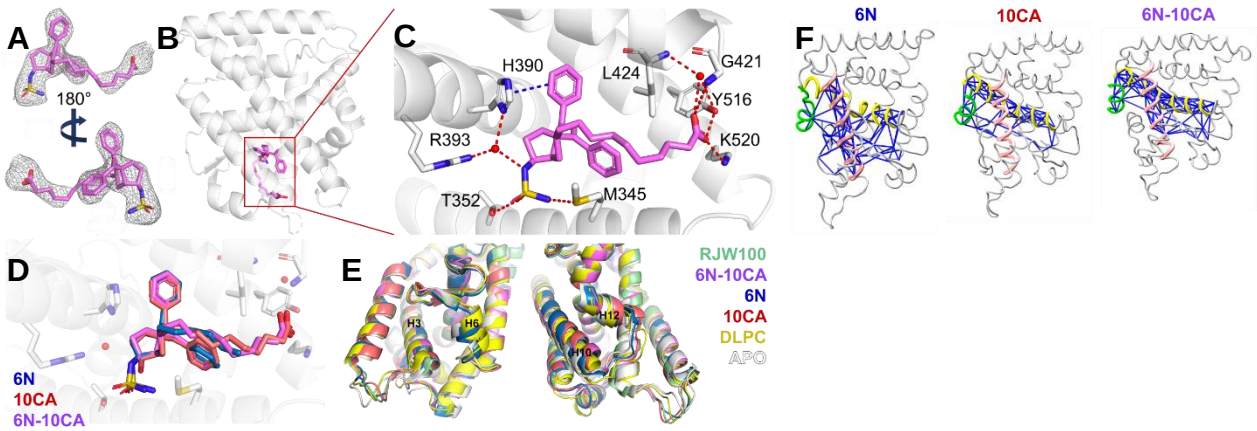

Figure 3.9 LRH-1 LBD structure and dynamics.

A. Ligand F_O-F_C omit map showing electron density for 6N-10CA contoured at 2.5σ. **B.** Co-crystal structure of 6N-10CA bound to the LRH-1 LBD (PDB XXXX). **C.** 6N-10CA binding mode with sidechains of engaged residues shown as sticks (C=purple, O=red, N=blue, S=yellow), water molecules are shown as spheres, and bonds are represented as dotted lines (red=hydrogen, blue= π–π stacking). **D.** Overlay of 6N, 10CA, and 6N-10CA. **E.** Structural comparison of LRH-1 LBD bound to RJW100 (green, PDB 5L11), 6N-10CA (purple), 6N (blue, PDB 6OQY), 10CA (red, unpublished), DLPC (yellow, PDB 4DOS), and unbound to ligand (white, PDB 4PLD). **F.** Pathway analysis of MD simulation of LRH-1 LBD bound to 6N, 10CA, and 6N-10CA showing communication between AF-B and AFS (pink = H3, yellow = H4/H5, green = Tif2 coactivator peptide).

To explore the mechanism of 6N-10CA-mediated activation and the molecular basis for differential LRH-1 signaling of different agonist classes, we first solved the crystal structure of this small molecule bound to the LRH-1 LBD (Figure 3.9). We observed clear electron density for each region of the small molecule, including the bicyclic core, sulfamide head group, and nearly the entire carboxylate tail (Figure 3.9A). As seen with 6N and 10CA (Figure 3.6), there was hydrogen bond contact with residue side chains of Y516 and K520 at the pocket mouth (10CA) and M345 and T352 deep within the pocket (6N) (Figure 3.9 B, C). Additionally, there is both π–π stacking and an indirect hydrogen bond contact with H390 through a conserved water molecule seen in previous structures (Figure 3.6). Overlaying 6N-10CA with 6N and 10CA reveals a nearly identical binding pose, further demonstrating that polar contacts anchor bicyclic compounds in a predictable orientation in the pocket (Figure 3.9 D). Structural comparison with the LBD of previous structures led to some interesting observations (Figure 3.9 E). Notably, the overall protein structure is highly similar between the 6N-10CA and 10CA complexes, with nearly complete overlap at the pocket mouth (H3 and H10), which is highly responsive to ligand binding, and the H10-loop-H12 region. Interestingly, while there is very strong overlap with the LRH-1 LBD bound to synthetic agonists RJW100 and 6N at the pocket mouth, this region differs substantially in DLPC-bound and apo structures. Additionally, the H10-loop-H12 region varies substantially between structures, suggesting that distinct ligand contacts promote different activation states at the AFS and that carboxylate-containing compounds confer a similar conformation at this region. Overall, the crystal structure shows that 6N-10CA effectively contacts both sets of polar residues in the pocket and that ligand identity confers different conformational states in key regions of the receptor that are conserved between 6N-10CA and 10CA.

To compare agonist-driven communication pathways between allosterically-linked sites on LRH-1, we conducted 1 μs MD simulations and performed a suboptimal paths analysis.15 This analysis identifies chains of residues with the strongest patterns of correlated motion, as measured by cartesian covariance, predicting the strongest communication paths between two sites on the receptor. These paths are thought to convey the most information between the sites, facilitating allosteric communication.[67,68] We obtained the strongest 1000 suboptimal paths connecting the AF-B, a region of the receptor consisting of the β-sheet-H6 which communicates ligand binding status to the AFS,8 and Tif2 coactivator in LRH-1 complexes with and 6N, 10CA, and 6N-10CA. Paths in LRH1-10CA traverse H4/H5 to reach the AFS surface, while 6N preferentially induces communication through H3. 6N-10CA induces communication between both H4/H5 (~70%) and H3 (~30%), indicating that correlated motions are induced along both pathways, in contrast to the more directionally restrictive pathways observed in 6N and 10CA (Figure 3.9 E). We also obtained the 1000 strongest paths connecting the ligand and bound Tif2 peptide which contains an LXXLL (X = any amino acid) motif that engages with the AFS of the LBD. While 6N and 6N-10CA induce communication directly between H3 and Tif2, 10CA relies heavily on induced communication between H3->H12->peptide and H5->peptide, with only a small fraction (2%) of paths directly linking H3 with Tif2 peptide. This trend can likely be attributed to the ability of 6N and 6N-10CA ligands, by virtue of the sulfamide, to directly contact H3, enhancing correlated motion. Overall,

---

[67] Vanwart AT, Eargle J, Luthey-Schulten Z, Amaro RE. Exploring residue component contributions to dynamical network models of allostery. J Chem Theory Comput. 2012;8(8):2949-61. Epub 2012/11/10. doi: 10.1021/ct300377a. PubMed PMID: 23139645; PMCID: PMC3489502

[68] Gasper PM, Fuglestad B, Komives EA, Markwick PR, McCammon JA. Allosteric networks in thrombin distinguish procoagulant vs. anticoagulant activities. Proc Natl Acad Sci U S A. 2012;109(52):21216-22. Epub 2012/12/01. doi: 10.1073/pnas.1218414109. PubMed PMID: 23197839; PMCID: PMC3535651.

the MD simulations reveal that the sulfamide strongly drives communication from the ligand directly, but that communication with the AF-B is strongly influenced by the carboxylate tail. Because of the important role of the AF-B in LRH-1 signaling, the different allostery driven by 6N and 6N-10CA may be responsible for the distinct signaling patterns seen in receptor signaling in HepG2 cells.

One of the most characteristic features of agonizing NR ligands is their ability to promote interaction with coactivator proteins. LRH-1 is responsive to activating molecules, showing improved affinity for coactivators when bound to activating PLs or synthetic agonists[61]. We therefore sought to explore how contacting different lipophilic sites in the LBP affects recruitment of LXXLL motif-containing peptides of coregulator proteins established to regulate LRH-1 activity: steroid receptor coactivator-3 (SRC-3), peroxisome proliferator-activated receptor gamma coactivator 1-α (PGC-1α), and small heterodimer partner (SHP). Each peptide was responsive to agonist binding, with PGC-1α binding representing the most responsive interaction (Fig. 5A). 6N and 10CA drove a 3-fold, 4-fold, and 2-fold increase in affinity for SRC-3, PGC-1α, and SHP, respectively. 6N-10CA binding promoted a similar affinity for SRC-3 and an enhanced affinity for PGC-1α and SHP (10-fold and 4-fold over vehicle control, respectively) (Fig. 5A). Because PGC-1α was the most responsive coactivator peptide to small molecule binding, we ran MD simulations (3 x 1 μs each) on the LRH-1 LBD bound to RJW100, 6N, 10CA, and 6N-10CA to explore the dynamics and allostery responsible for differential ligand responsiveness to this peptide. RMSF analysis for the complexes revealed the most variation in the AF-B region of the receptor, suggesting that this region of the receptor is responsive to different classes of LRH-1 agonists (Figure 3.10 B). Pathway analysis revealed that 6N-10CA promotes much stronger

communication between the AF-B and both H12 and the PGC-1α peptide (Figure 3.10 C). Interestingly, RJW100 communicated entirely through H3, while 6N, 10CA, and 6N-10CA each used paths traversing H3 and H4/H5. However, inclusion of the carboxylate tail strongly diverts paths from

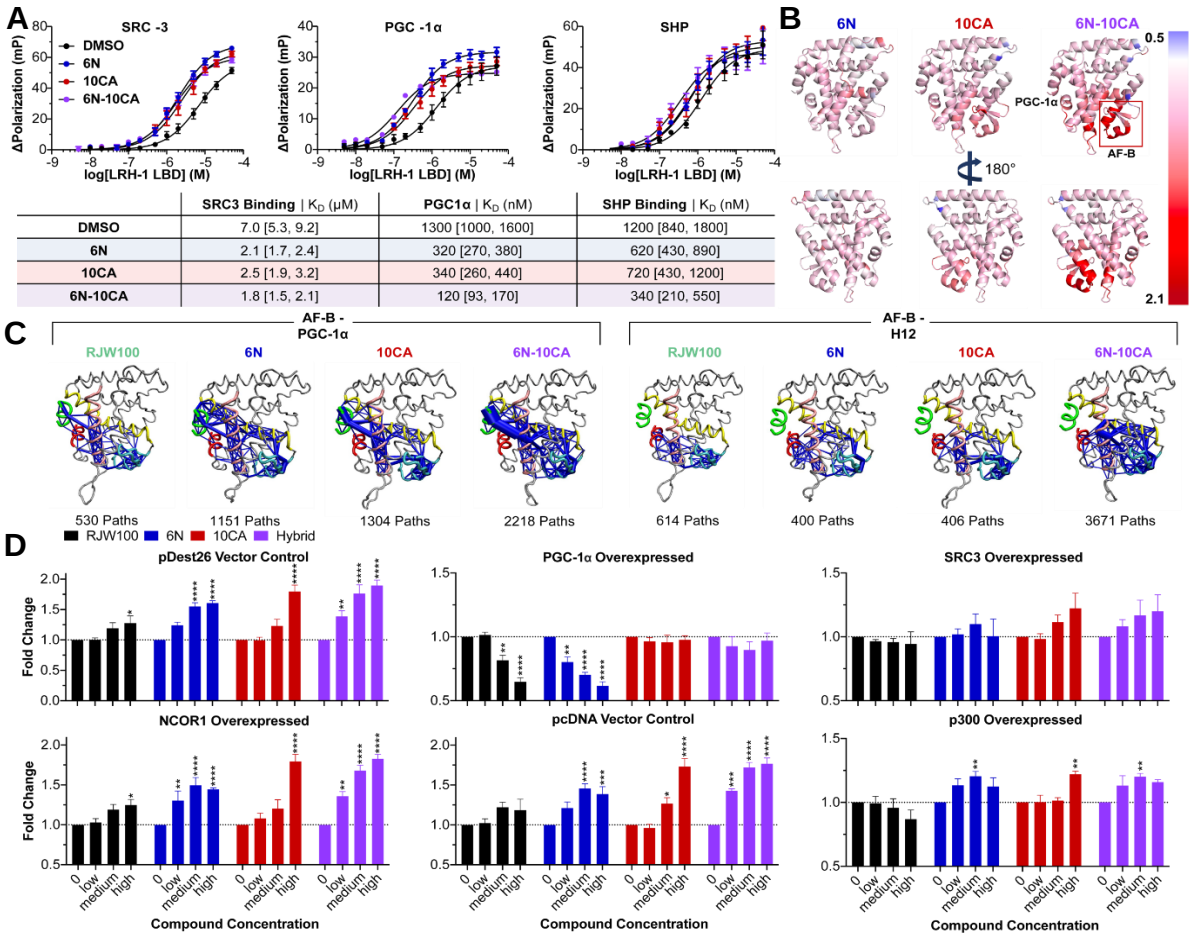

	SRC3 Binding | K_D (μM)	PGC1α | K_D (nM)	SHP Binding | K_D (nM)
DMSO	7.0 [5.3, 9.2]	1300 [1000, 1600]	1200 [840, 1800]
6N	2.1 [1.7, 2.4]	320 [270, 380]	620 [430, 890]
10CA	2.5 [1.9, 3.2]	340 [260, 440]	720 [430, 1200]
6N-10CA	1.8 [1.5, 2.1]	120 [93, 170]	340 [210, 550]

Figure 3.10 Differential modulation of coregulator preference by LRH-1 synthetic agonists.

A. LRH-1 LBD peptide binding assay. Binding affinities shown with 95% confidence intervals shown in brackets. Data shown as mean ± SEM from four independent experiments. **B.** RMSF analysis of MDS of LRH-1 LBD bound to synthetic ligands shown and fragment of PGC-1α. Values shown are derived from RMSF values normalized to values from MDS of LRH-1 LBD complexed with RJW100 as a reference. The AF-B and peptide fragment of PGC-1α are indicated. **C.** Pathway analysis of MD simulation of LRH-1 LBD bound to RJW100, 6N, 10CA, and 6N-10CA showing communication between the AF-B and AFS as well as between the AF-B and H12 (pink = H3, yellow = H4/H5, green = PGC-1α coactivator peptide, teal = AF-B, red = H12). **D.** Luciferase reporter assays with LRH-1 and indicated coregulator overexpressed. pDest26 is the vector control for PGC-1α, SRC3, and NCOR1, while pcDNA is the vector control for p300. Data shown as mean ± SEM from four biological replicates. One-way ANOVA and Bonferroni Multiple Comparisons Test, *p < 0.05, **p < 0.01, ***p < 0.001, ****p < 0.0001

H4/H5 to H3, as 10CA and 6N-10CA had substantially more communication through H4/H5 than 6N (Figure 3.10C). While the opposite was seen for Tif2 (Figure 3.9 F), the divergence in paths between these helices remains driven by the presence or absence of a carboxylate tail, indicating that carboxylate contacts at the pocket mouth drives different allostery in the LBD. Therefore, while improved binding is modest, 6N-10CA consistently promoted the highest affinity for each peptide and drove the strongest communication with the AFS when the PGC-1α peptide is bound to the receptor. This suggests that engagement with both hydrophilic sites in the LBP has an additive effect in driving an active conformation at the AFS and that certain coactivators may be more responsive to different ligand classes than others.

Recent work has shown that engagement between LRH-1 and coregulators involved residues found outside of the LBD. To investigate whether small molecules differentially modulate full-length coregulator interaction, we again used the luciferase reporter assay, but overexpressed coactivators SRC-3, PGC-1α, p300, as well as corepressor NCOR1. While the typical setup is highly dependent upon the native pool of coregulators in the cell line, overexpression of one coregulator enables us to see how a small molecule modulates LRH-1 activity where one coregulator is dominant. Each coregulator modulated LRH-1 as expected, with coactivators SRC-3, PGC-1α, p300 increasing activity and NCOR1 decreasing activity, relative to the vector control. Vector controls showed a consistent trend, with 6N and 6N-10CA displaying the greatest potency and 10CA and 6N-10CA exhibiting the greatest efficacy (Figure 3.10 D). However, LRH-1 activity changed drastically depending upon which coregulator was overexpressed in the cell (Figure 3.10 D). Overexpression of SRC3 and NCOR1 led to similar trends as vector controls. However, when PGC-1α is overexpressed, there is a dose-dependent decrease in receptor activity upon addition of RJW100 and 6N, and no response to carboxylate-containing 10CA and 6N-10CA.

Interestingly, when p300 is overexpressed, LRH-1 is unresponsive to RJW100 but remains responsive to 6N, 10CA, and 6N-10CA. This is the first strong evidence that full-length interactions between LRH-1 and coregulator proteins is differentially responsive to activating small molecules that make different contacts in the pocket. Importantly, this also suggests that certain classes of LRH-1 synthetic ligands act as inverse agonists when certain coregulators are dominant in the cell.

3.5 Conclusion

LRH-1 is a key regulator of many metabolic pathways in lipid biosynthesis and reverse cholesterol transport. However, it has also been implicated as a driver in many types of cancer. Agonizing LRH-1 systemically in an attempt to ameliorate symptoms related to cardiovascular disease may drive oncogenic behavior in other tissues. Building on our previous agonist development, we have combined features previously identified as crucial for LRH-1 activation and tight LRH-1 binding. Building from 6N, where the sulfamide driven water network is crucial for low nanomolar binding, we synthesized a derivative that also incorporated the carboxylate containing ten carbon tail; a moiety previously shown to activate LRH-1 and induce expression of CYP7A1, the rate limiting enzyme for bile acid synthesis. Mechanistically, in contrast to 6N which communicates with the AF-B primarily through helix 3, the hybrid compound 6N-10CA communicates through helix 3 as well as through the residues at the mouth of the binding pocket (analogous to 10CA). 6N-10CA retains the coactivator recruitment and gene expression profile of 10CA and native ligand DLPC, but with the potency of 6N. The differential coactivator recruitment is potentially sparing of oncogenic activity of LRH-1, and supports further study as a therapeutic in inflammatory and cardiovascular diseases.

3.6 Supporting Information

3.6.1 Chemistry

General Information

All reactions were carried out in oven-dried glassware, equipped with a stir bar and under a nitrogen atmosphere with dry solvents under anhydrous conditions, unless otherwise noted. Solvents used in anhydrous reactions were purified by passing over activated alumina and storing under argon. Yields refer to chromatographically and spectroscopically (1H NMR) homogenous materials, unless otherwise stated. Reagents were purchased at the highest commercial quality and used without further purification, unless otherwise stated. n-Butyllithium (n-BuLi) was used as a 1.6 M or a 2.5 M solution in hexanes (Aldrich), was stored at 4°C and titrated prior to use. Organic solutions were concentrated under reduced pressure on a rotary evaporator using a water bath. Chromatographic purification of products was accomplished using forced-flow chromatography on 230-400 mesh silica gel. Preparative thin-layer chromatography (PTLC) separations were carried out on 1000μm SiliCycle silica gel F-254 plates. Thin-layer chromatography (TLC) was performed on 250μm SiliCycle silica gel F-254 plates. Visualization of the developed chromatogram was performed by fluorescence quenching or by staining using KMnO4, p-anisaldehyde, or ninhydrin stains.

1H and 13C NMR spectra were obtained from the Emory University NMR facility and recorded on a Bruker Avance III HD 600 equipped with cryo-probe (600 MHz), INOVA 600 (600 MHz), INOVA 500 (500 MHz), INOVA 400 (400 MHz), VNMR 400 (400 MHz), or Mercury 300 (300 MHz), and are internally referenced to residual protio solvent signals. Data for 1H NMR are reported as follows: chemical shift (ppm), multiplicity (s = singlet, d = doublet, t = triplet, q = quartet, m = multiplet, dd = doublet of doublets, dt = doublet of triplets, ddd= doublet of doublet

of doublets, dtd= doublet of triplet of doublets, b = broad, etc.), coupling constant (Hz), integration, and assignment, when applicable. Data for decoupled 13C NMR are reported in terms of chemical shift and multiplicity when applicable. Gas Chromatography Mass Spectrometry (GC-MS) was performed on an Agilent 5977A mass spectrometer with an Agilent 7890A gas chromatography inlet. Liquid Chromatography Mass Spectrometry (LC-MS) was performed on an Agilent 6120 mass spectrometer with an Agilent 1220 Infinity liquid chromatography inlet. Preparative High-Pressure Liquid chromatography (Prep-HPLC) was performed on an Agilent 1200 Infinity Series chromatograph using an Agilent Prep-C18 30 x 250 mm 10 μm column, or an Agilent Prep-C18 21.2 x 100 mm, 5 μm column.

Evaluation of Purity

Purity of all tested compounds was determined by HPLC analysis, using the methods given below (as indicated for each compound).

Method A: A linear gradient using water and 0.1 % formic acid (FA) (Solvent A) and MeCN and 0.1% FA (Solvent B); t = 0 min, 30% B, t = 4 min, 99% B (held for 1 min), then 50% B for 1 min, was employed on an Agilent Poroshell 120 EC-C18 2.7 micron, 3.0 mm x 50 mm column (flow rate 1 mL/min) or an Agilent Zorbax SB-C18 1.8 micron, 2.1 mm x 50 mm column (flow rate 0.8 mL/min). The UV detection was set to 254 nm. The LC column was maintained at ambient temperature.

Method B: A linear gradient using water and 0.1 % formic acid (FA) (Solvent A) and MeCN and 0.1% FA (Solvent B); t = 0 min, 70% B, t = 4 min, 99% B (held for 1 min), then 50% B for 1 min, was employed on an Agilent Poroshell 120 EC-C18 2.7 micron, 3.0 mm x 50 mm column (flow rate 1 mL/min) or an Agilent Zorbax SB-C18 1.8 micron, 2.1 mm x 50 mm column (flow

rate 0.8 mL/min). The UV detection was set to 254 nm. The LC column was maintained at ambient temperature.

Method C: A linear gradient using water and 0.1 % formic acid (FA) (Solvent A) and MeCN and 0.1% FA (Solvent B); t = 0 min, 5% B, t = 6 min, 95% B (held for 2 min), then 5% B for 1 min, was employed on an Agilent Poroshell 120 EC-C18 2.7 micron, 3.0 mm x 50 mm column (flow rate 1 mL/min) or an Agilent Zorbax SB-C18 1.8 micron, 2.1 mm x 50 mm column (flow rate 0.8 mL/min). The UV detection was set to 254 nm. The LC column was maintained at ambient temperature.

Chemical Synthesis

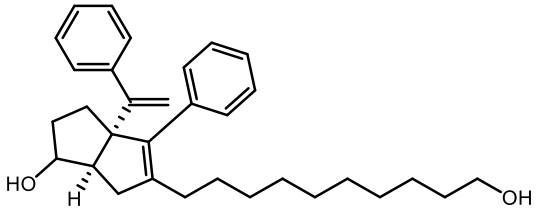

5-(10-hydroxydecyl)-4-phenyl-3a-(1-phenylvinyl)-1,2,3,3a,6,6a-hexahydropentalen-1-ol (3): A slight modification of the procedure of Flynn et al. was used. Prior to use in the reaction, all reagents were dried by azeotropic removal of water using benzene. A dry round bottom flask containing bis(cyclopentadienyl)zirconium(IV) dichloride (1.403 g, 4.8 mmol, 1.2 equiv) under nitrogen, was dissolved in anhydrous, degassed tetrahydrofuran (THF, 5 mL/mmol enyne) and cooled to -78 °C. The resulting solution was treated with *n*-BuLi (3.84 mL, 9.6 mmol, 2.4 equiv.) and the light yellow solution was stirred for 50 minutes. A solution of **tert-butyldimethyl((7-phenylhept-1-en-6-yn-3-yl)oxy)silane** (1.202 g, 4.0 mmol, 1.0 equiv) in anhydrous, degassed THF (5 mL/mmol) was added. The resulting salmon-colored mixture was stirred at -78 °C for 45 minutes, the cooling bath removed, and the reaction mixture was allowed to warm to ambient

temperature with stirring (2.5 hours total). The reaction mixture was then cooled to -78 °C for 15 minutes and **tert-butyl((10,10-dibromodecyl)oxy)diphenylsilane** (2.492 g, 4.4 mmol, 1.1 equiv) was added as a solution in anhydrous THF (5 mL/mmol) followed by freshly prepared lithium diisopropylamide (LDA, 4.4 mL, 4.4 mmol, 1.0 M, 1.1 equiv.). After 30 minutes, a freshly prepared solution of lithium phenylacetylide (14.4 mmol, 3.6 equiv.) in anhydrous THF (2 mL/mmol) was added dropwise and the resulting rust-colored solution was stirred at -78 °C for 1 hour. The reaction was quenched with methanol and saturated aqueous sodium bicarbonate and allowed to warm to room temperature, affording a light yellow slurry that stirred overnight. The slurry was then poured onto water and extracted with ethyl acetate four times. The combined organic layers were washed with brine, dried with Na_2SO_4, filtered, and concentrated *in vacuo* to afford a crude mixture. The resulting crude mixture was dissolved in 200 mL of 1:1 DCM:MeOH in a round bottom flask then 0.5 mL of concentrated HCl added. The resulting solution was stirred at room temperature for 2.5 hours before concentrating *in vacuo* and subjecting to silica gel chromatography (5-50% EtOAc/hexanes eluent) to afford the title compound as a yellow oil and 1.7:1 mixture of diastereomers used in the next step without separation. (1.47 g, 80% over 2 steps).

Exo diastereomer: **^{1}H NMR** (600 MHz, $CDCl_3$) δ 7.37 – 7.23 (m, 8H), 7.20 (t, *J* = 8.0 Hz, 2H), 5.07 (d, *J* = 1.4 Hz, 1H), 4.99 (d, *J* = 1.4 Hz, 1H), 3.96 – 3.93 (m, 1H), 3.64 (t, *J* = 6.6 Hz, 2H), 2.36 (dd, *J* = 16.9, 9.3 Hz, 1H), 2.29 (dd, *J* = 9.3, 1.8 Hz, 1H), 2.13 – 1.98 (m, 4H), 1.75 – 1.63 (m, 2H), 1.56 (p, *J* = 6.8 Hz, 3H), 1.43 – 1.17 (m, 14H).

Endo diastereomer: **^{1}H NMR** (600 MHz, $CDCl_3$) δ 7.37 – 7.23 (m, 8H), 7.20 (t, *J* = 7.5 Hz, 2H), 5.07 (d, *J* = 1.4 Hz, 1H), 4.93 (d, *J* = 1.4 Hz, 1H), 4.18 (td, *J* = 8.9, 5.6, 1H), 3.64 (t, *J* = 6.6 Hz,

2H), 2.62 (dd, *J* = 17.5, 2.1 Hz, 1H), 2.48 (td, *J* = 8.7, 2.0 Hz, 1H), 2.13 – 1.98 (m, 4H), 1.84 (dq, *J* = 10.0, 4.9 Hz, 1H), 1.75 – 1.63 (m, 2H), 1.56 (p, *J* = 6.8 Hz, 2H), 1.43 – 1.17 (m, 14H).

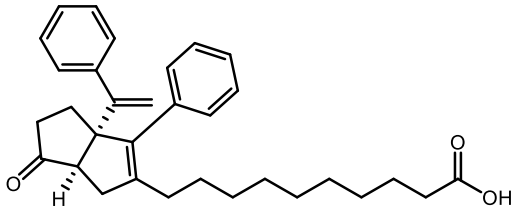

10-(-6-oxo-3-phenyl-3a-(1-phenylvinyl)-1,3a,4,5,6,6a-hexahydropentalen-2-yl)decanoic acid (4): To a solution of **3** in acetonitrile (592 mg, 1.3 mmol, 0.1 M) was added tetrapropylammonium perruthenate (45.3 mg, 0.13 mmol, 0.1 equiv.), *N*-methylmorpholine *N*-oxide (2.29 g, 12.9 mmol, 10 equiv.), and water (0.24 mL, 12.9 mmol, 10 equiv.) and stirred at room temperature overnight. The reaction solution was then filtered through a pad of silica with 99:1 EtOAc:AcOH to collect the title compound as a yellow oil (608 mg, quant.).

^{1}H NMR (500 MHz, $CDCl_3$) δ 7.40 – 7.19 (m, 10H), 5.22 (d, *J* = 1.5 Hz, 1H), 5.11 (d, *J* = 1.4 Hz, 1H), 2.46 (d, *J* = 7.8 Hz, 1H), 2.36 – 2.26 (m, 4H), 2.16 – 1.95 (m, 5H), 1.91 (dd, *J* = 16.5, 7.8 Hz, 1H), 1.61 (p, *J* = 7.5 Hz, 2H), 1.46 – 0.97 (m, 12H). Carboxylic acid proton (-COO**H**) not observed.

^{13}C NMR (126 MHz, $CDCl_3$) δ 223.0, 179.9, 153.3, 145.0, 142.6, 137.5, 136.8, 129.1, 128.4, 128.2, 127.7, 127.2, 127.1, 115.4, 65.6, 55.7, 38.9, 37.6, 34.2, 30.1, 29.8, 29.4, 29.3, 29.1, 28.5, 27.7, 24.8.

HPLC method A, **LRMS** (ESI, APCI) *m/z*: calc'd for $C_{32}H_{39}O_3$ $(M+H)^+$ 471.3, found 470.8.

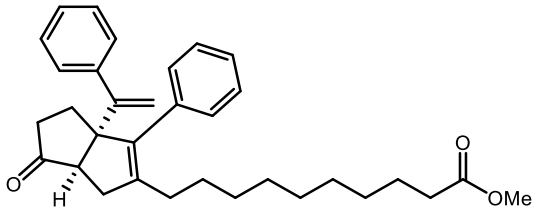

methyl 10-(6-oxo-3-phenyl-3a-(1-phenylvinyl)-1,3a,4,5,6,6a-hexahydropentalen-2-yl)decanoate (5): To a solution of **4** in methanol (945 mg, 2 mmol, 0.1 M) was added 5 drops of concentrated HCl and stirred at room temperature overnight. Reaction solution was then concentrated *in vacuo* and filtered through a pad of silica to collect the title compound as a yellow oil (930 mg, 96%).

^{1}H NMR (500 MHz, $CDCl_3$) δ 7.40 – 7.19 (m, 10H), 5.22 (d, *J* = 1.3 Hz, 1H), 5.11 (d, *J* = 1.3 Hz, 1H), 3.66 (s, 3H), 2.46 (d, *J* = 7.7 Hz, 1H), 2.34 – 2.25 (m, 4H), 2.16 – 1.95 (m, 5H), 1.91 (dd, *J* = 16.5, 7.8 Hz, 1H), 1.60 (p, *J* = 7.5 Hz, 2H), 1.33 – 1.10 (m, 12H).

^{13}C NMR (126 MHz, $CDCl_3$) δ 222.7, 174.4, 153.3, 144.9, 142.6, 137.5, 136.7, 129.0, 128.3, 128.2, 127.7, 127.1, 127.1, 115.3, 65.5, 55.6, 51.5, 38.8, 37.6, 34.2, 30.0, 29.7, 29.4, 29.33, 29.27, 29.2, 28.4, 27.7, 25.0.

HPLC method A, **LRMS** (ESI, APCI) *m/z*: calc'd for $C_{33}H_{41}O_3$ $(M+H)^+$ 485.3, found 484.9.

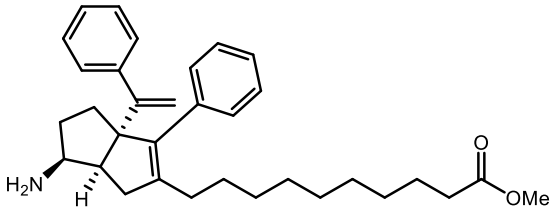

methyl 10-(6-amino-3-phenyl-3a-(1-phenylvinyl)-1,3a,4,5,6,6a-hexahydropentalen-2-yl)decanoate (6): To a screw top test tube charged with a stir bar was added **5** (350 mg, 0.72 mmol, 1.0 equiv.) and ethanol (3 mL) and sealed. Ammonia (7 M in methanol, 0.52 mL, 3.61

mmol, 5.0 equiv.) then titanium(IV) isopropoxide (0.33 mL, 1.08 mmol, 1.5 equiv.) were added via syringe and stirred at room temperature for 6 hours. The test tube cap was then removed and sodium borohydride (82 mg, 2.16 mmol, 3 equiv.) added portion-wise. The resulting solution was stirred at room temperature overnight before being quenched with EtOAc, saturated aqueous potassium sodium tartrate, and 2 M aqueous sodium hydroxide. The resulting slurry was then sonicated in the reaction tube for 10 minutes before adding to a separatory funnel. The aqueous layer was then drained and remaining EtOAc washed with 2 x 20 mL of aqueous potassium sodium tartrate and 2M sodium hydroxide then 20 mL water and 20 mL brine. The remaining organic layer was then dried over Na_2SO_4, filtered, and concentrated *in vacuo* to give the title compound as a yellow oil (283 mg, 81%).

^{1}H NMR (500 MHz, $CDCl_3$) δ 7.35 – 7.22 (m, 8H), 7.20 (t, *J* = 2.0 Hz, 1H), 7.18 (t, *J* = 1.5 Hz, 1H), 5.07 (d, *J* = 1.4 Hz, 1H), 4.93 (d, *J* = 1.5 Hz, 1H), 3.66 (s, 3H), 3.31 (td, *J* = 8.7, 5.8 Hz, 1H), 2.49 – 2.40 (m, 2H), 2.29 (t, *J* = 7.6 Hz, 2H), 2.12 – 2.00 (m, 4H), 1.85 – 1.78 (m, 1H), 1.72 – 1.67 (m, 2H), 1.60 (p, *J* = 7.5 Hz, 2H), 1.42 – 1.15 (m, 12H). Amine protons (-N**H$_2$**) not observed.

^{13}C NMR (126 MHz, $CDCl_3$) δ 174.5, 155.1, 144.3, 143.0, 139.5, 137.2, 129.9, 127.9, 127.8, 127.7, 126.8, 126.7, 115.3, 69.6, 55.3, 51.6, 34.4, 34.3, 33.3, 30.0, 29.9, 29.52, 29.50, 29.4, 29.3, 28.1, 25.1.

HPLC method A, **LRMS** (ESI, APCI) *m/z*: calc'd for $C_{33}H_{44}NO_2$ $(M+H)^+$ 486.3, found 485.8

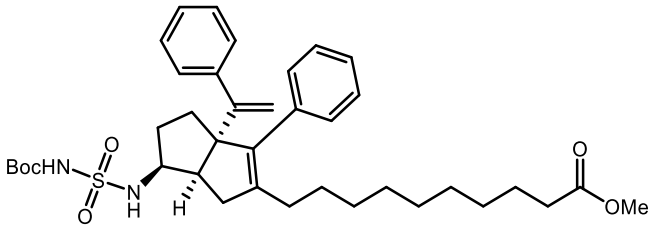

methyl 10-(6-((N-(tert-butoxycarbonyl)sulfamoyl)amino)-3-phenyl-3a-(1-phenylvinyl)-1,3a,4,5,6,6a-hexahydropentalen-2-yl)decanoate (7): To a solution of *tert*-butyl alcohol (47 mg, 0.64 mmol, 1.1 equiv.) in anhydrous DCM (0.6 mL) in an oven-dried flask under nitrogen at 0 °C was added neat chlorosulfonylisocyanate (0.050 mL, 0.58 mmol, 1.0 equiv.) and stirred for 45 minutes, warming to room temperature in that time. The resulting solution was then added via syringe to a solution of **6** (283 mg, 0.58 mmol, 1.0 equiv.) and triethylamine (0.12 mL, 0.87 mmol, 1.5 equiv.) in anhydrous DCM (0.6 mL) under nitrogen in an oven-dried flask at 0 °C. The reaction was then stirred and warmed to room temperature over 3 hours before diluting with DCM and washing with 2 x 10 mL 0.5 M aqueous HCl, 10 mL water and 10 mL brine. The organic layer was then dried over Na_2SO_4, filtered, and concentrated *in vacuo* to give crude material. This material was subjected to silica gel chromatography (10-40% EtOAc/hexanes) to collect material taken crude to the next step.

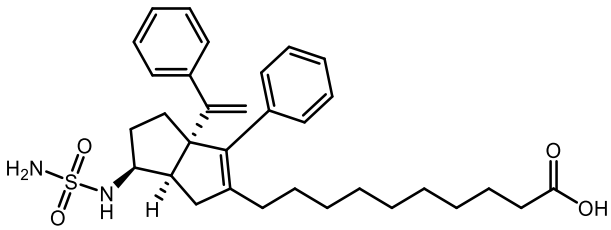

10-(3-phenyl-3a-(1-phenylvinyl)-6-(sulfamoylamino)-1,3a,4,5,6,6a-hexahydropentalen-2-yl)decanoic acid (1): A 20 mL scintillation vial was charged with a stir bar and **7** (160 mg, 0.24 mmol) and cooled to 0 °C. A 3:1 v/v solution of dioxane and concentrated HCl (2 mL) was then

added and allowed to warm to room temperature and stirred for 24 hours before heating to 40 °C for 14 hours. The reaction solution was then diluted with EtOAc and washed with 3 x 5 mL 0.5 M aqueous HCl, 5 ml water, and 5 mL brine. The organic layer was then dried over Na_2SO_4, filtered, and concentrated *in vacuo* to give the title compound as a brown oil (94 mg, 29% over 2 steps).

^{1}H NMR (500 MHz, $CDCl_3$) δ 7.35 – 7.22 (m, 8H), 7.19 (t, *J* = 2.0 Hz, 1H), 7.17 (t, *J* = 1.6 Hz, 1H), 5.10 (d, *J* = 1.3 Hz, 1H), 4.95 (d, *J* = 1.4 Hz, 1H), 4.84 (d, *J* = 7.8 Hz, 1H), 4.72 (s, 2H), 3.78 (dtd, *J* = 11.2, 8.3, 6.0 Hz, 1H), 2.62 (td, *J* = 8.9, 2.1 Hz, 1H), 2.42 (dd, *J* = 17.7, 2.1 Hz, 1H), 2.34 (t, *J* = 7.4 Hz, 2H), 2.16 (dd, *J* = 17.6, 9.0 Hz, 1H), 2.11 – 2.00 (m, 2H), 1.99 – 1.92 (m, 1H), 1.75 – 1.68 (m, 2H), 1.62 (p, *J* = 7.4 Hz, 2H), 1.53 – 1.42 (m, 1H), 1.43 – 1.18 (m, 12H). Carboxylic acid proton (-COO**H**) not observed.

^{13}C NMR (126 MHz, $CDCl_3$) δ 179.3, 154.3, 143.8, 143.01 139.3, 136.8, 129.8, 128.0, 127.8, 127.0, 126.9, 115.7, 68.9, 57.2, 47.5, 35.6, 34.0, 32.6, 31.8, 29.9, 29.7, 29.2, 29.1, 29.0, 28.9, 27.9, 24.6.

HPLC method B, **LRMS** (ESI, APCI) *m/z*: calc'd for $C_{32}H_{43}N_2O_4S$ $(M+H)^+$ 551.3, found 551.8.

3.6.2 Biology

Cell Culture

HeLa cells were cultured in phenol red-free MEMα + 10% fetal bovine serum – Charcoal/Dextran Treated and HepG2 cells were cultured in phenol red-free DMEM + 10% fetal bovine serum. Cell lines were cultured under standard conditions (5% CO2, 37°C). While initial Hoechst staining did not reveal contamination in HepG2 cells used in RNA-seq studies, this cell later tested positive for mycoplasma contamination using the LookOut® Mycoplasma PCR Detection Kit. HeLa cells and

HepG2 cells used for RT-qPCR studies were verified to be mycoplasma free with the LookOut® Mycoplasma PCR Detection Kit.

Protein Expression and Purification

LRH-1 LBD was expressed and purified as described previously.[52,66] Briefly, BL21(DE3) E. coli cells were transformed with human LRH-1 LBD (residues 299-541) with an N-terminal 6xHis tag in a pMCSG7 vector. Bacteria were grown at 37°C in liquid broth (LB) until cells reached OD_{600} 0.6, and protein expression was induced with 1 mM IPTG for 4 hours at 30°C. Cells were centrifuged and stored at -80°C. After one freeze-thaw cycle, the pellet was resuspended in lysis buffer (20 mM Tris-HCl, 150 mM NaCl, 5% glycerol, 25 mM imidazole, 0.2 mM PMSF, DNase, lysozyme, pH 7.4) and lysed via sonication. Lysate was subjected to Ni^{2+} affinity chromatography. To remove co-purified bacterial lipids and to ensure a homogenous complex, LRH-1 LBD was incubated with four-fold molar excess of DLPC for 16 h at 4°C and then purified with size-exclusion chromatography (SEC) into assay buffer (150 mM NaCl, 20 mM Tris-HCl, 5 % glycerol, pH 7.4). Protein used for thermal stability assays was purified in a similar manner but was not complexed with DLPC prior to SEC purification. LRH-1 LBD used for crystallization was incubated with TEV protease to remove the 6xHis tag and subjected to a second round of nickel affinity chromatography. All protein was stored at -80°C until use.

Ligand Binding Assays

Fluorescence polarization competition assays were performed as previously described.[65,66] Briefly, experiments were conducted in black 384-well plates in assay buffer (150 mM NaCl, 20 mM Tris-HCl, 5% glycerol, pH 7.4). 6N conjugated to fluorescein amidite (FAM) (10 nM/well) was

incubated with LRH-1 LBD (5 nM/well). Unlabeled compounds were added at concentrations indicated in figures. Each experiment was performed twice with four technical replicates each. Technical replicates were averaged and normalized independently prior to final data analysis. Using GraphPad Prism (version 9), data were fit to a one-site, fit Ki curve, assuming a final probe concentration of 10 nM and probe affinity of 1 nM.[65] Data was excluded from wells with 1.0 e-6 M 6N-10CA, as the resulting point dropped sharply after ligand saturation, distorting the curve fit.

Reporter Assays

LRH-1 reporter assays were conducted as described previously[65,66]. Briefly, HeLa cells were seeded at 7,500 cells per well in 96-well plates (white-walled, clear bottom). After ~ 24 hours, cells were transfected with LRH-1 (5 ng/well), a reporter plasmid with an LRH-1 response element derived from the SHP promoter cloned upstream of firefly luciferase (50 ng/well), and a plasmid expressing Renilla luciferase constitutively from a CMV promoter (1 ng/well). Cells were transfected with FuGENE at a ratio of 5:1 (FuGENE:DNA). Twenty-four hours after transfection, compounds were diluted in Opti-MEM and introduced to cells at final concentrations indicated in figures (final DMSO concentration was 0.37%). After ~ 24 hours, luciferase signal was measured using the DualGlo kit (Promega). Each experiment was conducted with four biological replicates, each with three technical replicates averaged prior to data analysis. Firefly luciferase signal for each well was divided by the well's Renilla signal intensity and then normalized relative to the DMSO control. Data was analyzed with GraphPad Prism (version 9) using a stimulating dose-response curve (Hill slope = 1). Data was excluded from analysis for cells treated with 3e-5 M of 6N-10CA, as the final signal showed a drastic decrease in overall signal, potentially indicating cell toxicity or compound insolubility near 1e-6 M also observed in the FP assays.

Protein Stability

Thermal stability of the LRH-1 LBD complexed with ligands was determined using a Tycho NT.6 Nanotemper. LRH-1 LBD was incubated with 5-fold molar excess ligand overnight at 4 °C in assay buffer (150 mM NaCl, 20 mM Tris-HCl, 5 % glycerol, pH 7.4). Complexes were centrifuged at high speed for five minutes prior to measurement. Samples were then loaded into capillaries and tryptophan/tyrosine fluorescence was monitored at wavelengths 330 and 350 nm over a 30 °C/min gradient (35°C – 95°C). The melting point (inflection point) was determined with Tycho NT.6 software. Three separate experiments were conducted in triplicate. Technical replicates were averaged, and data was plotted using GraphPad Prism (version 9).

Crystallography and Structure Determination

Complexed LRH-1 LBD crystals were generated as described previously. Briefly, cleaved LRH-1 LBD (6xHis tag removed) was incubated with 6N-10CA at four-fold molar excess overnight at 4°C. The complex was then purified via SEC into crystallization buffer (150 mM NaCl, 100 mM ammonium acetate, 1 mM EDTA, 2 mM CHAPS, 1 mM DTT, pH 7.4) and incubated with a peptide corresponding to human TIF-2 NR box 3 (NH3-KENALLRYLLDKDD-CO2) at four-fold molar excess for two hours at room temperature. The complex was then concentrated to ~ 5 mg/mL and crystals were generated via hanging drop vapor diffusion in crystallant containing 0.05 M sodium acetate – pH 4.6, 5-11% PEG 4000, and 0-25% glycerol at 4°C. Crystals were then flash frozen in liquid N2 using cryoprotectant consisting of crystallant supplemented with 30% glycerol. Data was collected remotely from the Southeast Regional Collaborative Access Team (SER-CAT) at the Advanced Photon Source (Argonne National Laboratories, Chicago, IL). Data were

processed using HKL2000 and phased with molecular replacement, using PDB 5L11 as the search model. Structure refinement was performed with Phenix and Coot (REFs), with additional refinement and assessment accomplished with PDB-REDO (ref). During refinement, residues 527-529 were removed due to poor electron density. Final figures were constructed with PyMOL (Schrodinger, LLC).

Peptide Binding

Coregulator peptide binding assays were performed as previously noted. Briefly, LRH-1 LBD was incubated with compounds (4-fold molar excess) or an equal volume of DMSO overnight at 4°C. Complexes were centrifuged at high speed for five minutes prior to assay setup. Complexes were serially diluted in assay buffer (150 mM NaCl, 20 mM Tris-HCl, 5 % glycerol, pH 7.4) in black 384-well plates. FAM-labeled coregulator peptides were added to a final concentration of 50 nM. After an overnight incubation at 4°C, fluorescence polarization was measured on a BioTek Neo plate reader. Sequences of peptides used were as follows: SRC-3 NR box 3, 1H3N-PVSPKKKENALLRYLLDKDDT-CO2; PGC-1α NR box 2, 1H3N-EEPSLLKKLLLAPA-CO2; SHP NR box 1, 1H3N-QGAASRPAILYALLSSSLK-CO2. Assays were performed in triplicate four times. Data were combined and fit to a one-site equilibrium binding equation with GraphPad Prism (version 9).

Molecular Dynamics Simulations

Molecular dynamics simulations were performed on three complexes: i) LRH1-Tif2-10CA ii) LRH1-Tif2-6N iii) LRH1-Tif2-hybrid. The complexes were solvated in an octahedral box of TIP3P water with a 10 Å buffer around the protein complex. Na+ and Cl− ions were added to

neutralize the protein and achieve physiological buffer conditions. All systems were set up using the xleap tool in AmberTools18 of Amber 2018[69] with the ff14SB forcefield.[70] Parameters for the agonist ligands 10CA, 6N and 6N-10CA were obtained using Antechamber[71] in AmberTools18. All minimizations and simulations were performed with Amber18 (also part of Amber 2018). For minimization, 5000 steps of steepest descent were used, followed by 5000 steps of conjugate gradient minimization. Minimizations were first performed with 500 kcal/mol·Å2 restraints on all protein and ligand atoms. Restraints were then removed on all except the ligand and Tif2 peptides, and the protocol was repeated. Restraints were subsequently lowered to 100 kcal/mol· Å2 and then finally removed from all atoms for two final rounds of minimization. Minimized systems were heated from 0 to 300 K with a 100-ps MD run, constant volume periodic boundaries and 5 kcal/mol·Å2 restraints on all protein and ligand atoms. A 12-ns equilibration was performed for all complexes with 10 kcal/mol·Å2 restraints on the Tif2 peptide and ligand atoms using the NPT ensemble. Restraints were reduced to 1 kcal/mol·Å2 and 10 ns of additional equilibration performed. Finally, production trajectories of 1000 ns were obtained for unrestrained complexes

---

[69] Case DA IYB-S, Brozell SR, Cerutti DS, Cheatham TE III, Cruzeiro WD V., Darden TA,; Duke, RE GM, Gohlke H, Goetz AW, Greene D, Harris R, Homeyer N, Huang Y,; Izadi S, A. K.,, Kurtzman T LT, LeGrand S, Li P, Lin C, Liu J, Luchko T, Luo R, Mermelstein DJ, M. M. K,, Miao Y MG, Nguyen C, Nguyen H, Omelyan I, Onufriev A, Pan F, Qi R, R. R. D, Roitberg, A SC, Schott-Verdugo S, Shen J, Simmerling CL, Smith J, SalomonFerrer R, Swails J,, Walker RC WJ, Wei H, Wolf RM, Wu X, Xiao L, York DMand Kollman PA, AMBER 2018,, University of California SF.

[70] Maier JA, Martinez C, Kasavajhala K, Wickstrom L, Hauser KE, Simmerling C. ff14SB: Improving the Accuracy of Protein Side Chain and Backbone Parameters from ff99SB. J Chem Theory Comput. 2015;11(8):3696-713. Epub 2015/11/18. doi: 10.1021/acs.jctc.5b00255. PubMed PMID: 26574453; PMCID: PMC4821407

[71] Wang JM, Wang W, Kollman PA. Antechamber: An accessory software package for molecular mechanical calculations. Abstracts of Papers of the American Chemical Society. 2001;222:U403-U. PubMed PMID: WOS:000170690002032.

in the NPT ensemble. All bonds between heavy atoms and hydrogens were fixed with the SHAKE algorithm.[72] A cutoff distance of 10 Å was used to evaluate long-range electrostatics with particle mesh Ewald and for van der Waals forces. Structural averaging was performed using the CPPTRAJ[73] module of AmberTools. Dynamic networks were constructed from each 1000-ns trajectory using the NetworkView plugin[74] in VMD[75] and the Carma program.[76] Networks are constructed by defining all protein C-α atoms as nodes, using Cartesian covariance (calculated in Carma) to measure communication within the network. Pairs of nodes that reside within a 4.5 Å cutoff for 75% of the simulation are connected via an edge. Edge weights are inversely proportional to the covariance between the nodes. Suboptimal paths between the Tif2 peptide and both the ligand LBP and AF-B sites were identified using the Floyd−Warshall algorithm.[77]

---

[72] Ryckaert J-P, Ciccotti G, Berendsen HJC. Numerical integration of the cartesian equations of motion of a system with constraints: molecular dynamics of n-alkanes. Journal of Computational Physics. 1977;23(3):327-41. doi: 10.1016/0021-9991(77)90098-5.

[73] Roe DR, Cheatham TE, 3rd. PTRAJ and CPPTRAJ: Software for Processing and Analysis of Molecular Dynamics Trajectory Data. J Chem Theory Comput. 2013;9(7):3084-95. Epub 2013/07/09. doi: 10.1021/ct400341p. PubMed PMID: 26583988.

[74] Sethi A, Eargle J, Black AA, Luthey-Schulten Z. Dynamical networks in tRNA:protein complexes. Proc Natl Acad Sci U S A. 2009;106(16):6620-5. Epub 2009/04/09. doi: 10.1073/pnas.0810961106. PubMed PMID: 19351898; PMCID: PMC2672494.

[75] Humphrey W, Dalke A, Schulten K. VMD: Visual molecular dynamics. Journal of Molecular Graphics. 1996;14(1):33-8. doi: 10.1016/0263-7855(96)00018-5.

[76] Glykos NM. Software news and updates. Carma: a molecular dynamics analysis program. J Comput Chem. 2006;27(14):1765-8. Epub 2006/08/19. doi: 10.1002/jcc.20482. PubMed PMID: 16917862.

[77] Floyd RW. Algorithm 97: Shortest path. Communications of the ACM. 1962;5(6). doi: 10.1145/367766.368168.

Chapter 4:

Lead Optimization of a Potent LRH-1 Agonist

Racheal Spurlin also synthesized and characterized some of the compounds described herein. Cato Lee performed biochemical assays related to potency and ran the molecular dynamics simulations. Solubility, permeability, and metabolic stability assays in addition to pharmacokinetic measurements were performed at Pharmaron. Prof. John Calvert and Cato Lee performed the target engagement studies.

Abstract: Liver receptor homolog-1 (LRH-1) is an orphan nuclear receptor that regulates expression of enzymes in bile acid biosynthesis, lipid homeostasis, and cholesterol transport. Therapeutic modulation of these pathways through LRH-1 agonism is an attractive tactic for reducing the burden of cardiovascular diseases, the leading cause of death worldwide. The native ligands for LRH-1 are phospholipids, compounds not suited for clinical administration due to poor pharmacokinetics, polypharmacology, and low potency. Thus, there has been a great deal of interest in synthetic agonists for LRH-1. Early drug discovery efforts focusing on the hexahydropentalene scaffold generated highly potent compounds, however none possessed properties required for therapeutic use; some compounds were chemically unstable, and most were extremely hydrophobic. Herein we disclose the design and synthesis of an LRH-1 agonist that possesses a clinically relevant pharmacokinetic profile and strong modulation of disease-relevant genes in vivo.

4.1 Introduction

Cardiovascular and metabolic disease is the leading cause of death worldwide and continues to increase, with death rates approximately doubling since 1990.[78,79] While lifestyle factors contribute significantly to one's risk of developing cardiovascular disease, there remains unmet need for pharmacological interventions.

Liver receptor homolog 1 (LRH-1, NR5A2) is an orphan nuclear receptor that regulates gene expression of key proteins involved in cholesterol homeostasis, lipogenesis, and bile acid synthesis. Thus, it is an attractive target for modulating several pathways implicated in cardiovascular disease. Early attempts at developing agonists for LRH-1 generated compounds poorly suited for administration as a therapeutic; some compounds were chemically unstable[80],

[78] Roth, G. A. et al. Global, regional, and national burden of cardiovascular diseases for 10 causes, 1990 to 2015. *J. Am. Coll. Cardiol.* **70**, 1–25 (2017).

[79] A, R. G., A, M. G., O, J. C., Giovanni, A., Enrico, A., M, B. L., C, B. N., Z, B. A., J, B. E., P, B. C., Aimé, B., Michael, B., Marianne, B., J, C. T., Jonathan, C., L, C. A., S, C. S., T, C. L., Josef, C., … Valentin, F. (2020). Global Burden of Cardiovascular Diseases and Risk Factors, 1990–2019. *Journal of the American College of Cardiology*, *76*(25), 2982–3021. https://doi.org/10.1016/j.jacc.2020.11.010

[80] Whitby, R. J., Dixon, S., Maloney, P. R., Delerive, P., Goodwin, B. J., Parks, D. J., & Willson, T. M. (2006). Identification of small molecule agonists of the orphan nuclear receptors liver receptor homolog-1 and steroidogenic factor-1. *Journal of Medicinal Chemistry*, *49*(23), 6652–6655. https://doi.org/10.1021/jm060990k

and most were extremely hydrophobic[81,82]. We sought to address these pitfalls by developing an LRH-1 agonist that was highly potent, soluble, and chemically and metabolically stable. A compound with these properties would have the potential to make meaningful progress towards therapeutic intervention in cardiovascular diseases through LRH-1 agonism.

4.2 ADME Properties in Drug Development

As a compound is developed further and is used in more complex models of the human disease, properties beyond potency become important to manage. Biological systems have evolved to prevent systemic exposure to chemical compounds not produced by that organism (xenobiotics)[83]. The first defense against foreign chemicals is the gut. The gastrointestinal tract is lined with epithelial cells with cell membranes that prevent most chemical compounds from coming through. These cells have transporter proteins that selectively shuttle chemicals like amino acids, nuceleobases, and fatty acids through but keep most other chemicals out[84]. However, compounds that are moderately hydrophobic and uncharged are able to diffuse into the apical lipid

[81] Whitby, R. J., Stec, J., Blind, R. D., Dixon, S., Leesnitzer, L. M., Orband-Miller, L. A., Williams, S. P., Willson, T. M., Xu, R., Zuercher, W. J., Cai, F., & Ingraham, H. A. (2011). Small molecule agonists of the orphan nuclear receptors steroidogenic factor-1 (SF-1, NR5A1) and liver receptor homologue-1 (LRH-1, NR5A2). *Journal of Medicinal Chemistry*, *54*(7), 2266–2281. https://doi.org/10.1021/jm1014296

[82] Mays, S. G., Flynn, A. R., Cornelison, J. L., Okafor, C. D., Wang, H., Wang, G., Huang, X., Donaldson, H. N., Millings, E. J., Polavarapu, R., Moore, D. D., Calvert, J. W., Jui, N. T., & Ortlund, E. A. (2019). Development of the First Low Nanomolar Liver Receptor Homolog-1 Agonist through Structure-guided Design. *Journal of Medicinal Chemistry*, *62*(24), 11022–11034. https://doi.org/10.1021/acs.jmedchem.9b00753

[83] Caldwell, J., Gardner, I., & Swales, N. (n.d.). An Introduction to Drug Disposition: The Basic Principles of Absorption, Distribution, Metabolism, and Excretion*.

[84] Shugarts S, Benet LZ. The role of transporters in the pharmacokinetics of orally administered drugs. Pharm Res. 2009;26(9):2039-2054. doi:10.1007/s11095-009-9924-0

bilayer of the cell membrane, through the cytoplasm and then diffuse out through the basolateral lipid bilayer, resulting in the drug entering the blood stream. Optimizing the compound's structure to be just the right amount of hydrophobic and hydrophilic is a substantial challenge in drug development[85].

Furthermore, the blood is passed through the liver which produces an abundance of oxidative enzymes known as cytochrome P450s. This family of enzymes contains a heme core and utilizes highly reactive hydroxide radical to oxidize and polyhydroxylate xenobiotic compounds[86]. The liver also contains enzymes that conjugate glucuronic acid to xenobiotics; glucuronic acid is an extremely hydrophilic sugar molecule[87]. Both the oxidative metabolism and the conjugative metabolism serve to make xenobiotic compounds more water soluble so that they can be excreted by the kidneys.

[85] Papich, M. G., & Martinez, M. N. (2015). Applying Biopharmaceutical Classification System (BCS) Criteria to Predict Oral Absorption of Drugs in Dogs: Challenges and Pitfalls. AAPS Journal, 17(4), 948–964. https://doi.org/10.1208/s12248-015-9743-7

[86] Lynch, T., & Price, A. (2007). The Effect of Cytochrome P450 Metabolism on Drug Response, Interactions, and Adverse Effects. www.aafp.org/afp.

[87] Yang G, Ge S, Singh R, Basu S, Shatzer K, Zen M, Liu J, Tu Y, Zhang C, Wei J, Shi J, Zhu L, Liu Z, Wang Y, Gao S, Hu M. Glucuronidation: driving factors and their impact on glucuronide disposition. Drug Metab Rev. 2017 May;49(2):105-138. doi: 10.1080/03602532.2017.1293682.

4.3 Design

In order to further develop the lead compound 6N-10CA that we had previously disclosed, we sought to improve its physiochemical properties. In the 1990s, Christopher Lipinski, a chemist at Pfizer, published an analysis of compounds that succeeded in clinical trials and compared them against those that failed[88]. This analysis demonstrated trends in the success of compounds that can be mapped back to their physiochemical properties. These properties can be reasoned to impact the absorption, distribution, metabolism, and excretion of the compound and serve as easy-to-measure surrogates for more complicated ADME behavior. The trends, termed "Lipinski's Rules", include compound molecular weight (<500 daltons), hydrogen bond acceptors (<10), hydrogen bond donors (<5) and cLogP (<5). In his analysis he showed that compounds which break none or one of the rules tend to be more successful in *in-vivo* experiments and ultimately clinical trials (Figure

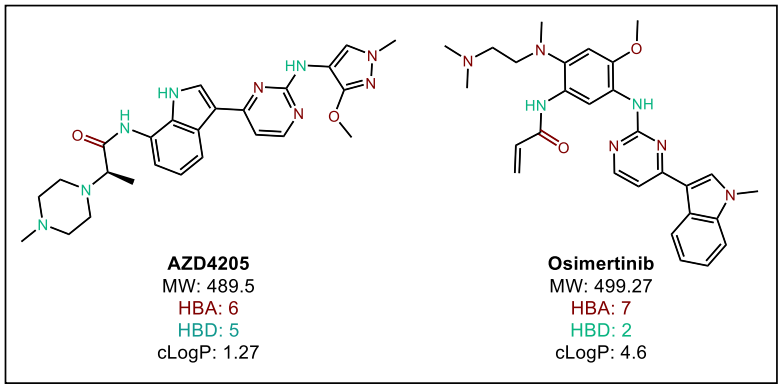

Figure 4.1 FDA approved compounds following Lipinski's Rules

[88] Lipinski, C. A., Dominy, B. W., & Feeney, P. J. (1997). Experimental and computational approaches to estimate solubility and permeability in drug discovery and development settings. In Advanced Drug Delivery Reviews (Vol. 23).

4.1). Following in his mold, there have been many other analyses and metrics produced with differing levels of predictive accuracy[89,90,91].

The lead compound of our LRH-1 agonist program (6N-10CA) is within Lipinski's Rules except in one important area—cLogP. A compound's LogP is the logarithmic value of the partition coefficient when the compound is dissolved in octanol and water[92]. This is a measure of how hydrophobic or hydrophilic the compound is. While LogP is measured, cLogP is calculated and there are many software programs that have been developed to do this, using different "training sets" of compounds from which to build the model[93]. A high LogP, indicating the compound is

[89] Wager, T. T., Hou, X., Verhoest, P. R., & Villalobos, A. (2016). Central Nervous System Multiparameter Optimization Desirability: Application in Drug Discovery. *ACS Chemical Neuroscience*, *7*(6), 767–775. https://doi.org/10.1021/acschemneuro.6b00029

[90] Johnson, T. W., Gallego, R. A., & Edwards, M. P. (2018). Lipophilic Efficiency as an Important Metric in Drug Design. *Journal of Medicinal Chemistry*, *61*(15), 6401–6420. https://doi.org/10.1021/acs.jmedchem.8b00077

[91] Meanwell, N. A. (2016). Improving Drug Design: An Update on Recent Applications of Efficiency Metrics, Strategies for Replacing Problematic Elements, and Compounds in Nontraditional Drug Space. In *Chemical Research in Toxicology* (Vol. 29, Issue 4, pp. 564–616). American Chemical Society. https://doi.org/10.1021/acs.chemrestox.6b00043

[92] Bharate SS, Kumar V, Vishwakarma RA. Determining Partition Coefficient (Log P), Distribution Coefficient (Log D) and Ionization Constant (pKa) in Early Drug Discovery. Comb Chem High Throughput Screen. 2016;19(6):461-9. doi: 10.2174/1386207319666160502123917.

[93] MORIGUCHI, I., HIRONO, S., NAKAGOME, I., & HIRANO, H. (1994). Comparison of Reliability of log P Values for Drugs Calculated by Several Methods. *CHEMICAL & PHARMACEUTICAL BULLETIN*, *42*(4), 976–978. https://doi.org/10.1248/cpb.42.976

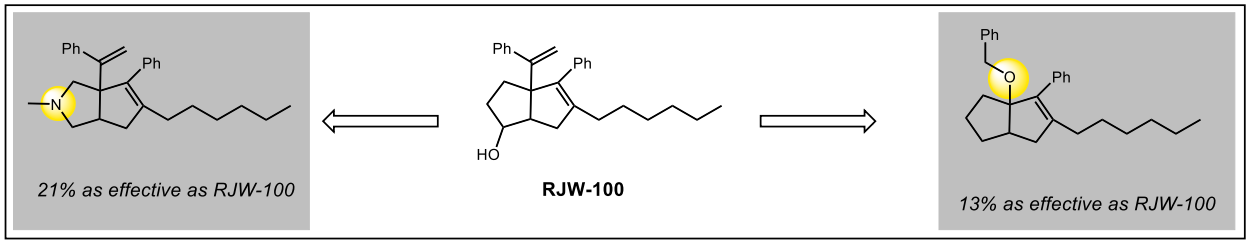

Figure 4.2 Whitby's polar modifications to the bicyclo[3,3,3]-oct-2-ene core were deleterious to potency and efficacy

extremely hydrophobic, has several important implications about how the compound will behave in biological systems. Notably, compounds that have high LogP tend to be poorly soluble, have high hepatic clearance, poorly selective and possess off-target toxicity. The lead compound 6N-10CA has an extremely high cLogP (7.5), and 10CA had high hepatic clearance. We hypothesized that decreasing the compound's LogP we would be able to mitigate some of these issues.

Because the syn-bicyclo[3,3,3]-oct-2-ene scaffold is key to binding, and Whitby et al had described significant loss in potency when incorporating heteroatoms into various parts of the core structure[94] (Figure 4.2) we were reluctant to make any modifications. However, we had already shown during the 10CA optimization that the key binding elements for the tail portion are the polar residues that sit at the mouth of the pocket, and the identity of the lipid-like tail itself may not be as crucial[95]. Thus we sought to increase polar residues in this portion of the molecule to decrease the cLogP. Our initial strategy, outlined in Figure 4.3, was to replace methylenes in the tail with ethers. Because the binding pocket that evolved to bind ligands is extremely nonpolar, any

[94] Whitby, R. J., Stec, J., Blind, R. D., Dixon, S., Leesnitzer, L. M., Orband-Miller, L. A., Williams, S. P., Willson, T. M., Xu, R., Zuercher, W. J., Cai, F., & Ingraham, H. A. (2011). Small molecule agonists of the orphan nuclear receptors steroidogenic factor-1 (SF-1, NR5A1) and liver receptor homologue-1 (LRH-1, NR5A2). *Journal of Medicinal Chemistry*, *54*(7), 2266–2281. https://doi.org/10.1021/jm1014296

[95] Flynn, A. R., Mays, S. G., Ortlund, E. A., & Jui, N. T. (2018). Development of Hybrid Phospholipid Mimics as Effective Agonists for Liver Receptor Homologue-1. *ACS Medicinal Chemistry Letters*, *9*(10), 1051–1056. https://doi.org/10.1021/acsmedchemlett.8b00361

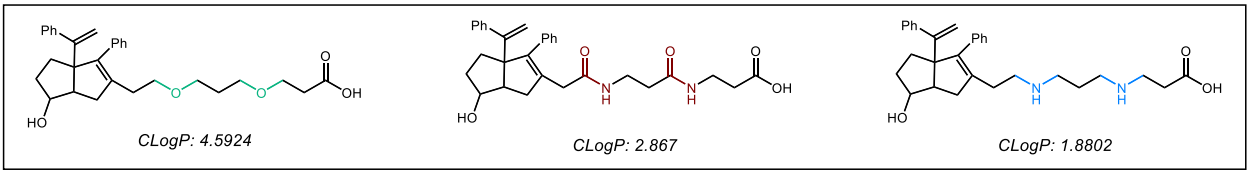

Figure 4.3 Potential modifications to the tail to improve aqueous solubility

protonated or partially charged species in the ligand would be potentially deleterious to binding affinity. We hypothesized that ethers would avoid those charged interactions, while still adding polarity for water solubility.

Furthermore, we sought to improve the hepatic clearance of the compound as the half-life of 6N-10CA was not predicted to provide the biological effect desired. To do this, we evaluated *in silico* the metabolic hot spots for the compound. Routinely, the pendant styrene was identified as the greatest liability[96]. Styrenes are part of a class of functional groups known as structural alerts, or groups with an established poor metabolism profile (Figure 4.4).[97] Recently, industrial groups have worked to better define the moieties in compounds that are likely to generate toxicological issue and eliminate them from compounds earlier on in the design and development process. Olefins are frequently sites of oxidative metabolism,

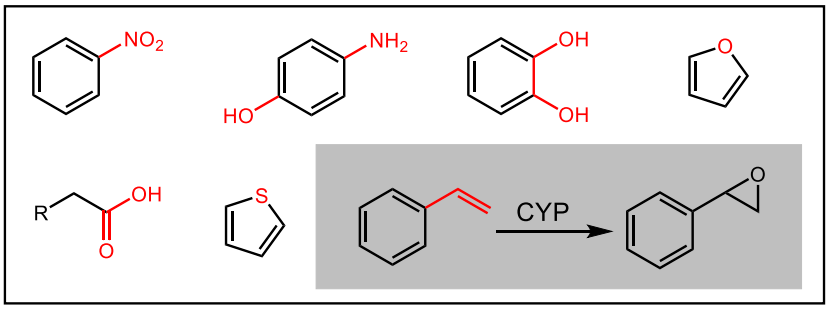

Figure 4.4 Structural alerts and styrene metabolism

[96] Vodicka, P., Koskinen, M., Naccarati, A., Oesch-Bartlomowicz, B., Vodickova, L., Hemminki, K., & Oesch, F. (2006). Styrene metabolism, genotoxicity, and potential carcinogenicity. *Drug Metabolism Reviews*, *38*(4), 805–853. https://doi.org/10.1080/03602530600952222

[97] Kalgutkar, A. S. (2020). Designing around Structural Alerts in Drug Discovery. In *Journal of Medicinal Chemistry* (Vol. 63, Issue 12, pp. 6276–6302). American Chemical Society. https://doi.org/10.1021/acs.jmedchem.9b00917

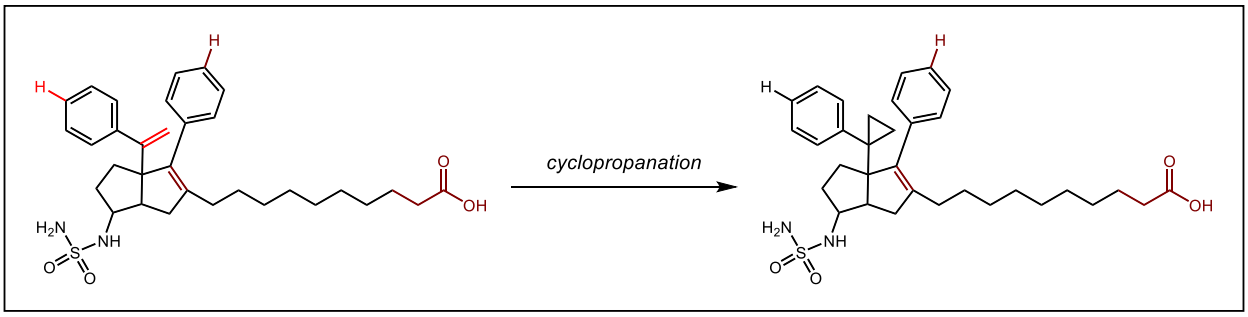

Figure 4.5 Cyclopropanation of pendant styrene to block metabolism

and styrenes are a particularly reactive class of olefin. To lower the hepatic clearance rate, we hypothesized that we could use the styrene as a synthetic intermediate; leveraging its high intrinsic reactivity to alter it into a less reactive species. One way to achieve that goal would be to simply reduce it to the alkane. However, a derivative of 6N had been synthesized with the fully saturated ethylbenzene substituent and the compound lost a significant amount of binding affinity. Another option that we considered was cyclopropanation of the olefin. This work is well precedented and would not only remove the metabolic liability but also create a new region for SAR exploration (Figure 4.5).[98]

A third area of focus was altering the attachment point for the tail (Figure 4.6). Using computational modeling, we examined the binding mode of these compounds and discovered that the alkyl tail could potentially be linked to one of the phenyl rings while still maintaining the same interactions. This would alter the components for the cyclization, where dichloromethane would be used as a carbene precursor. Whitby had utilized this previously but in diminished yield[99].

---

[98] Chanthamath, S., & Iwasa, S. (2016). Enantioselective Cyclopropanation of a Wide Variety of Olefins Catalyzed by Ru(II)-Pheox Complexes. *Accounts of Chemical Research*, *49*(10), 2080–2090. https://doi.org/10.1021/acs.accounts.6b00070

[99] Whitby, R. J., Dixon, S., Maloney, P. R., Delerive, P., Goodwin, B. J., Parks, D. J., & Willson, T. M. (2006). Identification of small molecule agonists of the orphan nuclear receptors liver receptor homolog-1 and steroidogenic factor-1. *Journal of Medicinal Chemistry*, *49*(23), 6652–6655. https://doi.org/10.1021/jm060990k

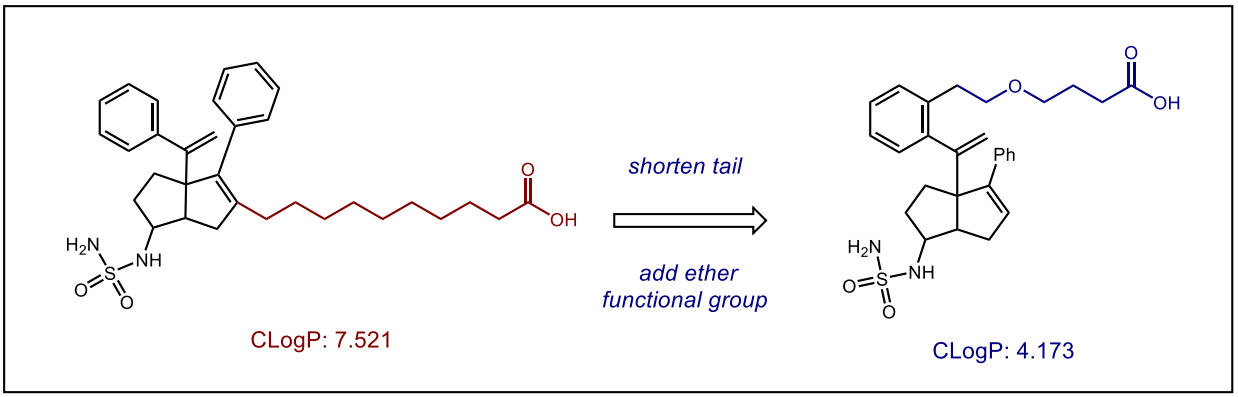

Figure 4.6 Aryl linked tail improves physiochemical properties

4.4 Synthesis

4.4.1 Aryl Linked Tails

Our initial efforts were aimed at synthesis of the aryl linked tail compounds (Scheme 7). As these compounds could be more readily accessible than the ether containing compounds they were prioritized. A synthetic handle on the aryl group was initially envisioned as a protected phenethanol. Starting with bromophenethanol, a protected acetylene unit was coupled on using the palladium catalyzed Sonogashira coupling (94% over two steps). This group was then deprotected under basic conditions to provide the functionalized phenylacetylene (87% yield). Using 3.6 equivalents of this material, the core was constructed using dichloromethane as the carbene precursor to install CH_2 where the tail is normally attached in 41% yield. From here, the phenethanol tail was deprotected to furnish the free alcohol (69%). Next to install the remaining section of the tail, methyl 4 bromobutanoate was added to a solution of the alkoxide to yield the

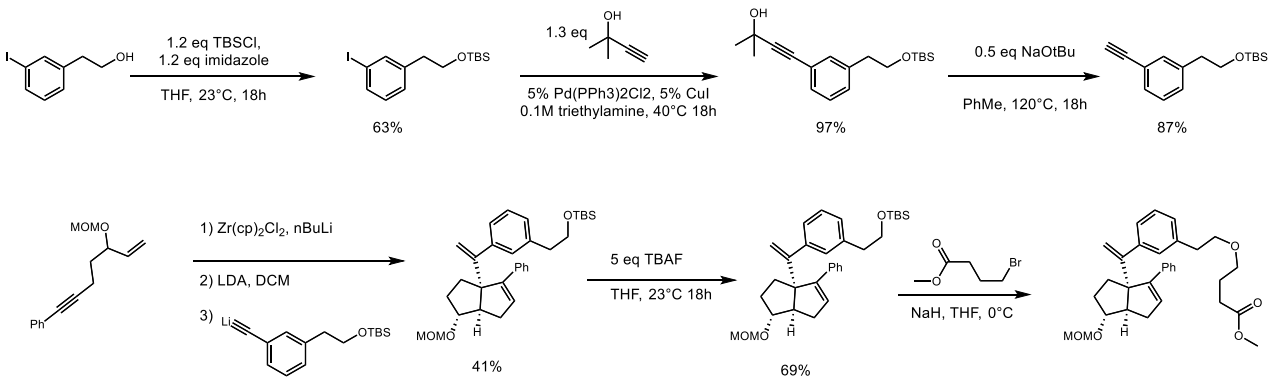

Scheme 7 Synthesis of phenethanol linked tail compound.

methyl protected elaborated tail. However, under the highly basic conditions required for this transformation, degradation of the starting material was observed. To facilitate a milder alkylation, we hypothesized the 1000x more acidic phenol might be an attractive synthetic handle (Scheme 8). The TBS protected tert-butyl(3-ethynylphenoxy)dimethylsilane was synthesized in three analogous steps to the phenethyl derivative (64% over three steps). The material was cyclized, also using dichloromethane as the carbene precursor in 29% yield to provide 426 mg of protected phenol. The protecting group was removed with TBAF and then using potassium carbonate as the base, deprotected and alkylated with ethyl 6-bromobutanoate (27% over two steps). The methoxymethyl protecting group was removed with hydrochloric acid and then the ethyl ester saponified with lithium hydroxide, ultimately synthesizing 1.8 mg of the desired compound for in vitro testing. Unfortunately, the compound was no longer potent; substantial modifications of the core and pendant functional groups have previously been known to be deleterious to potency and this modification met the same fate.

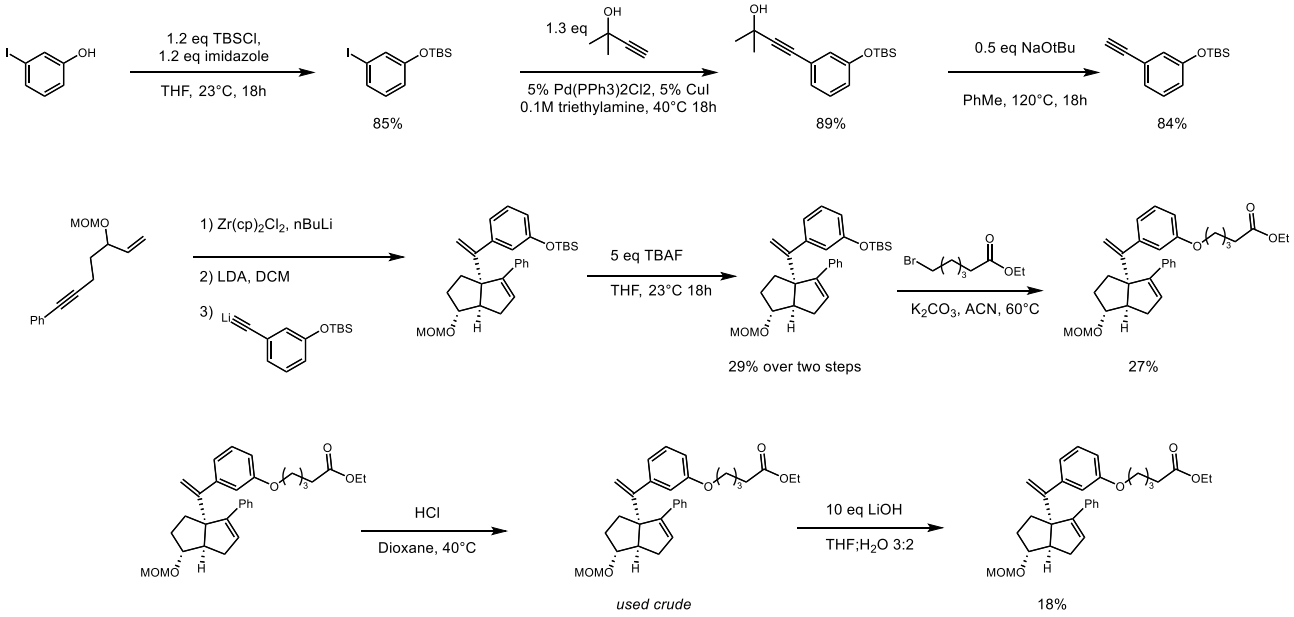

Scheme 8 Synthesis of phenol linked tail compound.

4.4.2 Ether Tails

Next, we turned our attention to the ether containing tail compounds. We outlined a divergent strategy, where one intermediate could be used to access multiple compounds, following the existing synthesis of 6N-10CA (Figure 4.7). We had previously confirmed that silyl protecting groups can be used in the Whitby cyclization and so we planned to synthesize a shorter tail with a protected oxygen, then unmask it and alkylate on different portions that would fill out the required chain length.

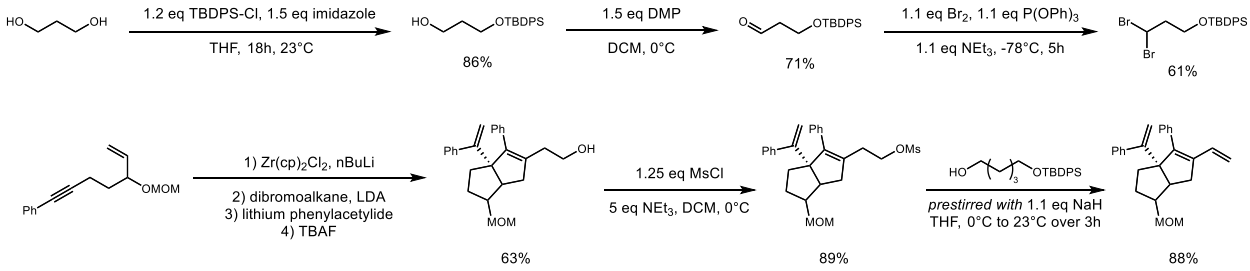

Scheme 9. Synthesis of divergent intermediate for construction of 6N-10CA derivatives with ether containing tails.

Synthesis of the required dibromo compound began with monoprotection of 1,3-propanediol, followed by oxidation and debromination (Scheme 9). Previously, this oxidation had been performed with TCCA and TEMPO, with varying yields. That combination was highly prone to overoxidation and had to be quenched within 5 minutes of the addition of catalyst, commonly providing a mixture of alcohol, aldehyde, and carboxylic acid. To improve the reliability of this transformation, we began to use Dess-Martin Periodinane, which is inexpensively commercially available and unable to oxidize the carbon beyond the aldehyde. This oxidation proceeded quantitatively on gram scale, followed by dibromination with bromine and triphenyl phosphite in 61% yield. This synthesis gave us access to the cyclization precursor on gram scale. Following cyclization and deprotection (62.5% over two steps), various alkylation strategies were attempted.

Reaction of the alcohol with methane sulfonyl chloride and triethylamine furnished the alkyl mesylate in 89%. Using this material, a series of bases, solvents, addition orders, and temperatures was screened. However, a clear reactivity pattern surfaced—even alkoxide nucelophiles were sufficiently basic to facilitate E_2 elimination to the 1-phenyl butadiene (88% isolated yield).

Next, a 5-carbon tail was synthesized (following the synthesis outlined for the 3-carbon tail) and synthetic efforts here focused on using the core as the limiting reagent, given the considerable effort expended in its preparation. Here too, alkylation attempts were largely unfruitful with poor conversion to the desired products (ca. 20%).

Alternate Route to Ether Tail Compounds

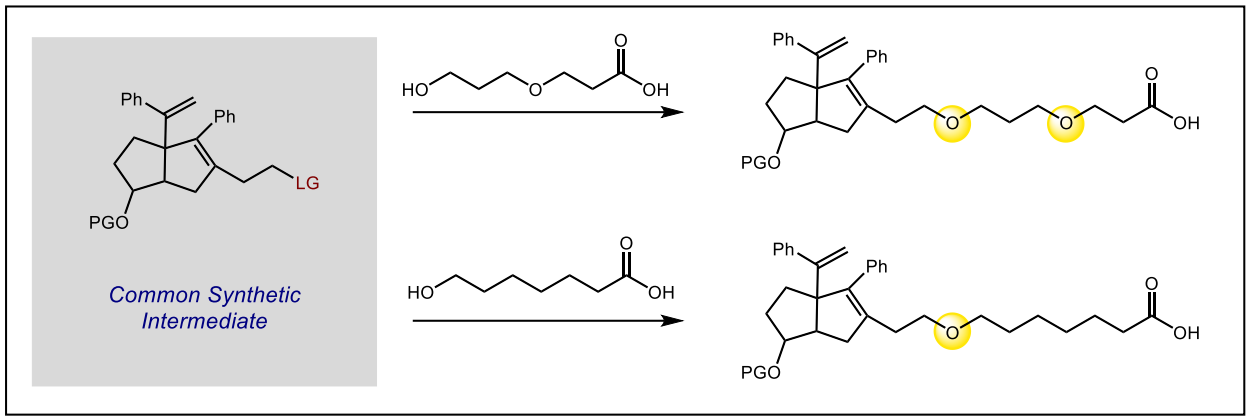

Figure 4.7 Initial divergent synthesis of ether containing tail compounds.

The challenges associated with elaborating the tails from a common post-cyclization intermediate inspired us to proceed with a less divergent route, however one that would reliably access the material required (Figure 4.7). We set out to synthesize the fully elaborated ether containing tails and then cyclize each in turn. Detailed in Scheme 10, this was achieved by monoprotection of pentane diol, followed by alkylation with 6-iodo-hex-1-ene (prepared in one step from the bromide via Finkelstein reaction). The long-chain alkene was subjected to ozone and the resulting ozonide reductively opened to furnish the aldehyde. The ozonide was uncharacteristically stable and was even isolable with the structure confirmed by ^{1}H NMR. Attempts to reduce it with dimethylsulfide across a range of temperatures were unsuccessful. Ultimately triphenylphosphine was proved fruitful and furnished the aldehyde in 76% yield. Dibromination following the typical conditions was then employed however the purification was improved; instead of 100% hexanes, the addition of 5% methyl *tert*-butyl ether more readily separated the desired product from triphenyl phosphate and allowed the average yield of that reaction to double to ca. 80%. This material was then subjected to cyclization and deprotection to provide the fully assembled monoether core in 72% yield.

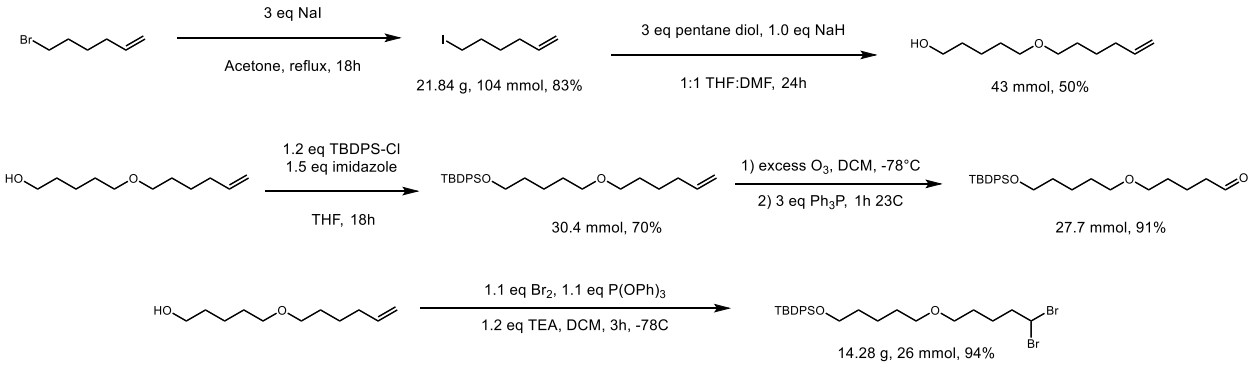

Scheme 10. Synthesis of the monoether dibromo tail

Following a similar synthesis to 6N-10CA, the diol was oxidized to the ketone-acid (58%) and then the carboxylic acid protected as the methyl ester (99%) (Scheme 11). Next, the ketone was reductively aminated utilizing ammonia and titanium^{IV} isopropoxide, furnishing the primary amine in 77% yield. This reaction is extremely sensitive to the quality of titanium catalyst, and efforts were expended to install the amine function prior to the cyclization (vide infra). Following amination, the amine was stirred with sulfamide in alcoholic solvent to install the sulfamide group (74%).

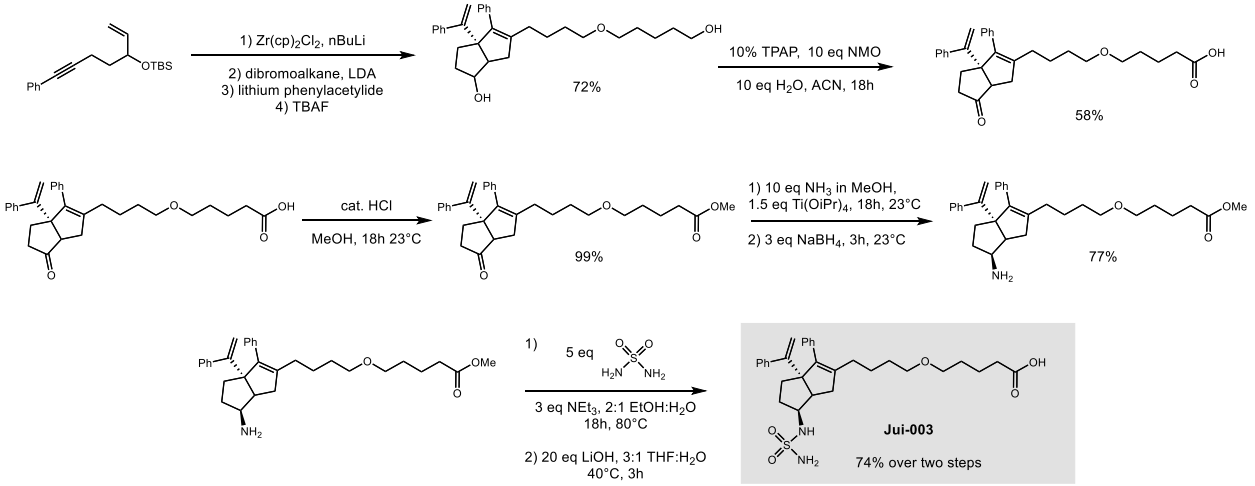

Scheme 11 Elaboration of monoether dibromo tail to Jui-003

We then turned to the synthesis of the diether 6N-10CA compound. To synthesize this compound a key starting material is tripropylene glycol (Scheme 12). While ethylene glycols of

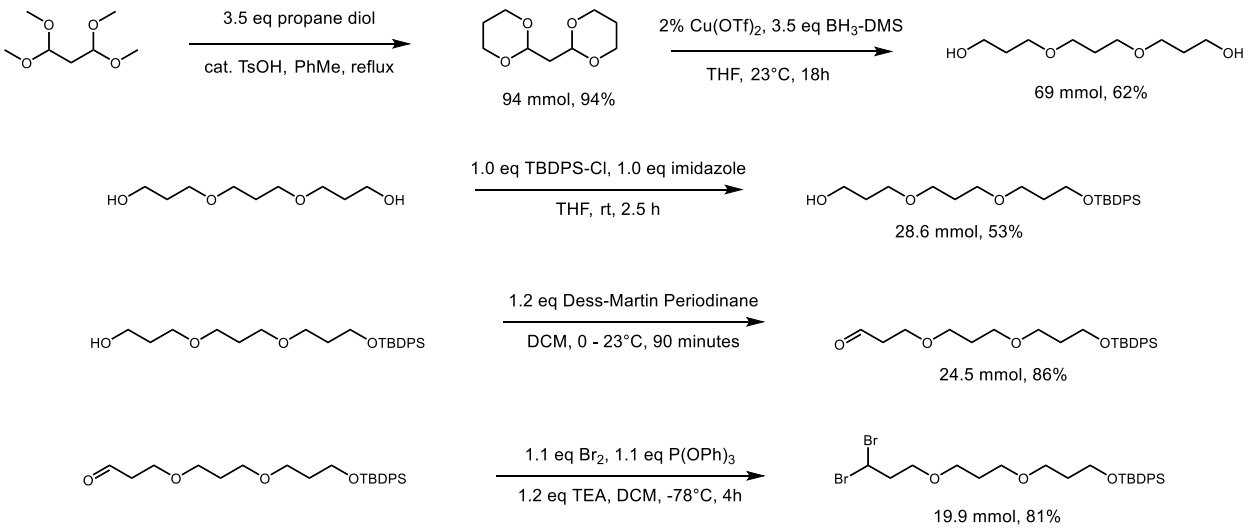

Scheme 12 Synthesis of the diether dibromo tail

various lengths are common and commercially available, there is a dearth of literature surrounding the three carbon analogs. One report from over 50 years ago synthesized the compound by reductively cleaving a cyclic acetal, di(1,3-dioxan-2-yl)methane, with 20 equivalents of borane in refluxing THF for 5 days. While we used this method early to establish proof of concept, some optimization had to be done. After screening a series of Lewis acid catalysts, copper triflate was selected as it provided high yield (82% vs 12% for the literature conditions), overnight reaction time, and room temperature reaction. With ready access to tripropylene glycol, we then protected one of the alcohol groups (53% yield), oxidized it with DMP (86% yield), and dibrominated (78% yield) as was done with previous compounds. It was then cyclized and carried through to the final sulfamide compound (14% over 6 steps, analogous to the synthetic steps for the monoether in Scheme 11).

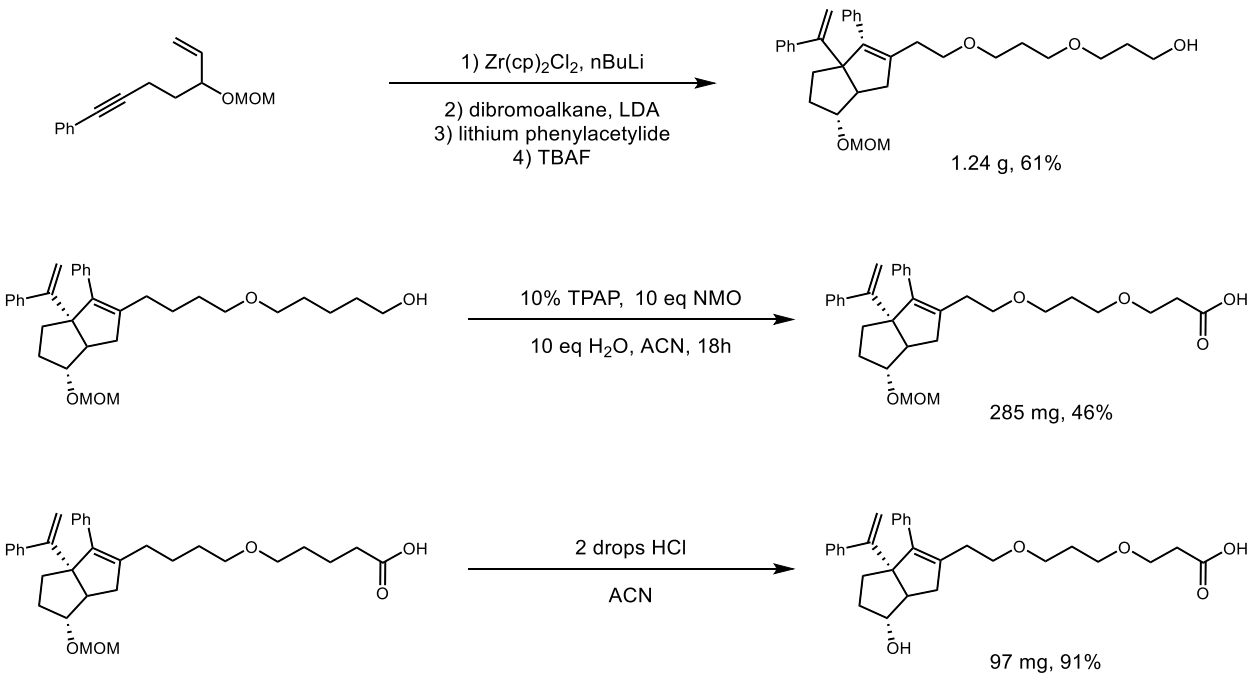

Scheme 13 Synthesis of ether tail 10CA derivatives

For a thorough understanding of the binding properties of the ether tails, we synthesized derivatives of the cyclopentanol compound 10CA using the same ethereal dibromoalkanes, with a representative synthesis shown in Scheme 13. Cyclization of a methoxymethyl protected enyne facilitated selective deprotection of the diol. Oxidation of the free terminal alcohol to the carboxylic acid under Ley-Griffith conditions furnished the acid in moderate yield. Acidic deprotection of the methoxymethyl protecting group revealed the secondary alcohol that is crucial for binding.

After optimization of the route to access the dibromoalkanes, synthesis of the ether tail compounds followed our previous synthetic work in this area. Using these strategies, we ultimately synthesized a small set of compounds that offered the possibility of improved physiochemical properties (FIGURE 4.8).

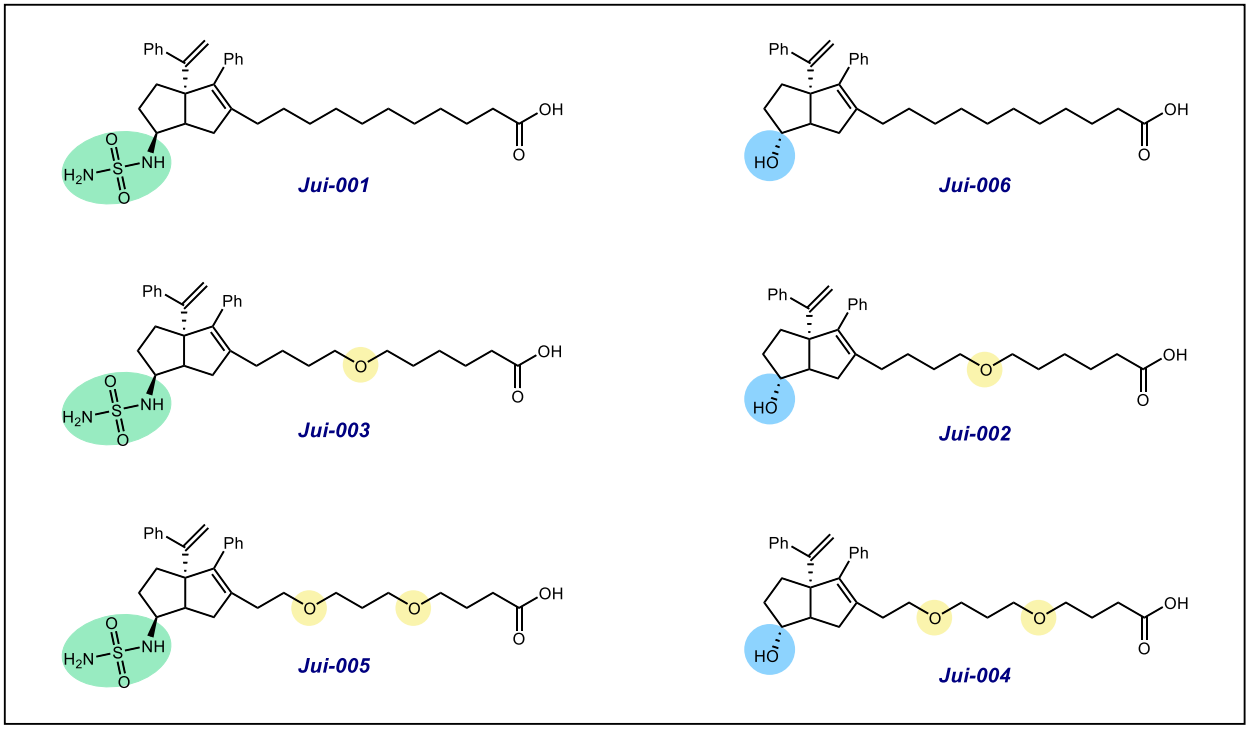

Figure 4.8 Ether tail compounds synthesized for further biologic evaluation

4.5 In-vitro evaluation

4.5.1 LRH-1 Agonism

Although the goal of the design changes was to improve aqueous solubility, optimization of one variable often comes at the expense of another. To that end, we first analyzed the in vitro binding and LRH-1 activation of the molecules we synthesized to ensure the changes did not adversely affect the pharmacological properties. In the case of the molecules with the tail attached to the

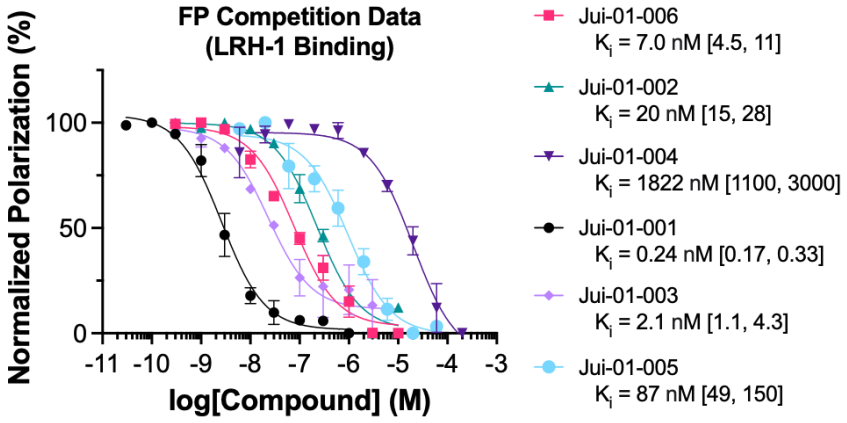

Figure 4.9 LRH-1 *in vitro* binding data for ether tail compounds

pendant arene, the changes destroyed the binding affinity. Altering the attachment point of a crucial binding moiety is a substantial change and the loss of potency was not surprising, if unfortunate. However, when we measured the binding of the monoether and diether tail molecules, we were delighted to observe only a minimal loss in binding affinity and activation. As seen in Figure 4.9, sulfamide containing derivatives in general display higher potency than the alcohol comparators (Jui-003 vs Jui-002 and Jui-005 vs Jui-004). Additional confirmation of the binding affinity can be seen in the thermal shift assay data (Figure 4.10). This assay measures the temperature at which the protein denatures, with tighter binding compounds stabilizing the native protein folding and shifting the melting temperature higher. The pronounced difference between the sulfamide and alcohol compounds is readily apparent and confirms the importance of the headgroup in compound potency.

After the exciting results of cell-free assays, we sought to confirm the activity of these compounds in cell-based assays. The first of which relies on LRH-1 activation to drive expression of a downstream luciferase gene, with higher luciferase expression correlating to higher in vivo target gene expression (Figure 4.11). This assay encouragingly recapitulated the results of the cell-free assays, with the sulfamide containing compounds showing effective LRH-1 activation at the lowest concentrations. Additionally, the alcohol containing compounds (Jui-002, Jui-004, Jui-006) show higher maximum activation

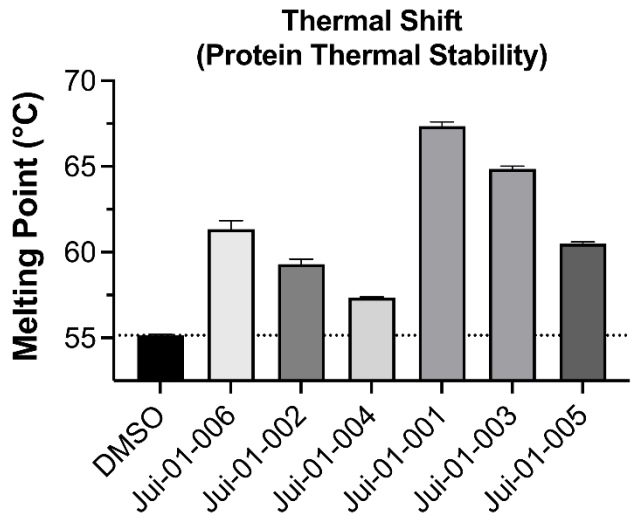

Figure 4.10 LRH-1 thermal stability with ether compounds

(height on the Y axis), however they do so at concentrations approximately 100-fold higher. Given the potential polypharmacology of ligands that bind to nuclear receptors, we were most interested in the more potent compounds even if the ultimate levels of gene expression may not be as high.

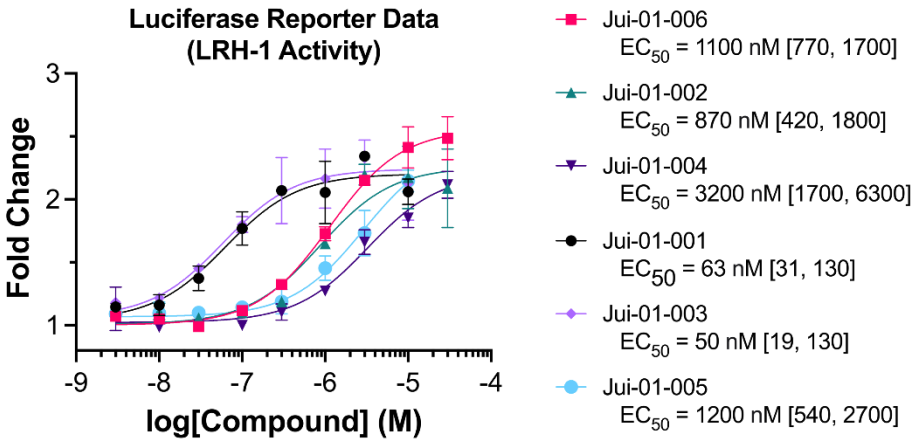

Figure 4.11 Cell based LRH-1 activity assay using a luciferase reporter

Having demonstrated the compound's ability to drive gene expression in an artificial construct, we sought to demonstrate elevated expression of genes relevant to LRH-1 pathophysiology. To do this, we exposed HepG2 hepatocellular carcinoma cells to the compounds at two doses, 1 and 10 micromolar, and looked for expression of three key LRH-1 target genes, CYP7A1, SHP, and STARD (Figure 4.12) Encouragingly we saw a dose-dependent response in expression of all three target genes.

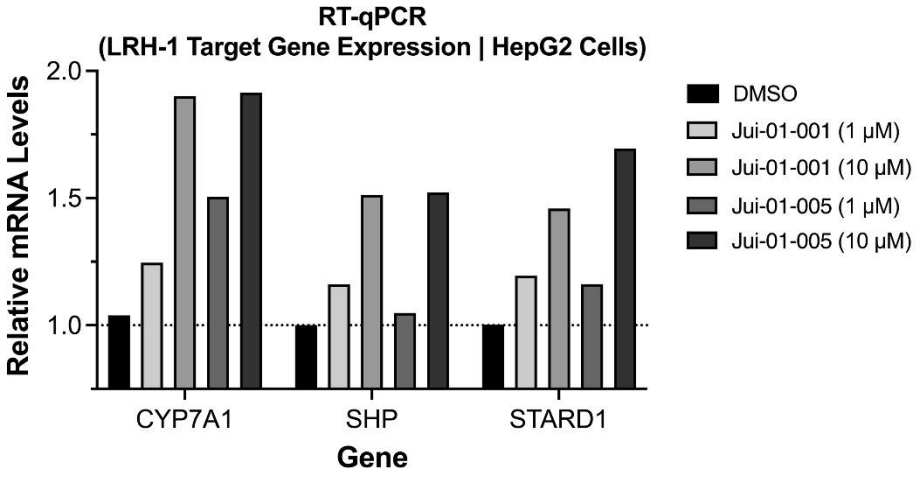

Figure 4.12 Ether compounds drive LRH-1 target gene expression in a dose-dependent manner.

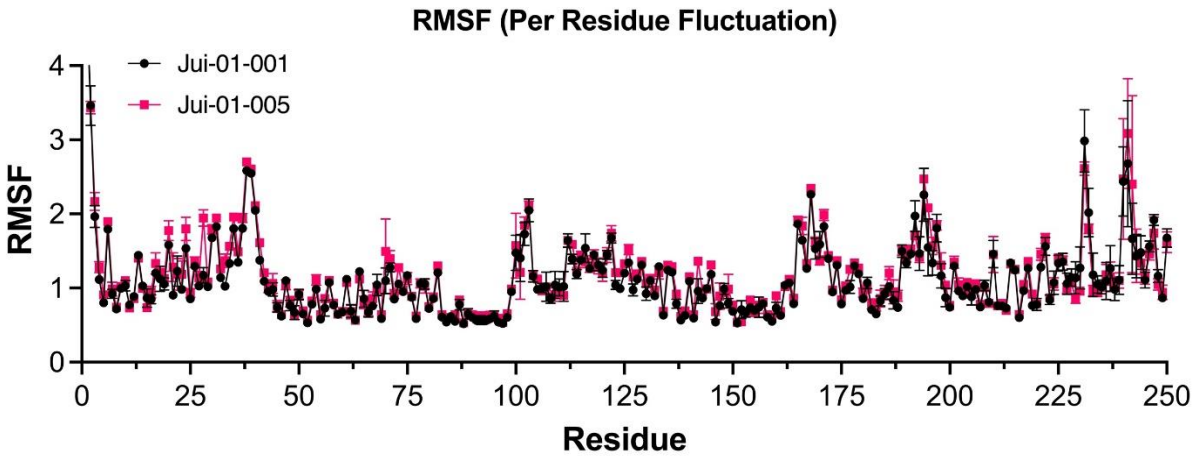

Figure 4.13 Molecular dynamics simulation of the LRH-1 ligand binding domain shows ether compounds behave similarly.

Our lab has thoroughly studied the mechanisms through which 6N-10CA derives its activity, and while we sought to make changes to the physiochemical properties of these compounds, we did not want to alter the means by which they operate. To confirm that they posses the same activity profile, we modeled their binding to LRH-1 utilizing molecular dynamics and compared the position of all residues in the ligand binding domain. Shown in Figure 4.13, the ether containing compounds have a similar modulatory profile to the parent compound. Encouraged by computational modeling and the high measured potency, we sent the compounds out for analysis of solubility, hepatocyte stability, and permeability.

4.5.2 Solubility

If a compound cannot dissolve into solution, it cannot exert any pharmacologic effect. Thus, solubility is an extremely important parameter to consider when developing a drug. Accordingly, we measured the solubility of these compounds in phosphate buffered saline (pH 7.4) to determine their solubility in a biologically relevant media. The results in Table 2 show that

Table 2. Aqueous solubility of ether compounds

	Solubility (μM)
6N-10CA	**111.1**
Jui-002	**234.77**
Jui-003	**259.38**
Jui-005	**304.64**

introduction of a single ether in the tail approximately doubles the aqueous solubility of the compound (Jui-003 vs Jui-001), with the addition of a second compound reaching values outside the assay window (Jui-005). Interestingly, the solubility difference between the sulfamide and the alcohol group is minimal despite the much larger hydrogen bonding network the sulfamide can generate in aqueous solution.

4.5.3 Metabolic Stability

As metabolic stability was one of the important parameters we sought to optimize, we measured the stability of the new compounds in liver microsomes. Liver microsomes contain a vast array of metabolizing enzymes, including cytochrome p450s, reductases, and glutathione-S-transferases; these enzyme families represent a major portion of the metabolic enzymes responsible for drug clearance[100]. Our experimental results are summarized in Table 3. Surprisingly, these results indicate that although the styrene moiety may be a metabolic liability, removing the alcohol for the sulfamide provides a large improvement in drug half-life (Jui-003 $T_{1/2}$: 81 minutes vs Jui-002 $T_{1/2}$: 17 minutes).

Table 3. Liver microsomal stability of ether compounds

	Half-life (min)	CL_{int} (mL/min/Kg)
Jui-002	**17.40**	**348.4**
Jui-003	**81.15**	**74.72**
Jui-005	**92.31**	**65.69**

[100] Knights, K. M., Stresser, D. M., Miners, J. O., & Crespi, C. L. (2016). In vitro drug metabolism using liver microsomes. *Current Protocols in Pharmacology, 2016,* 7.8.1-7.8.24. https://doi.org/10.1002/cpph.9

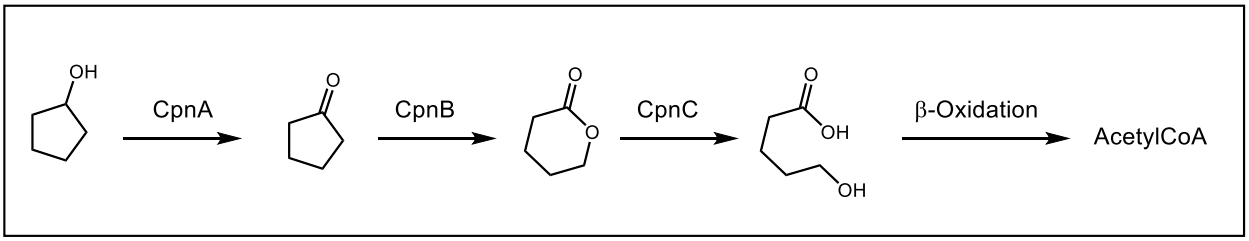

Figure 4.14 Cyclopentanol metabolism in *Pseudomonas*

Cyclopentanol metabolism is known in *Pseudomonas* species, involving an oxidation to the cyclopentanone followed by Bayer-Villager oxidation and ring opening to provide a substrate for lipid catabolic pathways (Figure 4.14).[101] It is likely that a similar oxidative metabolism pathway is dominant here, and the sulfamide is unable to engage in it, leading to a longer half-life. Although further modifications to the structure to block metabolically active sites such as the styrenes would likely provide an even further improved half-life, the metabolic rate that we observed is sufficient for a compound with a nuclear receptor target—activation of genes provides a long-lived biological effect even if the agonist itself has been cleared.

4.5.4 Permeability

While intravenous dosing is a common mode of drug delivery, for treatment of chronic conditions such as inflammatory bowel disease or diabetes an orally bioavailable therapeutic is far more practical. Because xenobiotic compounds are most likely to enter the body through the gut, the junctions between cells in the intestinal epithelium is strong and poorly permeable. Thus, the cellular permeability (passive permeability) of the compounds is crucial to the successful development of an oral drug. The passive permeability of a compound is controlled by

	$P_{app(A-B)}$	$P_{app(B-A)}$	Efflux Ratio
Jui-002	**0.81**	**0.20**	**0.24**
Jui-003	**0.06**	**0.15**	**2.53**
Jui-005	**2.05**	**6.20**	**3.03**

Table 4. Caco-2 Permeability of ether compounds

Note: Apparent permeability presented in 10^{-6}cm/s

[101] Griffin M, Trudgill PW. The metabolism of cyclopentanol by Pseudomonas N.C.I.B. 9872. *Biochem J*. 1972;129(3):595-603. doi:10.1042/bj1290595

how well it can dissolve into the luminal (apical) lipid bilayer, then dissolve back into the aqueous cytosol, into the abluminal (basolateral) lipid bilayer and then into the blood stream. To do this effectively, the compound must be soluble in aqueous environment, which favors charged organic molecules, but also in the organic lipid membrane, which repels charged organic molecules. The design of a compound with superior permeability requires careful balance of the physiochemical properties[102]. In addition to the challenges of purely passive diffusion, the intestinal cells express Pgp transporter proteins, which function as a "hydrophobic vacuum cleaner" actively pumping lipophilic drug-like molecules back into the gut[103]. These are part of the ATP binding cassette superfamily of transporters which utilize the energy stored in ATP to defend the body against potential toxins. The canonical substrates for Pgp proteins include cholesterol, bile acids and lipids.

While there are many ways to measure cell permeability in an *in vitro* assay, the standard by which others are compared is the Caco-2 cell line[104]. This tissue, an immortalized colorectal adenocarcinoma cell line, replicates the intestinal wall extremely well and crucially, has the transporter proteins which are absent in simpler *in vitro* models. Therefore, we used this model system to test the permeability of our compounds. Summarized in Table 4, we observed medium

---

[102] Krishna, G., Chen, K.-J., Lin, C.-C., & Nomeir, A. A. (2001). Permeability of lipophilic compounds in drug discovery using in-vitro human absorption model, Caco-2. In *International Journal of Pharmaceutics* (Vol. 222). www.elsevier.com/locate/ijpharmAbbre6iations:AP,apicalordonorside;BA,basolateralorreceiverside

[103] Mahar Doan KM, Humphreys JE, Webster LO, Wring SA, Shampine LJ, Serabjit-Singh CJ, Adkison KK, Polli JW. Passive permeability and P-glycoprotein-mediated efflux differentiate central nervous system (CNS) and non-CNS marketed drugs. J Pharmacol Exp Ther. 2002 Dec;303(3):1029-37. doi: 10.1124/jpet.102.039255.

[104] Hubatsch, I., Ragnarsson, E. G. E., & Artursson, P. (2007). Determination of drug permeability and prediction of drug absorption in Caco-2 monolayers. *Nature Protocols*, *2*(9), 2111–2119. https://doi.org/10.1038/nprot.2007.303

to poor permeability of the monoether containing compounds (Jui 002 and Jui-005), consistent with approximately 30% of compound absorbed into the blood stream. There was a marked increase in the permeability of the diether compound, $P_{app(A-B)}$ 2.05 for the diether vs 0.06 for the monoether. Furthermore, when comparing the efflux ratios (the measure of a compound's susceptibility for efflux via Pgp pumps), it appears that the sulfamide triggers recognition and efflux (Jui-003: 2.53 vs Jui-005: 0.24). This likely arises due to the similarity of the compound to a phospholipid, one of the main native substrates for these pumps[105]. This data also highlights the complexity involved in the multivariate optimization of drug molecules—the moiety that prevented unwanted metabolism is exactly what triggers unwanted efflux.

4.6 In-vivo evaluation

4.6.1 Tissue Distribution

Following the promising in vitro results, we weighed the relative importance of each datapoint we had collected. While more soluble and more permeable, the diether compound was not nearly as potent as the monoether derivative; to enable selection of a single compound to move forward with, we designed a tissue distribution study that would determine the relative importance of the solubility and permeability metrics. The goal of any drug development project is for the compound to elicit the desired pharmacological effect;

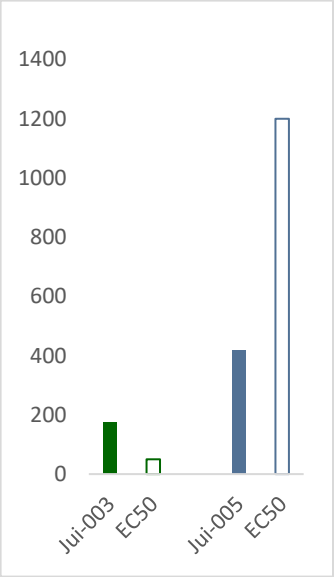

Figure 4.15 Tissue distribution of Jui-003 and Jui-005 and comparison to respective EC_{50} values

[105] Garrigues, A., Escargueil, A. E., & Phane Orlowski, S. (2002). *The multidrug transporter, P-glycoprotein, actively mediates cholesterol redistribution in the cell membrane*. www.pnas.orgcgidoi10.1073pnas.162366399

thus we wanted to measure the tissue concentration of the different compounds and compare those against the cell-based assay readouts which define the efficacy at various compound concentrations. We dosed mice with both compounds at two levels (10 and 100 miligrams per kilogram, mpk) and then collected tissue and analyzed compound concentration via LC-MS/MS. The results of this study are shown in Figure 4.15 (100 mpk dose in liver tissue shown, other doses and tissues omitted for clarity). Despite the enhanced permeability and solubility of the diether, the levels observed in tissue was unlikely to have a significant physiological effect. We decided to further progress Jui-003 into animal models.

4.6.2 Scale-up Synthesis

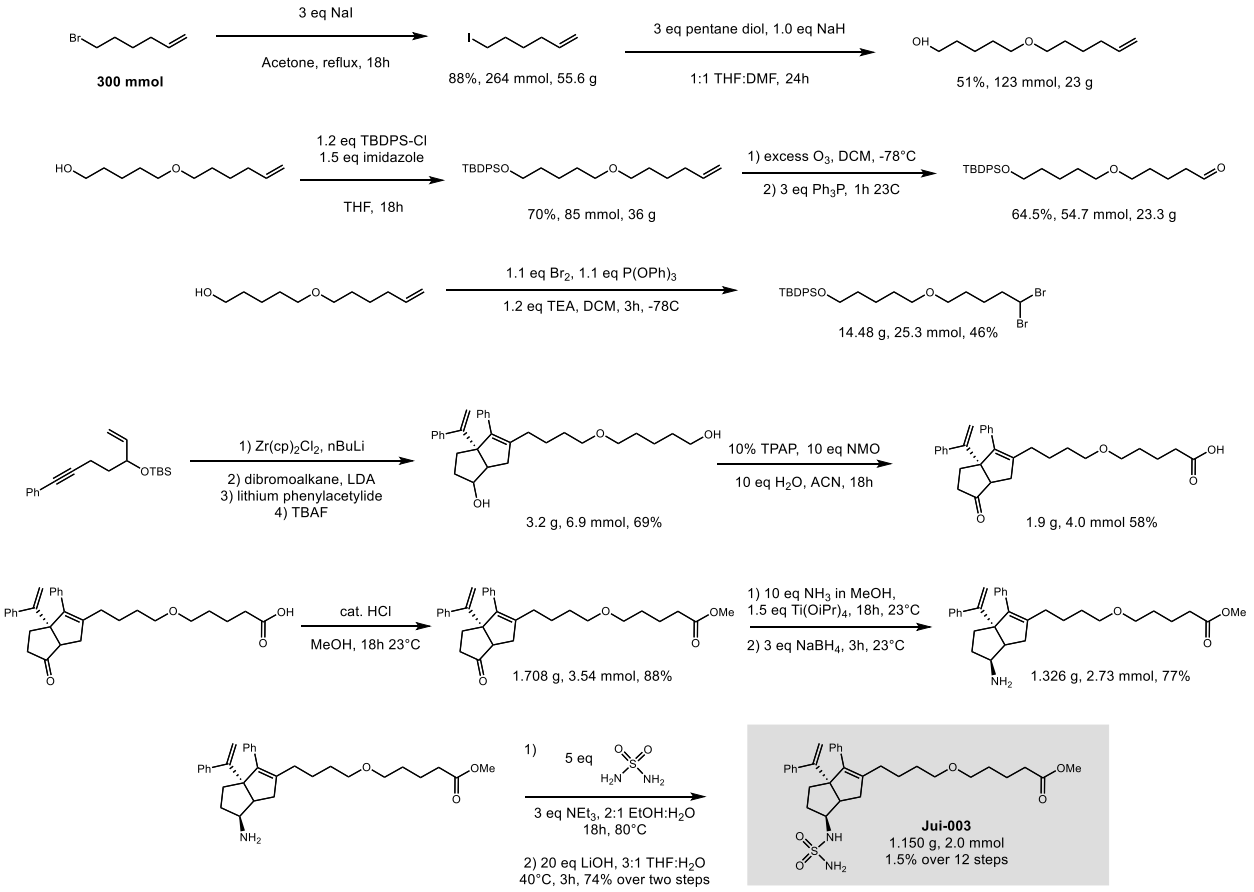

Scheme 14. Scale up of Jui-003, producing >1.1 g (2.0 mmol) of material after 12 synthetic steps

Having identified the candidate compound for advanced in vivo studies, we needed to synthesize sufficient material for its evaluation (Scheme 14). Following the established route, we first iodinated 6-bromo-hex-1-ene with sodium iodide in acetone to provide the alkyl iodide in 88% yield (300 mmol scale). Next, the iodine was displaced with pentane diol (51%, 123 mmol) and then the free alcohol protected as the tertbutyldiphenylsilyl ether (36.0 grams, 70%, 85 mmol). The alkene was treated with ozone and then dibrominated to provide 25.32 mmol of tert-butyl((5-((5,5-dibromopentyl)oxy)pentyl)oxy)diphenylsilane (30% over two steps).

Previously, our group had observed diminished yield when performing the Whitby cyclization on larger scales. Following investigation of the causes, it was determined that incomplete azeotropic

drying of the zirconocene catalyst was to blame. For our scale up efforts, we used zirconocene catalyst that had been stored under completely inert atmosphere and were able to generate reproducible results over increasing scales. For our final synthetic run, we successfully ran the Whidby cyclization on 10 mmol scale to provide 3.2 g of 5-(4-((5-hydroxypentyl)oxy)butyl)-4-phenyl-3a-(1-phenylvinyl)-1,2,3,3a,6,6a-hexahydropentalen-1-ol in 69% yield. Next this material was globally oxidized (58% yield, 4.02 mmol), esterified and the primary amine incorporated via reductive amination (1.326 g, 77%). Finally, the sulfamide was installed and ester hydrolyzed to furnish 1.1 g Jui-003 in 74%. The 12 step synthesis was performed on gram scale with overall yield of 1.5%.

4.6.3 Pharmacokinetics

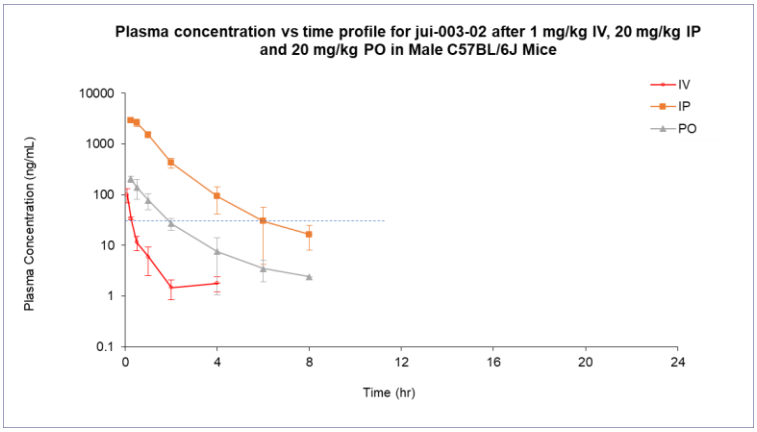

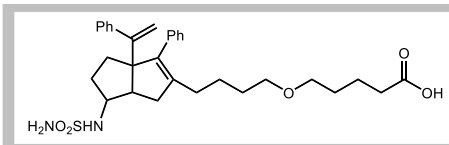

Jui-003

	1 mg/kg IP	20 mg/kg IP	20 mg/kg PO
$T_{1/2}$ (hours)	60	77	232
AUC (h*ng/mL)	42.1	3791	291
C_{max} (ng/mL)	174	2960	203

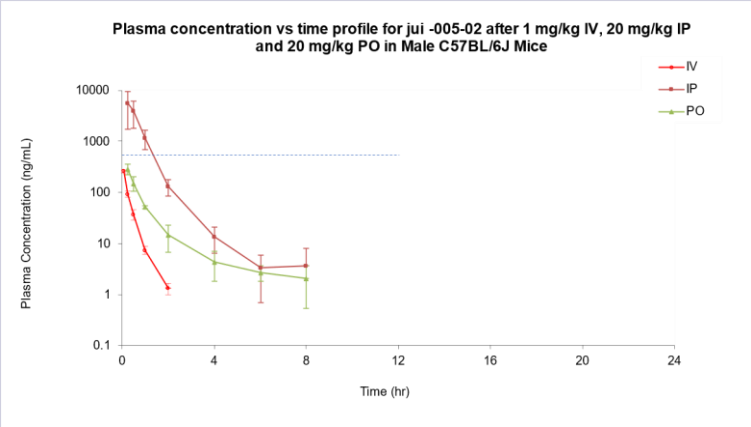

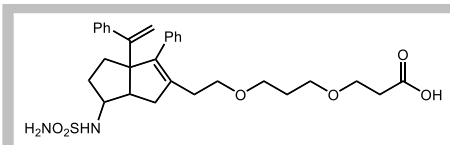

Jui-005

	1 mg/kg IP	20 mg/kg IP	20 mg/kg PO
$T_{1/2}$ (min)	18.7	65	102
AUC (h*ng/mL)	91	2195	212
C_{max} (ng/mL)	431	5580	289

With ample supply of the candidate compound, we next examined the pharmacokinetics of the compound. Pharmacokinetics is the study of what happens to the compound over time once administered; how quickly it is absorbed, the maximum concentration in the plasma, and how quickly it is excreted. All the physiochemical property optimization up to this point is done with the intention of improving the pharmacokinetic properties of the compound.

Compounds Jui-003 and Jui-005 were administered to C57BL/6J mice (n=3) at 1 mg/kg IP, 20 mg/kg IP and 20 mg/kg PO doses. Blood samples were taken at 8 time points over 24 hours and analyzed for the concentration of each compound. The values across individual animals were averaged and the averages plotted (Figure 4.16).

The observed clearance of the compounds (408 mL/min/kg for Jui-003) was considerably higher than the liver microsome assay would predict (74.72 mL/min/kg scaled-up Cl_{int}), suggesting that there are other, dominant, metabolic pathways for the compounds *in vivo*. The bioavailability of the compounds, the percentage of the dose that can be observed in the plasma, was 28% for a 20 mg/kg PO dose. This level of oral bioavailability is encouraging for further development of these compounds.

Albumin, a major blood protein, is responsible for shuttling hydrophobic signaling molecules through the aqueous blood[106]. As a result, hydrophobic drug compounds frequently bind to it which effectively removes them from circulation (plasma protein binding)[107]. Plasma protein binding is an important parameter to consider as compounds move into later stage experiments; while the bound drug is not available to bind to the desired target, it is also blocked from metabolism and thus represents a reservoir of new drug that is gradually released into the tissue as metabolism and excretion occurs[108]. Lipophilic molecules as well as acids frequently display extremely high plasma protein binding, albumin has many surface lysine residues that form salt bridges with acidic molecules[109]. Our compounds are

Table 5. Jui-003 and Jui-005 are highly plasma protein bound.

Plasma Protein Binding	
Jui-003	99.33%
Jui-005	97.16%

[106] Pardridgef, W. M. (1981). *Transport of Protein-Bound Hormones into Tissues in Vivo*. Endocrine Reviews. 2(1), 103-123.

[107] Bohnert T, Gan LS. Plasma protein binding: from discovery to development. J Pharm Sci. 2013 Sep;102(9):2953-94. doi: 10.1002/jps.23614.

[108] Trainor, G. L. (2007). The importance of plasma protein binding in drug discovery. In *Expert Opinion on Drug Discovery* (Vol. 2, Issue 1, pp. 51–64). https://doi.org/10.1517/17460441.2.1.51

[109] Zsila, F., Bikadi, Z., Malik, D., Hari, P., Pechan, I., Berces, A., & Hazai, E. (2011). Evaluation of drug-human serum albumin binding interactions with support vector machine aided online automated docking. *Bioinformatics*, *27*(13), 1806–1813. https://doi.org/10.1093/bioinformatics/btr284

both lipophilic and contain an acid functionality and thus it is unsurprising that they are highly bound. Given the relatively rapid clearance, the plasma protein binding may be beneficial for long-acting effects.

Shown in Figure 4.16 is the plasma concentration of Jui-003 and Jui-005 vs the compound EC50. Jui-003 displays substantial time over the EC50 (6h for 20 mg/kg IP dose) while Jui-005 has EC50 coverage for a mere 80 minutes. This level of exposure is encouraging, as the previous generation of compounds (6N-10CA) had half-lives on the order of ca. 15 minutes. With a half-life in hours, these compounds generate sufficient exposure for true biological activity studies with convenient dosing regimens.

4.6.4 Target Engagement

After demonstrating the compounds have exposure in the body for multiple hours, we next turned to measuring their *in vivo* biological activity. Jui-003 was administered to LRH-1 humanized C57-B6 mice at 3 and 30 mg/kg twice daily for three days and then the animals sacked, and the liver tissue resected. The liver tissue was analyzed for mRNA transcripts of genes regulated by LRH-1. Shown in Figure 4.17, the levels of CYP7A1 increased by more than 7-fold and the levels of FASN decreased in a significant and dose-dependent manner.

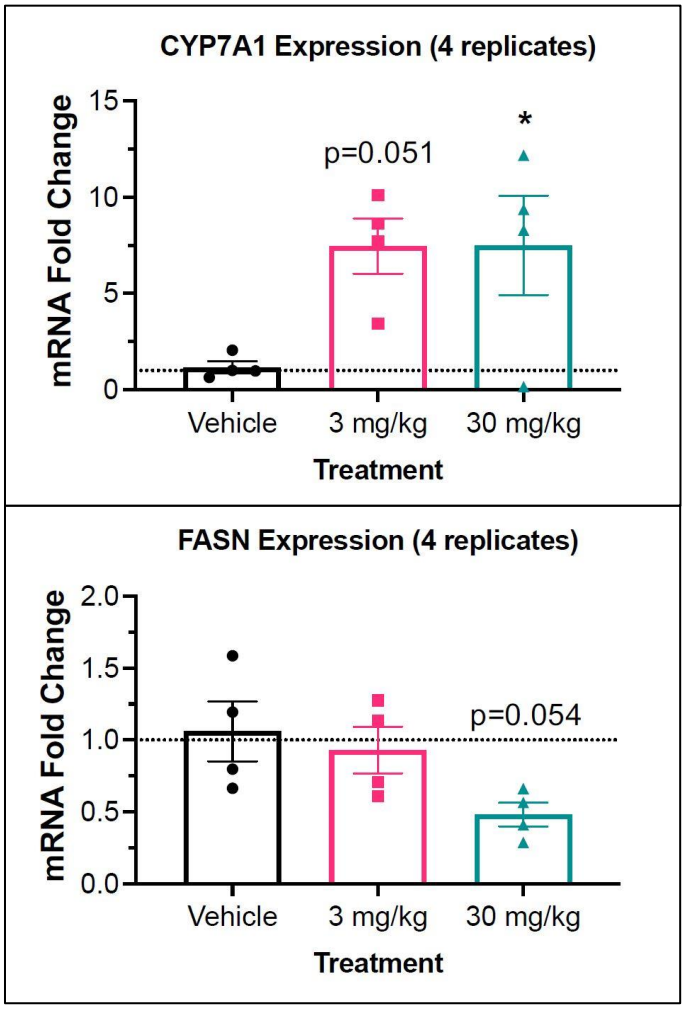

Figure 4.16. mRNA expression levels of LRH-1 regulated genes following administration of Jui-003

CYP7A1 (cholesterol 7 alpha-hydroxylase) is the rate limiting step in bile acid biosynthesis, and deficiency in this enzyme results in fat accumulation in the liver, hypercholesterolemia, and subsequent metabolic disorders[110]. The ability to increase the expression of CYP7A1 has the profound ability to reduce these pathologies and thus treat metabolic diseases such as diabetes and NAFLD.

[110] Pandak, W. M., Schwarz, C., Hylemon, P. B., Mallonee, D., Valerie, K., Heuman, D. M., Fisher, R. A., Redford, K., Vlahcevic, Z. R., & Mal-Lonee, D. (n.d.). *Effects of CYP7A1 overexpression on cholesterol and bile acid homeostasis*. http://www.ajpgi.org

Increasing CYP7A1 with a concomitant decrease in FASN is additionally beneficial. Fatty acid synthase (FASN), as the name suggests, is responsible for synthesis of palmitic acid from acetyl coenzyme A[111]. Downregulation of this gene decreases the amount of fatty acids being synthesized. Furthermore, fatty acid synthase is overexpressed in prostate, breast, and gastric cancers and has been studied as a possible therapeutic target for these indications[112].

4.7 Conclusion

Modulation of LRH-1 as a means of altering disease related gene expression is an attractive therapeutic strategy for cardiovascular disease, inflammatory diseases of the gut, and cancer. These represent some of the largest disease burdens currently facing our country and the world. Previous generations of LRH-1 agonists have proven efficacy in cell-based experiments, but do not posses the properties required to progress into more accurate models of the pertinent diseases. Here we disclosed the strategic design and synthesis of an improved LRH-1 agonist that possesses a clinically relevant half-life and strong modulation of disease-relevant genes *in vivo.* These data support continued development of this compound as a potential therapeutic for the treatment of inflammatory and cardiovascular disease.

---

[111] Huang, M., Koizumi, A., Narita, S., Inoue, T., Tsuchiya, N., Nakanishi, H., Numakura, K., Tsuruta, H., Saito, M., Satoh, S., Nanjo, H., Sasaki, T., & Habuchi, T. (2016). Diet-induced alteration of fatty acid synthase in prostate cancer progression. *Oncogenesis, 5*. https://doi.org/10.1038/oncsis.2015.42

[112] Lupu R, Menendez JA. Pharmacological inhibitors of Fatty Acid Synthase (FASN)--catalyzed endogenous fatty acid biogenesis: a new family of anti-cancer agents? Curr Pharm Biotechnol. 2006 Dec;7(6):483-93. doi: 10.2174/138920106779116928.

4.8 Supporting Information

GENERAL INFORMATION:

All reactions were carried out in oven-dried glassware, equipped with a stir bar and under a nitrogen atmosphere with dry solvents under anhydrous conditions, unless otherwise noted. Solvents used in anhydrous reactions were purified by passing over activated alumina and storing under argon. Yields refer to chromatographically and spectroscopically (1H NMR) homogenous materials, unless otherwise stated. Reagents were purchased at the highest commercial quality and used without further purification, unless otherwise stated. n-Butyllithium (n-BuLi) was used as a 2.5 M solution in hexanes (Aldrich), was stored at 4°C and titrated prior to use. Organic solutions were concentrated under reduced pressure on a rotary evaporator using a water bath. Chromatographic purification of products was accomplished using forced-flow chromatography on 230-400 mesh silica gel. Preparative thin-layer chromatography (PTLC) separations were carried out on 1000μm SiliCycle silica gel F-254 plates. Thin-layer chromatography (TLC) was performed on 250μm SiliCycle silica gel F-254 plates. Visualization of the developed chromatogram was performed by fluorescence quenching or by staining using KMnO4, p-anisaldehyde, or ninhydrin stains.

^{1}H and ^{13}C NMR spectra were obtained from the Emory University NMR facility and recorded on a Bruker Avance III HD 600 equipped with cryo-probe (600 MHz), INOVA 600 (600 MHz), INOVA 500 (500 MHz), INOVA 400 (400 MHz), VNMR 400 (400 MHz), or Mercury 300 (300 MHz), and are internally referenced to residual protio solvent signals. Data for ^{1}H NMR are reported as follows: chemical shift (ppm), multiplicity (s = singlet, d = doublet, t = triplet, q = quartet, m = multiplet, dd = doublet of doublets, dt = doublet of triplets, ddd= doublet of doublet

of doublets, dtd= doublet of triplet of doublets, b = broad, etc.), coupling constant (Hz), integration, and assignment, when applicable. Data for decoupled ^{13}C NMR are reported in terms of chemical shift and multiplicity when applicable. Gas Chromatography Mass Spectrometry (GC-MS) was performed on an Agilent 5977A mass spectrometer with an Agilent 7890A gas chromatography inlet. Liquid Chromatography Mass Spectrometry (LC-MS) was performed on an Agilent 6120 mass spectrometer with an Agilent 1220 Infinity liquid chromatography inlet. Preparative High-Pressure Liquid chromatography (Prep-HPLC) was performed on an Agilent 1200 Infinity Series chromatograph using an Agilent Prep-C18 30 x 250 mm 10 μm column, or an Agilent Prep-C18 21.2 x 100 mm, 5 μm column.

Purity of all tested compounds was determined by HPLC analysis, using one of the methods given below:

Method A: A linear gradient using water and 0.1 % formic acid (FA) (Solvent A) and MeCN and 0.1% FA (Solvent B); t = 0 min, 30% B, t = 4 min, 99% B (held for 1 min), then 50% B for 1 min, was employed on an Agilent Poroshell 120 EC-C18 2.7 micron, 3.0 mm x 50 mm column (flow rate 1 mL/min) or an Agilent Zorbax SB-C18 1.8 micron, 2.1 mm x 50 mm column (flow rate 0.8 mL/min). The UV detection was set to 254 nm. The LC column was maintained at ambient temperature.

Method B: A linear gradient using water and 0.1 % formic acid (FA) (Solvent A) and MeCN and 0.1% FA (Solvent B); t = 0 min, 70% B, t = 4 min, 99% B (held for 1 min), then 50% B for 1 min, was employed on an Agilent Poroshell 120 EC-C18 2.7 micron, 3.0 mm x 50 mm column (flow rate 1 mL/min) or an Agilent Zorbax SB-C18 1.8 micron, 2.1 mm x 50 mm column (flow rate 0.8

mL/min). The UV detection was set to 254 nm. The LC column was maintained at ambient temperature.

Method C: A linear gradient using water and 0.1 % formic acid (FA) (Solvent A) and MeCN and 0.1% FA (Solvent B); t = 0 min, 5% B, t = 6 min, 95% B (held for 2 min), then 5% B for 1 min, was employed on an Agilent Poroshell 120 EC-C18 2.7 micron, 3.0 mm x 50 mm column (flow rate 1 mL/min) or an Agilent Zorbax SB-C18 1.8 micron, 2.1 mm x 50 mm column (flow rate 0.8 mL/min). The UV detection was set to 254 nm. The LC column was maintained at ambient temperature.

GENERAL PROCEDURES:

General Procedure A:

Hexahydropentalene formation was accomplished through slight modification of Whitby's procedure[113]. Prior to cyclization, all non-volatile reagents were dried by azeotropic removal of water using benzene. A dry round bottom flask containing bis(cyclopentadienyl)zirconium(IV) dichloride (1.2 equiv) under nitrogen, was dissolved in anhydrous, degassed tetrahydrofuran (THF, 8 mL/mmol enyne) and cooled to -78 °C. The resulting solution was treated with n-BuLi (2.4

[113] Whitby, R. J., Dixon, S., Maloney, P. R., Delerive, P., Goodwin, B. J., Parks, D. J., & Willson, T. M. (2006). Identification of small molecule agonists of the orphan nuclear receptors liver receptor homolog-1 and steroidogenic factor-1. *Journal of Medicinal Chemistry*, *49*(23), 6652–6655. https://doi.org/10.1021/jm060990k

equiv.) and the light yellow solution was stirred for 45 minutes. A solution of Enyne (prepared according to Flynn et al[114]) (1.0 equiv) in anhydrous, degassed THF (8 mL/mmol) was added. The resulting salmon-colored mixture was stirred at -78 °C for 45 minutes, the cooling bath removed, and the reaction mixture was allowed to warm to ambient temperature while stirring (2.5 hours total). The reaction mixture was then cooled to -78 °C and the required 1,1-dibromoalkane tail (1.1 equiv) was added as a solution in anhydrous THF (8 mL/mmol enyne) followed by freshly prepared lithium diisopropylamide (LDA, 1.0 M, 1.1 equiv.). After 15 minutes, a freshly prepared solution of lithium phenylacetylide (3.6 equiv.) in anhydrous THF (8 mL/ mmol enyne) was added dropwise and the resulting rust-colored solution was stirred at -78 °C for 1.5 hours. The reaction was quenched with methanol and saturated aqueous sodium bicarbonate and allowed to warm to room temperature, affording a light yellow slurry. The slurry was poured onto water and extracted with ethyl acetate four times. The combined organic layers were washed with brine, dried with MgSO4, and concentrated in vacuo. The resulting yellow oil was passed through a short plug of silica (100% EtOAc eluent) and concentrated. The crude product was dissolved in THF and treated with either HCl or TBAF. The resulting solution stirred at room temperature for 16 h. The reaction mixture was concentrated and the diastereomers were purified and separated by flash chromatography.

General Procedure B:

To a solution of diol (1 equiv) in acetonitrile (0.1 M) was added tetrapropylammonium perruthenate (TPAP) (0.1 equiv), N-methylmorpholine N-oxide (NMO) (10 equiv), and water (10

[114] Flynn, A. R., Mays, S. G., Ortlund, E. A., & Jui, N. T. (2018). Development of Hybrid Phospholipid Mimics as Effective Agonists for Liver Receptor Homologue-1. *ACS Medicinal Chemistry Letters*, *9*(10), 1051–1056. https://doi.org/10.1021/acsmedchemlett.8b00361

equiv) and stirred at room temperature overnight. The reaction solution was then filtered through a pad of silica with (100% EtOAc) and concentrated. The resulting mixture was purified by flash chromatography to give the title compound.

General Procedure C:

To a solution of 14c-d(1 equiv) in methanol (0.1 M) was added three drops of concentrated HCl and stirred at room temperature overnight. Reaction solution was then concentrated in vacuo and filtered through a pad of silica to collect the title compound.

General Procedure D:

To a flame-dried screw top test tube charged with a stir bar backfilled (3x) was added 15a-b (1.0 equiv.) and ethanol (0.1 M). Ammonia (7 M in methanol, 5.0 or 20.0 equiv) then titanium(IV) isopropoxide (0.33 mL, 1.08 mmol, 1.5 equiv) were added via syringe and stirred at room temperature for 6 hours. The test tube cap was then removed and sodium borohydride (3.0 equiv) added portion-wise. The resulting solution was stirred at room temperature for 30 minutes before being diluted with EtOAc. The solution was adjusted to a pH of 1 with 1M HCl. The layers were separated and the aqueous layer was extracted 3x with EtOAc. The combined organic layers were then dried over Na_2SO_4, filtered, and concentrated in vacuo before being purified by flash chromatography to give the title compound.

General Procedure E:

Amine starting material (1 eq) and sulfamide (5 eq) were charged to a round bottom flask containing a stir bar. The reagents were then dissolved in water (20 mL/mmol) and ethanol (10

mL/mmol). Next, triethylamine was added (3 eq) and the reaction heated to 80 °C. Once complete by LC-MS analysis (typically 16h), the reaction was cooled and then concentrated by half.

THF (40 mL/mmol) was added followed by lithium hydroxide (10 eq). The mixture was stirred for 4h (heating to 40 °C if necessary). Reaction concentrated to remove THF, then 1M potassium hydrogen sulfate (15 mL/mmol) was added followed by 10% methanol in DCM (15 mL/mmol). The aqueous layer was extracted three times with 10% methanol in DCM (15 mL/mmol) and the organic layers combined, dried over anhydrous sodium sulfate and then concentrated to a crude oil. The oil was purified by silica chromatography to provide the title compound.

General Procedure F:

A reaction vial was charged with a stir bar and methoxymethyl ether starting was dissolved in dioxane and a 5 drops of concentrated HCl was then added. The reaction was heated to 40 °C, stirred until complete, then cooled and diluted with EtOAc and washed with 3 x 5 mL 0.5 M aqueous HCl, 5 ml water, and 5 mL brine. The organic layer was then dried over Na_2SO_4, filtered, and concentrated in vacuo to give the title compound after flash chromatography.

SYNTHESIS OF INDIVIDUAL COMPOUNDS:

Synthesis of monoether compounds

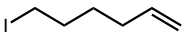

6-iodohex-1-ene (1): To a round bottom flask under nitrogen flow was added sodium iodide (93.68 g, 5 eqivalents, 625 mmol), acetone (300 mL) and 6-bromo-1-hexene (125 mmol, 1 eq, 16.75 mL). The suspension was stirred and heated to reflux for 18h. The reaction was then loaded onto a silica plug, eluted with hexanes, 1:1 hexanes and MTBE, and MTBE (75 mL each). The organics were concentrated to a colorless oil. 21.9 g, 104 mmol, 83%. ^{1}H NMR (600 MHz, Chloroform-d) δ 5.76 (ddtd, J = 17.0, 10.2, 6.7, 1.5 Hz, 1H), 4.99 (dp, J = 17.1, 1.7 Hz, 1H), 4.94 (dp, J = 10.2, 1.6 Hz, 1H), 3.17 (td, J = 7.0, 1.5 Hz, 2H), 2.05 (qd, J = 7.3, 1.5 Hz, 2H), 1.85 – 1.76 (m, 2H), 1.48 (pd, J = 7.5, 1.5 Hz, 2H). ^{13}C NMR (151 MHz, Chloroform-d) δ 138.12, 115.00, 32.91, 32.62, 29.69, 6.82.

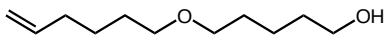

5-(hex-5-en-1-yloxy)pentan-1-ol (2): Sodium hydride (60% in mineral oil, 3.46 g, 86 mmol, 1 eq) was added to a flame dried round bottom flask under positive nitrogen pressure followed by 115 mL of DMF and 115 mL of THF. This was cooled to 0°C and then 1,5-pentane diol (27.2 mL, 3.0 eq, 260 mmol) was added dropwise. The resulting solution was stirred for 20 minutes, then 6-iodohex-1-ene (1) was added dropwise. The reaction was stirred overnight and allowed to warm to room temperature. In the morning, saturated ammonium chloride was added to quench the reaction and then the mixture was extracted with ethyl acetate (3x 100 mL). The organics was combined, dried, and concentrated to provide a crude oil that was purified by silica chromatography (0-20% EtOAc:hexanes) to yield the title compound. 8.01 g, 43 mmol, 50% ^{1}H NMR (600 MHz, Chloroform-d) δ 5.80 (ddtd, J = 16.9, 10.1, 6.7, 0.9 Hz, 1H), 5.00 (dtd, J = 17.1, 2.6, 1.5 Hz, 1H), 4.94 (ddq, J = 10.1, 2.2, 1.1 Hz, 1H), 3.64 (td, J = 6.5, 0.9 Hz, 2H), 3.40 (tdd, J

= 6.6, 3.8, 0.9 Hz, 4H), 2.06 (tdd, J = 7.8, 6.4, 1.3 Hz, 2H), 1.63 – 1.55 (m, 6H), 1.47 – 1.40 (m, 4H).

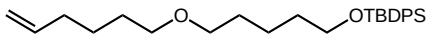

***tert*-butyl((5-(hex-5-en-1-yloxy)pentyl)oxy)diphenylsilane** (3): 8.01 g of 5-(hex-5-en-1-yloxy)pentan-1-ol (2) (43 mmol) was dissolved in 400 mL of dry THF, followed by 4.39 g imidazole (1.5 eq, 64.5 mmol). The mixture was stirred for 5 minutes until it was homogeneous and then TBDPS-Cl (1.2 eq, 51.6 mmol, 13.42 mL) was added dropwise. Stirred overnight at room temperature. The reaction was concentrated to approximately 150 mL and passed through a celite plug to remove imidazolium salts. The filtrate was then concentrated to a clear oil that was purified by silica chromatography (1-7% EtOAc/hexanes). 12.9 g, 30.37 mmol, 70% ^{1}H NMR (600 MHz, Chloroform-d) δ 7.69 – 7.64 (m, 4H), 7.44 – 7.35 (m, 6H), 5.80 (ddt, J = 16.9, 10.2, 6.7 Hz, 1H), 5.00 (dq, J = 17.1, 1.7 Hz, 1H), 4.94 (ddt, J = 10.2, 2.5, 1.2 Hz, 1H), 3.65 (t, J = 6.5 Hz, 2H), 3.38 (dt, J = 9.3, 6.6 Hz, 4H), 2.10 – 2.03 (m, 2H), 1.62 – 1.51 (m, 6H), 1.48 – 1.37 (m, 4H), 1.04 (s, 9H). ^{13}C NMR (151 MHz, Chloroform-d) δ 138.83, 135.59, 134.15, 129.50, 127.59, 114.47, 70.87, 70.73, 63.89, 33.60, 32.42, 29.52, 29.26, 26.89, 25.53, 22.45, 19.23.

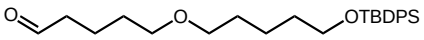

5-((5-((*tert*-butyldiphenylsilyl)oxy)pentyl)oxy)pentanal (4): 9.59 mmol (4.06 g) of starting material was dissolved in 150 mL of dry DCM and the reaction cooled to -78 °C. Next, ozone was bubbled through the reaction while stirring until a blue color persisted. Oxygen was then bubbled

through the reaction to flush remaining ozone and then 3 equivalents (7.73 g) of triphenylphosphine was added. The reaction was warmed to room temperature and stirred for 3 hours. The solvent was removed in vacuo and the resulting oil purified by silica chromatography (0-20% EtOAc/hexanes). 3.083 g, 76% ^{1}H NMR (600 MHz, Chloroform-d) δ 9.76 (t, J = 1.8 Hz, 1H), 7.71 – 7.60 (m, 4H), 7.46 – 7.33 (m, 6H), 3.66 (t, J = 6.5 Hz, 2H), 3.39 (dt, J = 18.5, 6.5 Hz, 4H), 2.45 (td, J = 7.3, 1.8 Hz, 2H), 1.75 – 1.67 (m, 2H), 1.64 – 1.51 (m, 6H), 1.45 – 1.36 (m, 2H), 1.04 (s, 9H). ^{13}C NMR (101 MHz, Chloroform-d) δ 202.67, 135.58, 134.11, 129.53, 127.60, 70.96, 70.26, 63.85, 43.66, 32.40, 29.48, 29.18, 26.88, 22.44, 19.24, 19.00.

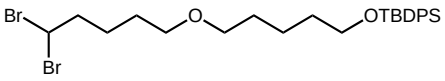

***tert*-butyl((5-((5,5-dibromopentyl)oxy)pentyl)oxy)diphenylsilane**: Under nitrogen, a solution of triphenylphosphite (2.35 mL, 9 mmol, 1.1 equiv) in DCM (50 mL) was cooled to -78 °C. Bromine (0.48 mL, 9 mmol, 1.1 equiv) and triethylamine (1.32 mL, 9 mmol, 1.1 equiv) were sequentially added dropwise at -78 °C. The reaction was stirred for 5 minutes, then S1b (5.8 g, 14 mmol, 1.0 equiv) was added as a solution in DCM (10 mL) via syringe at -78 °C. The reaction was stirred for 5 h and allowed to warm to ambient temperature. The whole reaction was then poured over a pad of silica. The filtrate was concentrated and purified on a short plug of silica with 5% MTBE in hexanes to afford the title compound as a clear, colorless oil (3.35 g, 72%, 10 mmol). ^{1}H NMR (600 MHz, Chloroform-*d*) δ 7.64 (dt, *J* = 8.0, 1.4 Hz, 4H), 7.44 – 7.31 (m, 6H), 5.67 (td, *J* = 6.2, 1.1 Hz, 1H), 3.63 (td, *J* = 6.5, 1.2 Hz, 2H), 3.42 – 3.29 (m, 4H), 2.38 (dddt, *J* = 7.6, 6.1, 4.2, 2.0

Hz, 2H), 1.66 – 1.46 (m, 9H). ^{13}C NMR (151 MHz, Chloroform-*d*) δ 135.58, 129.51, 128.35, 127.59, 70.98, 70.28, 63.87, 46.01, 45.20, 32.39, 29.48, 28.38, 26.89, 25.10, 22.45, 19.24.

Jui-002

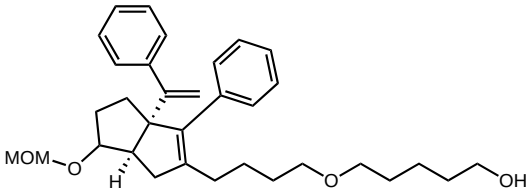

5-(4-((3aR,6aR)-6-(methoxymethoxy)-3-phenyl-3a-(1-phenylvinyl)-1,3a,4,5,6,6a-hexahydropentalen-2-yl)butoxy)pentan-1-ol According to general procedure A, *tert*-butyl((5-((5,5-dibromopentyl)oxy)pentyl)oxy)diphenylsilane (2.50 g, 4.4 mmol) was reacted with (5-(methoxymethoxy)hept-6-en-1-yn-1-yl)benzene (1.20 g, 4 mmol) before being treated with 5 equivalents of tetrabutylammonium fluoride to give the title compound (1.2 g, 5:1 dr, 60% yield over 2 steps) as a yellow oil after purification by flash chromatography (0-50% EtOAc/Hex eluent).

^{1}H NMR (600 MHz, Chloroform-*d*) δ 7.32 – 7.25 (m, 3H), 7.24 – 7.20 (m, 5H), 7.18 (dt, *J* = 8.1, 1.5 Hz, 2H), 5.02 (q, *J* = 2.5, 2.0 Hz, 1H), 4.98 (q, *J* = 2.4, 1.9 Hz, 1H), 4.60 – 4.54 (m, 2H), 3.79 – 3.73 (m, 1H), 3.66 – 3.57 (m, 4H), 3.34 (td, *J* = 6.6, 1.3 Hz, 2H), 3.28 (d, *J* = 1.3 Hz, 3H), 2.39 (dq, *J* = 9.6, 1.8 Hz, 1H), 2.26 (dddd, *J* = 9.8, 7.0, 3.1, 1.2 Hz, 1H), 2.03 – 1.96 (m, 3H), 1.60 – 1.52 (m, 8H), 1.49 – 1.34 (m, 8H).

LRMS (APCI) m/z calc'd for $C_{33}H_{44}O_4$: 505.31, found 473.3 (13a - $CH_3O^{\bullet}$)

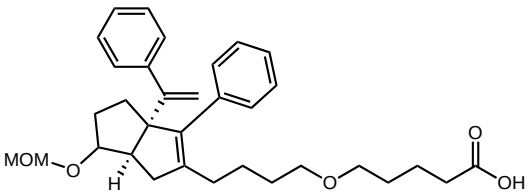

5-(4-((3aR,6aR)-6-(methoxymethoxy)-3-phenyl-3a-(1-phenylvinyl)-1,3a,4,5,6,6a-hexahydropentalen-2-yl)butoxy)pentanoic acid Following general procedure B, a solution of 5-(4-((3aR,6aR)-6-(methoxymethoxy)-3-phenyl-3a-(1-phenylvinyl)-1,3a,4,5,6,6a-hexahydropentalen-2-yl)butoxy)pentan-1-ol (504 mg, 1 eq) in 50 mL acetonitrile was treated with tetrapropylammonium perruthenate (TPAP, 0.1 equiv, 17.55 mg), N-Methylmorpholine-N-Oxide (NMO, 10 equiv, 1.17 g), and water (10 equiv, 180 microliters). The reaction mixture was allowed to stir overnight at room temperature. The reaction mixture was passed through celite, concentrated and purified on silica (0-65% EtOAc (containing 0.1% AcOH)/hexanes eluent) to provide the title compound. 70 mg, 13%

^{1}H NMR (600 MHz, Chloroform-*d*) δ 7.38 – 7.28 (m, 4H), 7.28 – 7.25 (m, 3H), 7.25 – 7.22 (m, 2H), 5.06 (d, *J* = 1.2 Hz, 1H), 5.04 (t, *J* = 1.2 Hz, 1H), 4.64 (s, 2H), 3.81 (dd, *J* = 4.5, 2.6 Hz, 1H), 3.42 (q, *J* = 5.8 Hz, 2H), 3.37 (dd, *J* = 6.1, 1.2 Hz, 5H), 2.39 (t, *J* = 7.6 Hz, 2H), 1.71 – 1.59 (m, 4H), 1.56 – 1.41 (m, 5H), 1.36 – 1.23 (m, 10H).

LRMS (APCI) m/z calc'd for $C_{33}H_{42}O_5$: 519.3, found 487.3 (14a - $CH_3O^{\bullet}$)

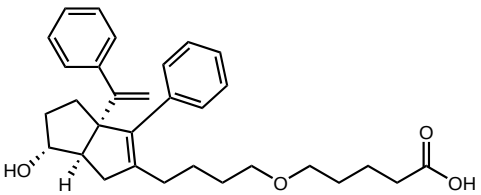

5-(4-((3aR,6aR)-6-hydroxy-3-phenyl-3a-(1-phenylvinyl)-1,3a,4,5,6,6a-hexahydropentalen-2-yl)butoxy)pentanoic acid. According to general procedure F, 70 mg of 5-(4-((3aR,6aR)-6-(methoxymethoxy)-3-phenyl-3a-(1-phenylvinyl)-1,3a,4,5,6,6a-hexahydropentalen-2-yl)butoxy)pentanoic acid was dissolved in dioxane and then 5 drops of concentrated HCl was added. The reaction was stirred at room temp until complete by TLC and HPLC. The reaction was then concentrated and purified by silica chromatography (30-100% EtOAc/Hexanes w/ 1% AcOH). 27 mg, 42%

^{1}H NMR: ^{1}H NMR (600 MHz, Chloroform-*d*) δ 7.35 – 7.28 (m, 5H), 7.24 – 7.18 (m, 5H), 5.06 (d, *J* = 1.3 Hz, 1H), 5.00 (d, *J* = 1.4 Hz, 1H), 3.95 (s, 1H), 3.39 (t, *J* = 6.2 Hz, 2H), 3.34 (t, *J* = 6.3 Hz, 2H), 2.39 (t, *J* = 7.3 Hz, 2H), 2.34 – 2.28 (m, 1H), 2.12 – 1.98 (m, 4H), 1.77 – 1.57 (m, 11H), 1.52 – 1.45 (m, 1H), 1.42 (q, *J* = 7.6, 7.2 Hz, 1H).

LRMS (APCI) m/z[M+H]$^+$ calc'd for $C_{31}H_{38}O_4$: 475.28, found 475.3

Jui-003

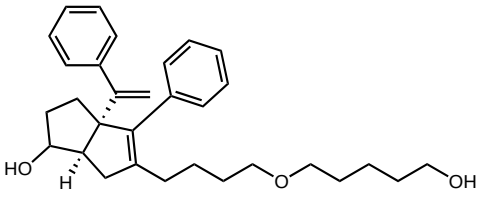

(3a*R*,6a*R*)-5-(4-((5-hydroxypentyl)oxy)butyl)-4-phenyl-3a-(1-phenylvinyl)-1,2,3,3a,6,6a-hexahydropentalen-1-ol: According to general procedure A, *tert*-butyl((5-((5,5-dibromopentyl)oxy)pentyl)oxy)diphenylsilane (2.50 g, 4.4 mmol) was reacted with tert-butyldimethyl((7-phenylhept-1-en-6-yn-3-yl)oxy)silane (1.20 g, 4 mmol) before being treated

with three drops of HCl to give the title compound (1.21 g, X dr, 66% yield over 2 steps) as a yellow oil after purification by flash chromatography (0-65% EtOAc/Hex eluent).

^{1}H NMR (600 MHz, Chloroform-*d*) δ 7.35 – 7.30 (m, 5H), 7.25 (m, 2H), 7.20 (t, *J* = 6.8 Hz, 3H), 5.07 (d, *J* = 1.6 Hz, 1H), 4.99 (dp, *J* = 1.5 Hz, 1H), 3.95 (m, 1H), 3.65 (t, *J* = 6.6 Hz, 3H), 3.38 (t, *J* = 6.4 Hz, 4H), 3.33 (t, *J* = 6.3 Hz, 2H), 2.64 (d, *J* = 17.3 Hz, 1H), 2.47 (t, *J* = 8.7 Hz, 1H), 2.42 – 2.24 (m, 2H), 2.14 – 1.94 (m, 6H), 1.76 – 1.64 (m, 4H), 1.59 (dd, *J* = 10.7, 4.6 Hz, 4H), 1.55 – 1.46 (m, 1H).

LRMS (APCI) m/z[M+H]$^+$ calc'd for $C_{31}H_{41}O_3$: 461.7, found 461.3

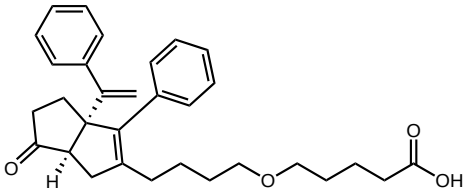

5-(4-((3a*R*,6a*R*)-6-oxo-3-phenyl-3a-(1-phenylvinyl)-1,3a,4,5,6,6a-hexahydropentalen-2-yl)butoxy)pentanoic acid: According to general procedure B, (3a*R*,6a*R*)-5-(4-((5-hydroxypentyl)oxy)butyl)-4-phenyl-3a-(1-phenylvinyl)-1,2,3,3a,6,6a-hexahydropentalen-1-ol (1.21 g, 2.63 mmol) was reacted with TPAP (92.4 mg, 0.26 mmol), NMO (3.07 g, 26 mmol), water (473μL, 473 mg, 26 mmol), and acetonitrile (40 mL) to give the title compound (529 mg, 43% yield) as an oil after purification by flash chromatography (0-65% EtOAc/Hex).

^{1}H NMR (600 MHz, Chloroform-*d*) δ 7.36 – 7.31 (m, 2H), 7.30 – 7.26 (m, 3H), 7.23 (m, 3H), 7.20 – 7.16 (m, 2H), 5.19 (d, *J* = 1.7 Hz, 1H), 5.08 (d, *J* = 1.6 Hz, 1H), 3.34 (t, *J* = 6.2 Hz, 2H), 3.27 (t, *J* = 6.5 Hz, 2H), 2.44 (d, *J* = 7.7 Hz, 1H), 2.35 (td, *J* = 7.4, 1.6 Hz, 2H), 2.28 (dd, *J* = 13.7, 9.0 Hz, 2H), 2.14 – 2.04 (m, 4H), 2.02 – 1.96 (m, 2H), 1.87 (dd, *J* = 16.5, 7.8 Hz, 1H), 1.67 (p, *J* = 7.4 Hz, 2H), 1.57 (dq, *J* = 12.4, 6.6 Hz, 2H), 1.40 (h, *J* = 6.5 Hz, 2H), 1.29 (p, *J* = 7.7 Hz, 2H).

LRMS (APCI) m/z[M+H]$^+$ calc'd for $C_{31}H_{37}O_4$: 473.6, found 473.3

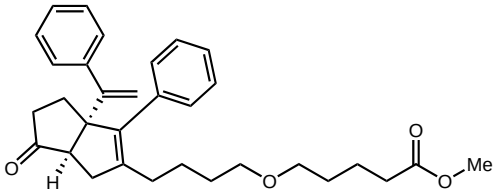

Methyl-5-(4-((3a*R*,6a*R*)-6-oxo-3-phenyl-3a-(1-phenylvinyl)-1,3a,4,5,6,6a-hexahydropentalen-2-yl)butoxy)pentanoate: According to general procedure C, 5-(4-((3a*R*,6a*R*)-6-oxo-3-phenyl-3a-(1-phenylvinyl)-1,3a,4,5,6,6a-hexahydropentalen-2-yl)butoxy)pentanoic acid (529 mg, 1.1 mmol) was reacted with HCl in methanol to give the title compound (545 mg, quantitative yield) as a yellow oil.

^{1}H NMR (600 MHz, Chloroform-*d*) δ 7.39 – 7.33 (m, 2H), 7.33 – 7.28 (m, 3H), 7.26 (t, *J* = 3.9 Hz, 3H), 7.22 – 7.19 (m, 2H), 5.22 (d, *J* = 1.5 Hz, 1H), 5.11 (d, *J* = 1.4 Hz, 1H), 3.66 (s, 3H), 3.34 (t, *J* = 6.4 Hz, 2H), 3.28 (t, *J* = 6.5 Hz, 2H), 2.46 (d, *J* = 7.8 Hz, 1H), 2.38 – 2.24 (m, 4H), 2.14 – 1.99 (m, 5H), 1.91 (dd, *J* = 16.5, 7.8 Hz, 1H), 1.66 (ddd, *J* = 12.4, 8.8, 6.0 Hz, 2H), 1.56 (dq, *J* = 10.3, 6.6 Hz, 2H), 1.41 (dt, *J* = 9.8, 6.5 Hz, 2H), 1.31 (q, *J* = 7.8 Hz, 2H).

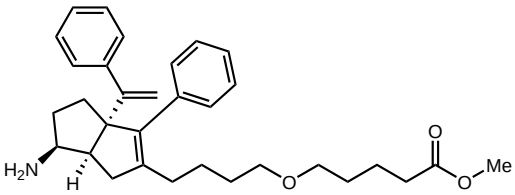

Methyl-5-(4-((3a*R*,6*S*,6a*R*)-6-amino-3-phenyl-3a-(1-phenylvinyl)-1,3a,4,5,6,6a-hexahydropentalen-2-yl)butoxy)pentanoate: According to general procedure D, Methyl-5-(4-((3a*R*,6a*R*)-6-oxo-3-phenyl-3a-(1-phenylvinyl)-1,3a,4,5,6,6a-hexahydropentalen-2-yl)butoxy)pentanoate (545 mg, 1.13 mmol) was reacted with Ammonia (816 μL, 5.65 mmol), $Ti(O\textit{i}Pr)_4$ (517 μL, 1.7 mmol), and $NaBH_4$ (128 mg, 3.4 mmol) in ethanol (11 mL) to give the title compound (235 mg, 42% yield) as a clear oil after purification by flash chromatography (0-10% MeOH/DCM).

^{1}H NMR (600 MHz, Chloroform-*d*) δ 7.29 – 7.24 (m, 7H), 7.24 – 7.21 (m, 3H), 5.09 (d, *J* = 1.4 Hz, 1H), 4.97 (d, *J* = 1.5 Hz, 1H), 3.65 (s, 3H), 3.50 (td, *J* = 10.4, 9.2, 4.0 Hz, 1H), 3.30 (t, *J* = 6.4 Hz, 2H), 3.23 (q, *J* = 5.9 Hz, 2H), 2.67 (t, *J* = 9.1 Hz, 1H), 2.42 (d, *J* = 17.8 Hz, 1H), 2.31 (t, *J* = 7.5 Hz, 2H), 2.25 (dd, *J* = 17.8, 8.9 Hz, 1H), 2.17 (q, *J* = 7.4, 5.6 Hz, 2H), 2.07 – 2.00 (m, 1H), 1.75 (dt, *J* = 12.6, 5.6 Hz, 1H), 1.72 – 1.61 (m, 4H), 1.54 (dt, *J* = 9.4, 6.5 Hz, 2H), 1.38 (ddt, *J* = 23.5, 16.8, 8.7 Hz, 4H).

LRMS (APCI) m/z$[M+H]^+$ calc'd for $C_{32}H_{42}NO_3$: 488.7, found 488.3

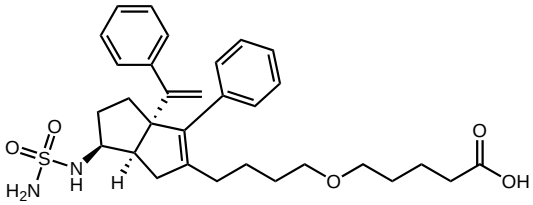

5-(4-((3a*R*,6*S*,6a*R*)-3-phenyl-3a-(1-phenylvinyl)-6-(sulfamoylamino)-1,3a,4,5,6,6a-hexahydropentalen-2-yl)butoxy)pentanoic acid: According to general procedure E, Methyl-5-(4-((3a*R*,6*S*,6a*R*)-6-amino-3-phenyl-3a-(1-phenylvinyl)-1,3a,4,5,6,6a-hexahydropentalen-2-yl)butoxy)pentanoate (1.326 g, 2.69 mmol) was reacted with 13.45 mmol sulfamide (5 eq, 1.21 g) and 8.07 mmol triethylamine (3 eq, 1.13 mL) in 53.8 mL water and 26.9 mL ethanol. For the ester hydrolysis, 26.9 mmol of lithium hydroxide was used (10 eq, 645 mg). Purified by silica chromatography (15-65% EtOAc:Hex + 1% AcOH). 1.15 g, 74%

^{1}H NMR (600 MHz, Chloroform-*d*) δ 7.34 – 7.27 (m, 4H), 7.26 – 7.24 (m, 5H), 7.19 – 7.15 (m, 2H), 5.55 (d, *J* = 8.2 Hz, 1H), 5.10 (d, *J* = 1.2 Hz, 1H), 4.91 (d, *J* = 1.2 Hz, 1H), 4.75 (s, 2H), 3.79 (dtd, *J* = 11.5, 8.5, 5.8 Hz, 1H), 3.51 – 3.36 (m, 5H), 2.63 (td, *J* = 9.0, 2.3 Hz, 1H), 2.47 (dd, *J* = 17.8, 2.4 Hz, 1H), 2.39 (t, *J* = 7.5 Hz, 2H), 2.21 – 2.10 (m, 3H), 1.98 (dq, *J* = 10.3, 6.3, 4.9 Hz, 2H), 1.80 (dt, *J* = 14.8, 7.4 Hz, 1H), 1.72 (tq, *J* = 18.0, 6.5, 5.4 Hz, 3H), 1.62 (p, *J* = 6.7 Hz, 3H), 1.58 – 1.46 (m, 6H).

LRMS (APCI) m/z[M+H]$^+$ calc'd for $C_{31}H_{41}N_2O_5S$: 553.7, found 553.3

Synthesis of Diether Compounds

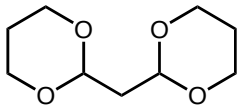

di(1,3-dioxan-2-yl)methane: The title compound was prepared according to the reported procedure (17.6 g, 94%) and the NMR data were consistent with those previously reported[115]

3,3'-(propane-1,3-diylbis(oxy))bis(propan-1-ol): A dry 3-neck round bottom flask charged with a stir bar was removed from a drying oven and sealed with septum stoppers before being connected to a vacuum line. The flask was allowed to cool to room temperature under vacuum. Once cool, Di(1,3-dioxan-2-yl)methane (21 g, 111.85 mmol, 1.0 equiv) and freshly prepared $Cu^{II}(OTf)_2$ (810 mg, 2.24 mmol, 2% loading) were added to the flask under positive nitrogen pressure. The flask was resealed with a septum stopper. The atmosphere was exchanged by applying vacuum and backfilling with N_2 (this process was conducted a total of three times). Degassed tetrahydrofuran (THF, 65 ml/mmol Di(1,3-dioxan-2-yl)methane) was delivered to the flask and the resulting solution was cooled to 0°C. Once cool, BH_3·DMS (37.1 ml, 391.5 mmol, 3.5 equiv) was added. The resulting mixture was allowed to stir overnight while warming to rt. The reaction was quenched with MeOH and subjected to a short celite plug. The resulting crude mixture was concentrated *in vacuo* and subjected to silica gel chromatography (5-15% MeOH/EtOAc) to afford the title compound (13.3 g, 62%). The title compound's NMR data were consistent with those previously reported.[115]

[115] Castro, P. P., Tihomirov, S., & Gutierrez, C. G. (1988). A convenient synthesis of substituted polyether diols. *The Journal of Organic Chemistry*, *53*(21), 5179–5181. https://doi.org/10.1021/jo00256a060

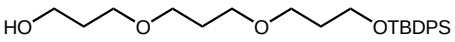

2,2-dimethyl-3,3-diphenyl-4,8,12-trioxa-3-silapentadecan-15-ol: To a solution of tripropylene glycol (13.3 g, 69.2 mmol, 1.3 equiv) and imidazole (3.62 g, 53.2 mmol, 1 equiv) in anhydrous THF (800 ml) in an oven-dried flask under nitrogen at r.t. was added *tert*-butyl(chloro)diphenylsilane (13.85 ml, 53.2 mmol, 1 equiv) and stirred for 2.5 h. The resulting solution was concentrated *in vacuo* and subjected to silica gel chromatography (20-50% EtOAc/Hexanes) to afford the title compound (12.3 g, 54%).

^{1}H NMR (600 MHz, Chloroform-*d*) δ 7.67 – 7.65 (m, 4H), 7.43 – 7.35 (m, 6H), 3.77 – 3.73 (m, 4H), 3.61 – 3.58 (m, 2H), 3.54 (t, *J* = 6.4 Hz, 2H), 3.49 (t, *J* = 6.4 Hz, 2H), 3.46 (t, *J* = 6.3 Hz, 2H), 2.42 (s, 1H), 1.85 – 1.78 (m, 6H), 1.04 (d, *J* = 0.6 Hz, 9H).

^{13}C NMR (151 MHz, Chloroform-*d*) δ 135.56, 133.99, 129.54, 127.60, 70.46, 68.46, 67.76, 67.63, 62.35, 60.84, 32.72, 31.96, 30.07, 26.86, 19.24.

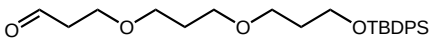

2,2-dimethyl-3,3-diphenyl-4,8,12-trioxa-3-silapentadecan-15-al: To a solution of 2,2-dimethyl-3,3-diphenyl-4,8,12-trioxa-3-silapentadecan-15-ol (12.3 g, 28.6 mmol, 1 equiv) in anhydrous THF (500 ml) in an oven-dried flask under nitrogen at 0°C was added Dess-Martin Periodinane (14.5 g, 34.3 mmol, 1.2 equiv) and allowed to warm to room temperature and stirred for 1.5 h. The reaction mixture was then filtered through a pad of celite. The resulting solution was concentrated *in vacuo* and subjected to silica gel chromatography (20-50% EtOAc/Hexanes) to afford the title compound (10.5 g, 86%).

^{1}H NMR (600 MHz, Chloroform-*d*) δ 9.77 (td, *J* = 2.0, 0.7 Hz, 1H), 7.69 – 7.64 (m, 4H), 7.44 – 7.34 (m, 6H), 3.74 (dt, *J* = 8.1, 6.1 Hz, 4H), 3.54 (t, *J* = 6.4 Hz, 2H), 3.49 (t, *J* = 6.4 Hz, 2H), 3.45 (t, *J* = 6.3 Hz, 2H), 2.66 – 2.61 (m, 2H), 1.81 (dp, *J* = 8.0, 6.4 Hz, 4H), 1.04 (s, 9H).

^{13}C NMR (151 MHz, Chloroform-*d*) δ 201.30, 135.56, 133.99, 129.55, 127.61, 68.25, 67.58, 64.47, 60.83, 43.87, 32.75, 29.98, 26.85, 19.24.

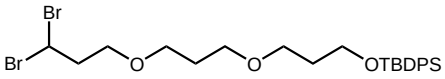

15,15-dibromo-2,2-dimethyl-3,3-diphenyl-4,8,12-trioxa-3-silapentadecane: To a cold solution of triphenyl phosphite (7.1 g, 27.0 mmol, 1.1 equiv) in anhydrous dichloromethane (350 mL) maintained at -78°C under N_2 flow, bromine (1.4 ml, 27.0 mmol, 1.1 equiv) was dropped in. Anhydrous triethylamine (4.1 mL, 29.5 mmol, 1.2 equiv) and 2,2-dimethyl-3,3-diphenyl-4,8,12-trioxa-3-silapentadecan-15-al (10.5 g, 24.5 mmol, 1 equiv) were added to the faint orange solution. The reaction mixture was stirred for 4 h and allowed to warm to room temperature after 3 h. The resulting solution was concentrated *in vacuo* and subjected to silica gel chromatography (10-30% MTBE/Hexanes) to afford the title compound (10.9 g, 78%).

^{1}H NMR (600 MHz, Chloroform-*d*) *δ* 7.68 – 7.65 (m, 4H), 7.44 – 7.40 (m, 2H), 7.40 – 7.36 (m, 4H), 5.82 (t, *J* = 6.7 Hz, 1H), 3.75 (t, *J* = 6.1 Hz, 2H), 3.55 (t, *J* = 6.4 Hz, 2H), 3.52 – 3.44 (m, 6H), 2.61 (q, *J* = 5.9 Hz, 2H), 1.86 – 1.77 (m, 4H), 1.05 (s, 9H).

^{13}C NMR (151 MHz, Chloroform-*d*) *δ* 135.57, 133.98, 129.55, 128.35, 127.61, 77.23, 77.02, 76.81, 68.18, 68.05, 67.64, 67.58, 60.84, 45.59, 43.09, 32.76, 29.99, 27.25, 20.21.

Jui-004

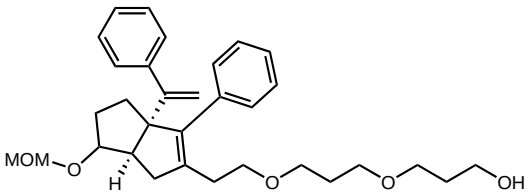

3-(3-(2-((3aR,6aR)-6-(methoxymethoxy)-3-phenyl-3a-(1-phenylvinyl)-1,3a,4,5,6,6a-hexahydropentalen-2-yl)ethoxy)propoxy)propan-1-ol According to general procedure A, 15,15-dibromo-2,2-dimethyl-3,3-diphenyl-4,8,12-trioxa-3-silapentadecane (2.50 g, 4.4 mmol) was reacted with (5-(methoxymethoxy)hept-6-en-1-yn-1-yl)benzene (1.20 g, 4 mmol) before being treated with 5 equivalents of tetrabutylammonium fluoride to give the title compound (1.24 g, 7:1 dr, 61% yield over 2 steps) as a yellow oil after purification by flash chromatography (0-50% EtOAc/Hex eluent).

^{1}H NMR: ^{1}H NMR (600 MHz, Chloroform-*d*) δ 7.32 (ddq, *J* = 6.0, 2.3, 1.3 Hz, 2H), 7.28 – 7.25 (m, 2H), 7.26 – 7.19 (m, 6H), 5.03 (q, *J* = 1.3 Hz, 1H), 4.98 (dd, *J* = 2.0, 1.3 Hz, 1H), 4.58 – 4.53 (m, 2H), 3.76 – 3.75 (m, 1H), 3.58 – 3.54 (m, 2H), 3.48 – 3.44 (m, 2H), 3.42 – 3.35 (m, 4H), 3.27 (d, *J* = 2.0 Hz, 3H), 2.40 (ddt, *J* = 11.0, 7.1, 1.7 Hz, 2H), 2.36 – 2.25 (m, 3H), 2.07 (d, *J* = 16.9 Hz, 1H), 1.78 (dddt, *J* = 7.8, 5.9, 3.4, 1.8 Hz, 5H), 1.67 – 1.58 (m, 2H).

LRMS (APCI) m/z[M+H]$^+$ calc'd for $C_{32}H_{42}O_5$: 507.3, found 475.3 (13b - $CH_3O^{\bullet}$)

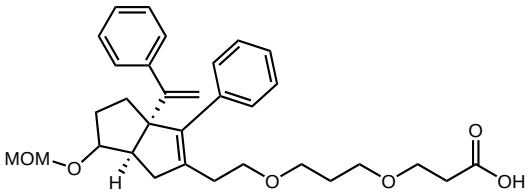

3-(3-(2-((3aR,6aR)-6-(methoxymethoxy)-3-phenyl-3a-(1-phenylvinyl)-1,3a,4,5,6,6a-hexahydropentalen-2-yl)ethoxy)propoxy)propanoic acid: According to general procedure B, 3-(3-(2-((3aR,6aR)-6-(methoxymethoxy)-3-phenyl-3a-(1-phenylvinyl)-1,3a,4,5,6,6a-hexahydropentalen-2-yl)ethoxy)propoxy)propan-1-ol (504 mg, 1 eq) was dissolved in 50 mL acetonitrile was treated with tetrapropylammonium perruthenate (TPAP, 0.1 equiv, 17.55 mg), N-Methylmorpholine-N-Oxide (NMO, 10 equiv, 1.17 g), and water (10 equiv, 180 microliters). The reaction mixture was allowed to stir overnight at room temperature. The reaction mixture was passed through celite, concentrated and purified on silica (20-80% EtOAc (containing 0.1% AcOH)/hexanes eluent) to provide the title compound. 285 mg, 45%.

^{1}H NMR (600 MHz, Chloroform-*d*) δ 7.35 – 7.30 (m, 2H), 7.29 – 7.25 (m, 2H), 7.24 – 7.20 (m, 6H), 5.03 (d, *J* = 1.4 Hz, 1H), 4.98 (d, *J* = 1.4 Hz, 1H), 4.61 – 4.55 (m, 2H), 3.80 – 3.74 (m, 1H), 3.67 – 3.63 (m, 2H), 3.52 – 3.46 (m, 2H), 3.42 – 3.34 (m, 5H), 3.29 (t, *J* = 1.0 Hz, 2H), 2.57 (td, *J* = 6.2, 1.4 Hz, 2H), 2.39 (dt, *J* = 9.3, 1.6 Hz, 1H), 2.35 – 2.29 (m, 2H), 2.26 (dt, *J* = 13.8, 6.5 Hz, 1H), 2.11 – 2.08 (m, 1H), 2.08 – 2.04 (m, 2H), 2.01 – 1.96 (m, 1H), 1.78 (pd, *J* = 6.4, 1.6 Hz, 2H), 1.74 – 1.67 (m, 1H), 1.67 – 1.58 (m, 2H).

LRMS (APCI) m/z calc'd for $C_{32}H_{40}O_6$: 521.28, found 489.3 (14a - $CH_3O^{\bullet}$)

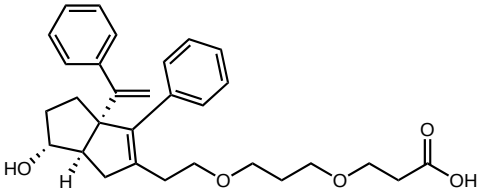

3-(3-(2-((3aR,6aR)-6-hydroxy-3-phenyl-3a-(1-phenylvinyl)-1,3a,4,5,6,6a-hexahydropentalen-2-yl)ethoxy)propoxy)propanoic acid. According to general procedure F,

125 mg of 3-(3-(2-((3aR,6aR)-6-(methoxymethoxy)-3-phenyl-3a-(1-phenylvinyl)-1,3a,4,5,6,6a-hexahydropentalen-2-yl)ethoxy)propoxy)propanoic acid was dissolved in 10 mL acetonitrile and 5 drops of 12M HCl. Reaction stirred for 10 minutes, then concentrated and purified by prep HPLC (15-75% ACN in water, 0.1% formic acid modifier, 30 minute gradient). 97 mg, 85%

^{1}H NMR (600 MHz, Chloroform-*d*) δ 7.37 (dd, *J* = 6.6, 2.9 Hz, 2H), 7.32 (t, *J* = 7.3 Hz, 2H), 7.28 (d, *J* = 7.8 Hz, 6H), 5.09 (s, 1H), 5.03 (s, 1H), 4.01 – 3.93 (m, 1H), 3.70 (t, *J* = 6.2 Hz, 2H), 3.54 (t, *J* = 6.3 Hz, 2H), 3.44 (qd, *J* = 9.2, 4.6 Hz, 4H), 2.61 (t, *J* = 6.1 Hz, 2H), 2.42 – 2.33 (m, 2H), 2.31 (dd, *J* = 12.6, 6.9 Hz, 2H), 2.14 (d, *J* = 17.2 Hz, 1H), 1.83 (p, *J* = 6.3 Hz, 2H), 1.74 (tt, *J* = 10.9, 5.5 Hz, 1H), 1.49 (pd, *J* = 7.1, 3.4 Hz, 1H), 1.43 (q, *J* = 7.7, 6.6 Hz, 1H), 1.36 (p, *J* = 3.5 Hz, 1H).

LRMS (APCI) m/z[M+H]$^+$ calc'd for $C_{30}H_{36}O_5$: 477.26, found 477.3

Jui-005

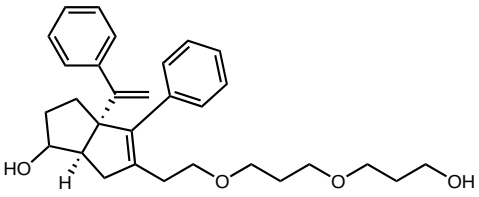

(3a*R*,6a*R*)-5-(2-(3-(3-hydroxypropoxy)propoxy)ethyl)-4-phenyl-3a-(1-phenylvinyl)-1,2,3,3a,6,6a-hexahydropentalen-1-ol: According to general procedure A, 15,15-dibromo-2,2-dimethyl-3,3-diphenyl-4,8,12-trioxa-3-silapentadecane (2.52 g, 4.4 mmol) was reacted with tert-butyldimethyl((7-phenylhept-1-en-6-yn-3-yl)oxy)silane (1.20 g, 4 mmol) before being treated

with three drops of HCl to give the title compound (758.7 g, X dr, 41% yield over 2 steps) as a yellow oil after purification by flash chromatography (10-100% EtOAc/Hex eluent).

^{1}H NMR (600 MHz, Chloroform-*d*) δ 7.36 – 7.31 (m, 4H), 7.30 – 7.24 (m, 3H), 7.22 – 7.20 (m, 3H), 5.05 (d, *J* = 1.1 Hz, 1H), 4.97 (d, *J* = 1.0 Hz, 1H), 3.92 (m, 1H), 3.73 (t, *J* = 5.5 Hz, 4H), 3.57 (q, *J* = 5.9, 4.7 Hz, 4H), 3.48 (dt, *J* = 16.8, 6.0 Hz, 3H), 3.42 – 3.33 (m, 4H), 2.57 (td, *J* = 10.7, 9.6, 5.9 Hz, 2H), 2.42 (t, *J* = 8.3 Hz, 1H), 2.39 – 2.20 (m, 4H), 2.14 – 2.03 (m, 4H), 1.96 – 1.88 (m, 1H), 1.67 – 1.58 (m, 1H).

LRMS (APCI) m/z[M+H]$^+$ calc'd for $C_{30}H_{39}O_4$: 463.6, found 463.3

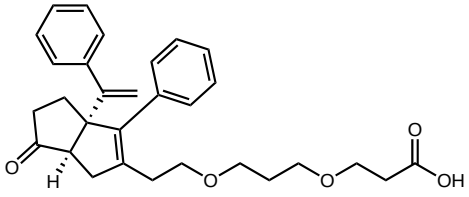

3-(3-(2-((3a*R*,6a*R*)-6-oxo-3-phenyl-3a-(1-phenylvinyl)-1,3a,4,5,6,6a-hexahydropentalen-2-yl)ethoxy)propoxy)propanoic acid: According to the oxidation general procedure, (3a*R*,6a*R*)-5-(2-(3-(3-hydroxypropoxy)propoxy)ethyl)-4-phenyl-3a-(1-phenylvinyl)-1,2,3,3a,6,6a-hexahydropentalen-1-ol (1.51 g, 3.2 mmol) was reacted with TPAP (112.5 mg, 0.32 mmol), NMO (3.74 g, 32 mmol), water (576 μL, 576 mg, 32 mmol), and acetonitrile (53 mL) to give the title compound (817 mg, 53% yield) as an oil after purification by flash chromatography (20-50% EtOAc/Hex).

^{1}H NMR (600 MHz, Chloroform-*d*) δ 7.36 (d, *J* = 4.7 Hz, 4H), 7.28 (m, 4H), 7.24 – 7.20 (m, 2H), 5.25 (d, *J* = 1.5 Hz, 1H), 5.13 (d, *J* = 1.5 Hz, 1H), 3.69 (t, *J* = 6.1 Hz, 2H), 3.56 – 3.44 (m, 2H),

3.44 – 3.28 (m, 4H), 2.60 (t, *J* = 6.0 Hz, 2H), 2.47 (t, *J* = 7.8 Hz, 2H), 2.44 – 2.20 (m, 4H), 2.15-2.07 (m, 2H), 1.97 – 1.88 (m, 1H), 1.77 (dq, *J* = 12.2, 6.2 Hz, 2H).

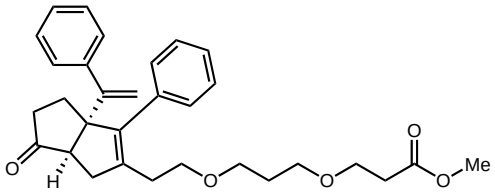

Methyl-3-(3-(2-((3a*R*,6a*R*)-6-oxo-3-phenyl-3a-(1-phenylvinyl)-1,3a,4,5,6,6a-hexahydropentalen-2-yl)ethoxy)propoxy)propanoate: According to general procedure C, 3-(3-(2-((3a*R*,6a*R*)-6-oxo-3-phenyl-3a-(1-phenylvinyl)-1,3a,4,5,6,6a-hexahydropentalen-2-yl)ethoxy)propoxy)propanoic acid (403.4 mg, 0.85mmol) was reacted with HCl in methanol to give the title compound (299 mg, 70%) as an oil after purification by flash chromatography (30% EtOAc/Hex).

^{1}H NMR (600 MHz, Chloroform-*d*) δ 7.36 (d, *J* = 4.3 Hz, 4H), 7.32 (p, *J* = 4.2 Hz, 2H), 7.28 (d, *J* = 6.5 Hz, 2H), 7.23 (dd, *J* = 7.7, 2.0 Hz, 2H), 5.24 (d, *J* = 1.4 Hz, 1H), 5.12 (d, *J* = 1.5 Hz, 1H), 3.68 (s, 3H), 3.66 (d, *J* = 6.5 Hz, 2H), 3.46 (td, *J* = 6.4, 3.3 Hz, 2H), 3.41 – 3.28 (m, 4H), 2.56 (t, *J* = 6.4 Hz, 2H), 2.46 (d, *J* = 7.8 Hz, 1H), 2.39 (dd, *J* = 14.2, 7.1 Hz, 1H), 2.35 (d, *J* = 16.4 Hz, 1H), 2.32 – 2.24 (m, 2H), 2.16 – 2.00 (m, 3H), 1.96 (dd, *J* = 16.5, 7.9 Hz, 1H), 1.76 (p, *J* = 6.4 Hz, 2H), 1.26 (d, *J* = 2.6 Hz, 1H).

LRMS (APCI) m/z[M+H]$^+$ calc'd for $C_{31}H_{37}O_5$: 489.6, found 489.3

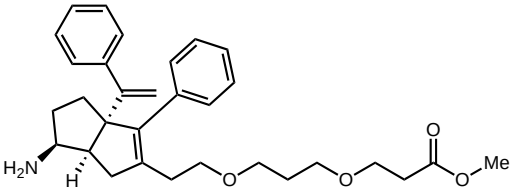

Methyl-3-(3-(2-((3a*R*,6*S*,6a*R*)-6-amino-3-phenyl-3a-(1-phenylvinyl)-1,3a,4,5,6,6a-hexahydropentalen-2-yl)ethoxy)propoxy)propanoate: According to general procedure D, Methyl-3-(3-(2-((3a*R*,6a*R*)-6-oxo-3-phenyl-3a-(1-phenylvinyl)-1,3a,4,5,6,6a-hexahydropentalen-2-yl)ethoxy)propoxy)propanoate (299.1 mg, 0.6 mmol) was reacted with Ammonia (1.7 mL, 12.2 mmol), Ti(O*i*Pr)$_4$ (272 μL, 261.4 mg, 0.92 mmol), and $NaBH_4$ (68.1 mg, 1.8 mmol) in ethanol (6 mL) to give the title compound (210.8 mg, 67% yield) as an orange oil after purification by flash chromatography (0-10% Methanol/DCM).

^{1}H NMR (600 MHz, Chloroform-*d*) δ 7.53 – 7.36 (m, 2H), 7.31 (dd, *J* = 8.3, 6.5 Hz, 3H), 7.29 – 7.25 (m, 3H), 7.19 (dq, *J* = 5.3, 2.9, 2.5 Hz, 2H), 5.18 (d, *J* = 1.5 Hz, 1H), 5.07 (d, *J* = 1.6 Hz, 1H), 3.93 – 3.86 (m, 1H), 3.75 – 3.66 (m, 3H), 3.65 (s, 3H), 3.60 – 3.51 (m, 3H), 3.48 (ddd, *J* = 9.2, 5.6, 3.2 Hz, 1H), 2.89 – 2.75 (m, 1H), 2.70 (dd, *J* = 9.7, 6.7 Hz, 1H), 2.66 – 2.58 (m, 2H), 2.54 (ddd, *J* = 16.2, 6.8, 4.4 Hz, 2H), 2.24 – 2.16 (m, 1H), 2.00 – 1.94 (m, 3H), 1.93 – 1.79 (m, 2H), 1.73 (dq, *J* = 15.9, 6.0 Hz, 2H), 1.49 – 1.38 (m, 1H).

LRMS (APCI) m/z[M+H]$^+$ calc'd for $C_{31}H_{40}NO_4$: 490.6, found 490.3

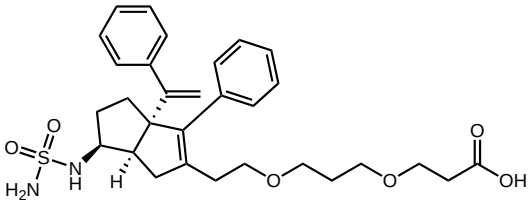

3-(3-(2-((3a*R*,6*S*,6a*R*)-3-phenyl-3a-(1-phenylvinyl)-6-(sulfamoylamino)-1,3a,4,5,6,6a-hexahydropentalen-2-yl)ethoxy)propoxy)propanoic acid: According to general procedure E,

Methyl-3-(3-(2-((3a*R*,6*S*,6a*R*)-6-amino-3-phenyl-3a-(1-phenylvinyl)-1,3a,4,5,6,6a-hexahydropentalen-2-yl)ethoxy)propoxy)propanoate (0.1 mmol, 52.6 mg) was reacted with sulfamide (0.5 mmol, 47 mg, 5 eq) and triethylamine (0.1 mmol, 0.417 mL, 3 eq) in 1 mL water and 2 mL ethanol. For the ester hydrolysis, 10 mL of 1M lithium hydroxide was used. Purified by silica chromatography (30-50% EtOAc:Hex). 9.6 mg

^{1}H NMR (600 MHz, Chloroform-*d*) δ 7.40 – 7.34 (m, 3H), 7.30 (m, 2H), 7.25 (m, 3H), 5.47 (d, *J* = 6.9 Hz, 2H), 5.30 (d, *J* = 1.2 Hz, 1H), 5.08 (s, 1H), 5.07 (s, 2H), 3.83 (m, 1H), 3.71 (d, *J* = 5.9 Hz, 2H), 3.69 – 3.58 (m, 2H), 3.53 (dd, *J* = 32.9, 9.4 Hz, 5H), 2.67 – 2.46 (m, 6H), 1.87 (dq, *J* = 13.4, 7.5, 6.9 Hz, 4H), 1.63 (dq, *J* = 15.0, 8.8, 7.1 Hz, 3H), 1.40 – 1.31 (m, 1H).

LRMS (APCI) m/z[M+H]$^+$ calc'd for $C_{30}H_{39}N_2O_6S$: 555.7, found 555.3